

OSLO METROPOLITAN UNIVERSITY
STORBYUNIVERSITETET

Master's Degree in
Structural Engineering and Building Technology
Department of Civil Engineering and Energy Technology

MASTER THESIS

THESIS TITLE Aeroelastic damping of high-rise timber buildings	DATE 09 June 2021
	NUMBER OF PAGES
AUTHOR(S) Vasileios Kotzamanis	SUPERVISOR(S) Arnab Chaudhuri Dimitrios Kraniotis CO-SUPERVISORS Haris Stamatopoulos

IN COLLABORATION WITH	CONTACT PERSON
-----------------------	----------------

SUMMARY <p>High-rise timber buildings have recently been the focus of many designers, because they offer a sustainable way to provide sustainable high and dense developments in urban regions with housing shortage. However, their dynamic properties differ a lot from conventional tall buildings due to timber's low weight, which becomes restrictive in satisfying the SLS criteria for vibrations and top floor accelerations. This thesis utilizes a two-way coupled fluid-structure interaction (FSI) for the case of Mjøstårnet to assess whether aeroelastic damping could have prevalent role in the increase of overall damping for this specific structure. The replication of the structure was performed in the FEM commercial software ABAQUS, while the computational fluid dynamics and two way coupling were done by the use of Star-CCM+.</p>
--

3 KEYWORDS
fluid-structure interaction (FSI)
High-rise timber building
Aeroelasticity

OSLO METROPOLITAN UNIVERSITY
OSLOMET

Thesis submitted for the course

MABY5900

**Aeroelastic damping of high rise timber
buildings**

by

Vasileios Kotzamanis

OSLOMET

Supervisors: **Arnab Chaudhuri and Dimitrios Kraniotis**
Co-Supervisor: **Haris Stamatopoulos**

9th of June 2021

Declaration of Original and Sole Authorship

I, Vasileios Kotzamanis, declare that this thesis entitled *Aeroelastic damping of high rise timber buildings* and the data presented in it are original and my own work.

I confirm that:

- No part of this work has previously been submitted for a degree at this or any other university.
- References to the work of others have been clearly acknowledged. Quotations from the work of others have been clearly indicated, and attributed to them.
- In cases where others have contributed to part of this work, such contribution has been clearly acknowledged and distinguished from my own work.
- None of this work has been previously published elsewhere, as of the submission date.

Date: 9th of June 2021

Signature



Preface

Aeroelastic damping of high rise timber buildings

The following thesis was procured during an *Erasmus+* exchange and is a product of the course *MABY5900(2021)* provided in the last semester of the 2-year Master's Degree Programme in Structural Engineering and Building Technology, in Oslo Metropolitan University and is also required for the completion of the 5-year study program Diploma in Civil Engineering by Aristotle University of Thessaloniki. The work presented equals to 30 *ECTS* and corresponds to 20 weeks worth of work.

In this thesis, the aeroelastic damping of high-rise timber buildings is investigated. More specifically the case of Mjøstårnet, the tallest timber building in the world, is studied under different wind loads. As the title of the thesis suggests, a core issue was the development of both the *FEM* model, the *CFD* domain as well as their two-way coupling, stimulating the *FSI*. The software that was used was *ABAQUS/CAE* for the *FEM* and *StarCCM+* for the *FSI* and *CFD* procedures, respectively. Both codes are subscribed under OsloMet's license plan.

As this work combines elements of structural dynamics and fluid mechanics, a lot of time was spent on gaining experience on the respective software and obtaining new knowledge by reviewing articles based on methodology and theory. I can now confidently say that I have a satisfying understanding of *FSI*, and have delved in depth in both software. Hopefully, the results of this thesis will provide an incentive for designers to consider the different types of damping in their assessment of a structure's serviceability levels.

Acknowledgment

Countless people supported my effort on this essay. Associate professors here at OsloMet, Dimitrios Kraniotis, Arnab Chaudhuri and Haris Stamatopoulos from NTNU provided invaluable feedback on my analysis and article reviews, demonstrated their rigorous support and continuous motivation as well as kept on steering me in the right direction in terms of the thought process required to study the topic of this thesis. I am also indebted to the academic staff in my home educational institution, Aristotle University of Thessaloniki. I especially want to thank Associate professor Dimitrios Pitilakis for his invaluable help in reviewing relative scientific papers and incorporating the SSI phenomenon. His course on the Post-Graduate study programme *Antiseismic Design of Structures* encouraged me to investigate the interaction between superstructure wind loading and the soil medium, and it also provided the methodology of modelling the foundation implicitly.

I would like to express my gratitude to my fellow student Koh Chuen Hon, for his guidance and advice on all steps of the simulations and our good discussions. Many thanks are also owed to Lazaros Melidis, PhD candidate at the *Laboratory of Experimental Strength of Materials and Structures* in Aristotle University of Thessaloniki, for his tremendous help on my first steps learning *ABAQUS/CAE*.

In addition, I thank deeply Rune Abrahamsen, CEO at *Moelven Limtre AS*, for his enthusiasm and his sharing of the *BIM* frame bearing structure model of Mjøstårnet.

Lastly, my family deserves endless gratitude for supporting me financially and emotionally on this *Erasmus+* experience. To my family, I give everything, including this.

Abstract

Aeroelastic damping of high rise timber buildings

This thesis aims to connect three different interdisciplinary engineering fields, in order to provide a holistic approach to structural design. Real time fluid-structure interaction (FSI), requires a two-way coupling scheme where the computational fluid dynamics (CFD) solution is exported on the finite element model (FEM) as external loads and then the deformations of the FEM are imported back into the (CFD) for the next solution iteration. This thesis utilises a (FSI) for assessing the importance of aeroelastic damping in high-rise timber buildings. In addition, the amount of damping soil structure interaction (SSI) is studied by using a set of Winkler springs. For the (CFD) part, unsteady Reynolds-averaged Navier–Stokes equations were used in conjunction with the SSTKO turbulence model, thus avoiding implementing the common LES or DES approaches. Lastly, aeroelasticity is studied by using 4 different finite elements models subjugated under 6 different wind conditions.

Abbreviations

All abbreviations used in the thesis will be listed here, with their definitions, in alphabetical order. This will include trivial and commonly used abbreviations, but not words that have entered into general English usage.

ABL	Atmospheric Boundary Layer
BC	Boundary Condition
BIM	Building Information Modelling
CAE	Computer-Aided Engineering
CFD	Computational Fluid Dynamics
CLT	Cross Laminated Timber
CWE	Computational Wind Engineering
DES	Detached Eddy Simulation
DOF	Degrees Of Freedom
EC1	Eurocode 1
EC2	Eurocode 2
EC5	Eurocode 5
EC8	Eurocode 8
FEA	Finite Element Analysis
FEM	Finite Element Modelling
FMI	Foundation Input Motion
FSI	Fluid Structure Interaction

FVM	Finite Volume Mesh
GLULAM	Glued Laminated Timber
LES	Large Eddy Simulation
MPC	Multi-Point Constraints
NTNU	Norwegian University of Science and Technology
PIM	Pressure Integral Method
PBM	Per parts Based Meshing
RANS	Reynolds-averaged Navier–Stokes equations
RMS	Root Mean Square
SC	Surface Control
SI	Scientific International
SLS	Service Limit State
SRANS	Steady state Reynolds-averaged Navier–Stokes
SLS	Service Limit State
SSI	Soil Structure Interaction
TKE	Turbulent Kinetic Energy
ULS	Ultimate Limit State
URANS	Unsteady state Reynolds-averaged Navier–Stokes
VC	Volumetric Control

Glossary

Power law

In statistics, a power law is a functional relationship between two quantities, where a relative change in one quantity results in a proportional relative change in the other quantity, independent of the initial size of those quantities: one quantity varies as a power of another.

Vortex shedding

An oscillating flow that takes place when air flows past a bluff (as opposed to streamlined) body at certain velocities, depending on the size and shape of the body. In this flow, vortices are created at the back of the body and detach periodically from either side of the body forming a Von Kármán vortex street. The fluid flow past the object creates alternating low-pressure vortices on the downstream side of the object.

Lock-in effect

A resonance phenomenon that occurs when the vortex shedding frequency of an elastic bluff body is close to its structural frequency. At this condition, amplification of motion can lead to fatigue or even catastrophic failure.

Rainflow-counting algorithm

The rainflow-counting algorithm is used in the analysis of fatigue data in order to reduce a spectrum of varying stress into an equivalent set of simple stress reversals. The method successively extracts the smaller interruption cycles from a sequence, which models the material memory effect seen with stress-strain hysteresis cycles.

Overconstraint checks

An overconstraint occurs when multiple consistent or inconsistent kinematic constraints are applied to the same degree of freedom. Overconstraints may lead to inaccurate solutions or prevent convergence. The vast majority of the overconstraints that are not resolved by the preprocessor are detected by the equation solver.

Superposition Principle

The superposition principle, also known as superposition property, states that, for all linear systems, the net response caused by two or more stimuli is the sum of the responses that would have been caused by each stimulus individually. So that if input A produces response X and input B produces response Y then input $(A + B)$ produces response $(X + Y)$.

Dummy analysis

A dummy variable is one that takes only the value 0 or 1 to indicate the absence or presence of some categorical effect that may be expected to shift the outcome. In structural analyses, a dummy variable can be a type of minuscule load and aims to check the convergence of the *FEM*.

Mach number

A dimensionless quantity in fluid dynamics representing the ratio of flow velocity past a boundary to the local speed of sound.

Sway motion

Oscillations that occur under wind loading in the across-wind direction. The amplitude and frequency of sway depends on height, slenderness and rigidity of the structure. The accelerations of the sway motion are critical for the comfort criteria on the top floors.

Nomenclature

- c Speed of sound at 25° (346 ms^{-1})
- ρ_{air} Density of air at 25° (1.184 kg(m)^3)
- C_p Isobaric specific heat of air at 25° ($1.006 \text{ kJ}^*(\text{kgK})^{-1}$)
- λ Thermal conductivity of air at 25° ($26.24 \text{ mW}^*(\text{mK})^{-1}$)
- Pr Turbulent Prandtl number (0.9)

Contents

Declaration of Original and Sole Authorship	ii
Preface	iii
Acknowledgment	iv
Abstract	v
Abbreviations	vi
Glossary	viii
Nomenclature	xi
Contents	xii
List of Figures	xvii
1 Introduction	1
1.1 High rise timber buildings	1
1.2 Wind loads in high rise timber buildings	3
2 Makings of a wooden tower	4
2.1 Scope and limitations of present work	5

2.1.1	Objectives of thesis	5
2.1.2	Limitations and simplifications.	5
2.2	Structural profile of Mjøstårnet	6
2.2.1	Building materials	8
2.2.2	Timber to steel connections	11
3	Structural background	17
3.1	Dynamics of high rise timber buildings	17
3.2	Damping	21
3.2.1	Damping in Mjøstårnet	24
3.3	Soil Structure Interaction	26
3.3.1	Dynamic response of piled raft foundations	27
4	Wind engineering	30
4.1	Assessing wind loads	31
4.2	Wind flow simulations	36
5	FEA Methodology	38
5.1	Geometry	39
5.2	Properties	44
5.2.1	Material properties	44
5.2.2	Assigning material normals	46
5.2.3	Material damping of GL30C	47
5.2.4	Slab damping	50
5.3	Assembly	52
5.3.1	Fully rigid connections (Model 1)	53
5.3.2	Semi Rigid Connections (Model 2)	53
5.4	Interactions	55
5.4.1	Point masses	55

5.4.2	Interaction between shell and wire elements	57
5.5	Steps	68
5.6	Loads	70
5.6.1	Boundary Conditions	70
5.6.2	Load Conditions	70
5.7	Meshing	71
5.7.1	Wire Elements	71
5.7.2	Shell Elements	72
5.8	Jobs and Output	75
5.8.1	Preparing the ABAQUS model for the co-simulation.	75
5.8.2	Frequency analysis results	76
5.9	Comments and discussion on the FEM part	79
6	CFD Methodology	80
6.1	Preparing the Geometry.	80
6.2	Creating the Region.	85
6.2.1	Assigning boundary conditions to surfaces.	85
6.3	Meshing.	86
6.3.1	Default meshing values.	90
6.3.2	Surface and Volumetric controls	91
6.4	Creating Physics continua	96
6.4.1	Numerical <i>URANS</i> model	97
6.5	Boundary Conditions	98
6.5.1	Upstream Boundary	98
6.5.2	Wall treatment for the ground surface	103
6.5.3	Downstream boundary	104
6.5.4	Symmetry planes	104
6.6	Fluid continuum solvers	105

6.6.1	Time-step configuration	105
6.6.2	Postprocessing	106
6.7	Discussion on the CFD part.	115
7	Coupling between CAE and CFD code	117
7.1	Setting up coupling	119
7.1.1	Solvers configuration for the co-simulation	119
7.1.2	Setting up morphing	120
8	Results and discussions	121
8.1	Displacement Time History, Model 1 & Model 4	123
8.1.1	Vh=17.95 m/s	123
8.1.2	Vh=35.9 m/s	124
8.1.3	Vh=53.85 m/s	125
8.1.4	Vh=71.8 m/s	126
8.1.5	Vh=179.5 m/s	127
8.1.6	Vh=224.375 m/s	128
8.2	Displacement Time History, Model 2 & Model 3	129
8.2.1	Vh=17.95 m/s	129
8.2.2	Vh=224.375 m/s	130
8.2.3	Acting forces, Model 1-Model 4	131
8.2.4	Vh=17.95 m/s	131
8.2.5	Vh=224.375 m/s	131
8.3	Damping results.	132
8.4	Discussions	134
8.5	Lock-in Phenomenon	136
8.5.1	Lock-In Displacements	137
8.5.2	Q-criterion	138

- Conclusion** **139**

- A Element sections** **140**

- B Timber Connections** **143**

- C SSI** **158**
 - C.1 Kinematic Interaction 158
 - C.2 Group pile dynamic Impedance matrices 159
 - C.2.1 Monopile simplified dynamic impedance matrix 159
 - C.2.2 Pile distance matrix and ψ motion matrix 160
 - C.2.3 ϵ_{xx} coefficient matrix 161
 - C.2.4 ϵ_{xy} coefficient matrix 162
 - C.2.5 ϵ_{xr} coefficient matrix 163
 - C.2.6 Group pile dynamic impedance matrix 164

- D Turbulence calculations** **165**
 - D.1 First cell height inflation 165
 - D.2 Inlet turbulent conditions 167

- Bibliography** **168**

List of Figures

- 1.1 Comparative sustainability study on 3 different structural scenarios. The authors concluded that the most sustainable solution was the wooden structure [1]. 2
- 1.2 Trending chart of construction lumber price in the US, proving a demand in housing and providing incentive for stakeholders to consider investing in residential high-rise timber buildings [2]. 2
- 2.1 Mjøstårnet| Source: (a),(b)Google commons, (c) Google Earth. 4
- 2.2 Mjøstårnet| Source: MOELVEN. 7
- 2.3 Source: Materials for Construction and Civil Engineering pp 557-583 [3] . . 8
- 2.4 GL30c Source: Swedish Wood [4] 9
- 2.5 CLTc Source: Swedish Wood [4]. 10
- 2.6 Effect of friction on dowel type connections| Source: Dorn(2012) 15
- 3.1 Frequency spectra for wind| Source: NatHaz Modeling Laboratory, University of Notre Dame. 18
- 3.2 Active tuned massdamper (ATMD) as an energy-absorbing system to reduce wind-induced structural response of buildings in the elastic range.| Source: Aly Mousaad Aly and Srinivasa Abburu (2015). 23

3.3	The combination of a shallow foundation and a deep foundation enables the sharing of load transfer to the soil. Source: Article written by Dr. Nainan P. Kurian.	26
3.4	Proposed macroelement accounting the near-field plastic deformations and the far-field elasticity. Source: Sensitivity study on building typologies with pile foundations in Groningen	28
3.5	Simplifying piles with a set of <i>Winkler</i> springs. Source: Google Commons	29
4.1	Lab setting ABL study using a wind tunnel test. Source: Google Commons.	34
5.1	Consistent units, SI. Source: ABAQUS/CAE Manual [5]	39
5.2	Front beam geometry.	40
5.3	Back beam geometry.	41
5.4	Inner beam geometry.	41
5.5	Rigid beams and facade shell geometry.	42
5.6	Foundation and Truss shell geometry.	42
5.7	Default shell normals orientation.	44
5.8	Beam normals orientation.	46
5.9	Y-component excitation modes.	50
5.10	Decoupling SSI Source: Graduate course ASTE07 by Dimitris Pitilakis. . .	60
5.11	Piled raft foundation plan.	61
5.12	Group pile kinematic interaction Source: Graduate course ASTE07 by Dimitris Pitilakis.	65
5.13	Single point's degrees of freedom. Source: <i>ABAQUS/CAE</i> manual	66
5.14	Springs/Dashpots connected to columns	67
5.15	Rigid frame mesh seeds.	71
5.16	Facade shell mesh seeds.	73
5.17	Truss shell mesh.	74
5.18	Fundamental eigenvalues of Model 1 and 4.	76

5.19	Fundamental eigenvalues of Model 2.	77
5.20	Fundamental eigenvalues of Model 3.	78
6.1	Imported solid geometry part Right: Before geometry edit, Left: After geometry edit.	81
6.2	Preliminary <i>SRANS</i> domain testing. Up: Separation field at the top of the building, Down: Wake field.	83
6.3	Split surfaces of the wind domain.	84
6.4	Details of the prism layer (a) Prism layer on top of the building, (b) Prism layer near the ground, (c) Prism layer around the Truss elements, (d) Overall prism layer	88
6.5	Prism layer quality scalar	88
6.6	Details of the surface mesh (a) Surface mesh on the building, (b) Transitional ground-building surface mesh, (c) Surface mesh on truss	92
6.7	Volumetric Controls.	93
6.8	Mesh quality scalars Small irregularities occur in the expected regions.	94
6.9	Volume mesh. (a) Mesh perpendicular to the wind flow, (b) Mesh lateral to the wind flow, (c) Building surface mesh.	95
6.10	Pressure Coefficient	108
6.11	Vh1=17.95m/s	109
6.12	Vh2=35.9m/s	109
6.13	Vh3=53.85m/s	109
6.14	Vh4=71.85m/s	110
6.15	Vh5=179.5m/s	110
6.16	Vh6=224.375m/s	110
6.17	Vh1=17.95m/s	111
6.18	Vh2=35.9m/s	111
6.19	Vh3=53.85m/s	111

6.20	Vh4=71.85m/s	112
6.21	Vh5=179.5m/s	112
6.22	Vh6=224.375m/s	112
6.23	Vh1=17.95m/s	113
6.24	Vh2=35.9m/s	113
6.25	Vh3=53.85m/s	113
6.26	Vh4=71.85m/s	114
6.27	Vh5=179.5m/s	114
6.28	Vh6=224.375m/s	114
6.29	Horseshoe vortexes	115
6.30	Suction field.	115
7.1	Co-Simulation flow chart	118
8.1	Surface probes	122
8.2	Q criteria-Vortex Shedding	138
8.3	Q criteria-Horseshoe vortices	138
A.1	Column elements numbering	140
A.2	Beam elements numbering	141
B.1	Timber connections.	143

Chapter 1

Introduction

1.1 High rise timber buildings

In the last few decades, the use of wood as the core bearing component for high-rise buildings has piqued the curiosity of many engineers and researchers. High timber buildings are on the rise, with a few examples being the 8-storey building Limnologen in Växjö, Sweden, the 9-storey Stadthaus in London, UK, the 14-storey building Treet in Bergen, Norway and lastly the 18-storey building Mjøstårnet in Brumunddal, Norway.

Timber constructions offer the combined possibility of minimal transportation costs and near zero carbon footprint. High rise timber constructions, residential buildings in particular, have relatively low stresses in their structural load bearing components in proportion to the building's total height. Walls and slabs can be designed to provide adequate acoustic separation and thermal performance and can effectively carry the levels of applied loading encountered [6].

One could argue that timber's excellent high strength-to-weight ratio, low carbon footprint and its high fire resistance would make the design and construction of high-rise timber buildings ever so desirable in the future. The minuscule relative weight of wood constitutes timber structures as earthquake resilient, however in their *SLS* they suffer

from wind induced accelerations that seem to affect the human comfort criteria and the acoustic properties of timber floor modules [7].

Structure Dimension	Masonry	RC frame	Wood frame
Ecologic	35p	45p	70p
	0p	5p	10p
	0p	0p	10p
	0p	0p	10p
	35p	50p	100p
Economic	10p	15p	35p
	20p	15p	25p
	25p	25p	20p
	0p	0p	10p
	55p	55p	90p
Social	10p	10p	15p
	20p	15p	20p
	20p	25p	15p
	5p	25p	20p
	55p	75p	70p

Figure 1.1: Comparative sustainability study on 3 different structural scenarios. The authors concluded that the most sustainable solution was the wooden structure [1].



Figure 1.2: Trending chart of construction lumber price in the US, proving a demand in housing and providing incentive for stakeholders to consider investing in residential high-rise timber buildings [2].

1.2 Wind loads in high rise timber buildings

Timber has the benefit of having a high strength-to-weight ratio compared to other building materials which in many cases is beneficial. Tall timber buildings would be an opportunity and provide for ecological, sustainable high and dense developments in urban regions with housing shortage. However, for the case with medium-to-high-rise buildings this might pose a challenge since the dynamic properties of the building will be quite different from a high-rise building with a load-bearing structure in steel or concrete [7]. The critical aspect on designing concrete or steel buildings has always been the safety aspect of the *ULS* criteria with a period of approximately 50 years. The interest in fulfilling the *SLS* criteria has been gaining more importance and interest. In the horizontal direction there are limitations both for the floor displacements but also for vibrations & accelerations. For tall buildings, the most important dynamic phenomenon is the sway due to wind loads.

There are three different international standards (*ISO*) that deal with horizontal vibrations in buildings and the human perception thereof apart from the national ones. Though not directly relevant to this thesis, they will be referred to concisely.

- **ISO 6897:1984**, Guidelines for the evaluation of the response of occupants of fixed structures, especially buildings and off-shore structures, to low-frequency horizontal motion (*0.063, 1 Hz*)
- **ISO 2631-2:2003**, Mechanical vibration and shock — Evaluation of human exposure to whole-body vibration — Part 2: Vibration in buildings (*1, 80 Hz*)
- **ISO 10137:2007**, Bases for design of structures - Serviceability of buildings and walkways against vibrations and covers the range from (*0.063, 5 Hz*) and uses the peak acceleration calculated for a wind velocity with a return period of one year. This is the standard referred to in *EC1*.
- **National standards**, For Norway, NS-EN 1990:2002/A1:2005/NA:2010.

Chapter 2

Makings of a wooden tower

Standing 85.4 meters tall, Mjøstårnet holds the title of world's tallest timber building. Mjøstårnet can be categorised as a mixed use residential high rise as it consists of offices, technical rooms, 32 apartments, 72 hotel rooms, one hotel suite on level 15, a cafeteria, a restaurant, a conference room on level 17 and a rooftop terrace. The building is situated in the small town of Brumunddal in Norway, about 140km north of Oslo. It is about one hour's drive from OSL airport. The building is next to highway E6 and faces the lake Mjøsa – Norway's largest lake. [8]

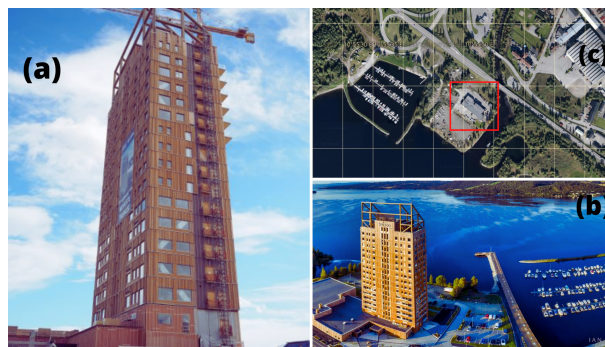


Figure 2.1: Mjøstårnet| Source: (a),(b)Google commons, (c) Google Earth.

2.1 Scope and limitations of present work

2.1.1 Objectives of thesis

In this thesis the damping properties of the case building, Mjøstårnet, will be investigated by the development of 4 different *FEA* models and subjugated in aeroelastic analysis.

This work involves the production of a *FEM* for the building in *ABAQUS/CAE*, the creation of a wind tunnel domain in *StarCCM+* and consequently the study of the displacement time history of the building by utilising *FSI* under different fractions of critical wind speed flows. In addition, the effect of *SSI* under wind loading will be briefly examined. Also the reduced stiffness of the connections between members in the frame and the effect of compartmental damping will be discussed. The goal of this work is to develop an understanding of the primary damping mechanisms that occur in tall timber buildings, as well as the levels of influence aeroelastic damping might have and whether it would be a beneficial consideration in the designing process.

2.1.2 Limitations and simplifications.

All the information used hereby (dimensions, materials, and area) are taken directly by the BIM frame truss model provided by *MOELVEN*. Certain simplifications were made to produce a simpler geometry that can be efficiently meshed and ran for multiple iterations on a standard medium-end PC and to efficiently complete the present work in the time frame of 4 months.

The simplifications herein are believed to have a minor effect on the results of a linear dynamic analysis and were thus judged appropriate. Those were:

1. Mjøstårnet was modelled as a stand-alone structural system. The lower attached building does not communicate directly with the tall timber structure; it is safe to assume that their dynamic responses will be independent.

2. The balconies of the 12th and upper floors were not modelled because they are not rigidly attached to the main frame structure, as they are suspended by cables and are also on the leeward side of the building, thus not interacting directly with the separation flow field.
3. The slabs of each floor were simulated as single point masses that interact with the columns and beams of each floor as part of a rigid continuum diaphragm.
4. The wooden truss construction on top will be simulated with a rectangle cross section. In reality, the edges were smoothed giving each beam a better aerodynamic performance by reducing the drag C_d and lift C_l shape coefficient.
5. In aeroelasticity, Reynolds number was held stable in order for the wind profile to stay relatively similar between different wind speed scenarios. This enabled the production of a single mesh scheme, without having the need for different mesh sizes.

2.2 Structural profile of Mjøstårnet

The structural profile of Mjøstårnet follows the principle of a standard frame design, with start to end columns and in between beams to ensure each floor's diaphragmatic function. In addition to the frame elements, the façade of the building is equipped with diagonal large-scale GLULAM trusses that act as the main load bearing elements in the same way that is expected in the cases of metal framework. More importantly, these large GLULAM elements are installed diagonally having thus an increased cross section area to bear the cumulative stresses and give the system its appropriate stiffness in the vertical and horizontal direction. The internal columns and beams are not equipped with truss elements.

Since the building is characterised by a prefabricated element- steel connections philosophy, monolithic walls are not present, however, all planar elements are CLT walls that act

as the secondary load bearing of the façade cladding as well as the internal core structure of the building which accommodates elevators and staircases. The absence of monolithic behaviour implies that the CLT walls do not contribute on the building’s horizontal stability and that the CLT elevator core is not rigidly attached to the frame bearing [8].

The external dimensions for each floor are (17×37 m), however the floor slab material differentiates between the floors. In more detail, the ground (1) floor is equipped with a massive concrete slab, while in the second (2) until the eleventh (11) floor the slabs are prefabricated wooden decks based on MOELVEN’s Trä8 building system. From the twelfth (12) floor and forth (18) the slabs are made of a composite concrete slab with a thickness of 30cm. This adjustment was made for increased mass on the top floors where the biggest deflections due to wind are expected. It also follows the principle of building high rise buildings with mass dampers or increased structural mass on the top floors to increase the structural damping provided during wind driven oscillations [9].

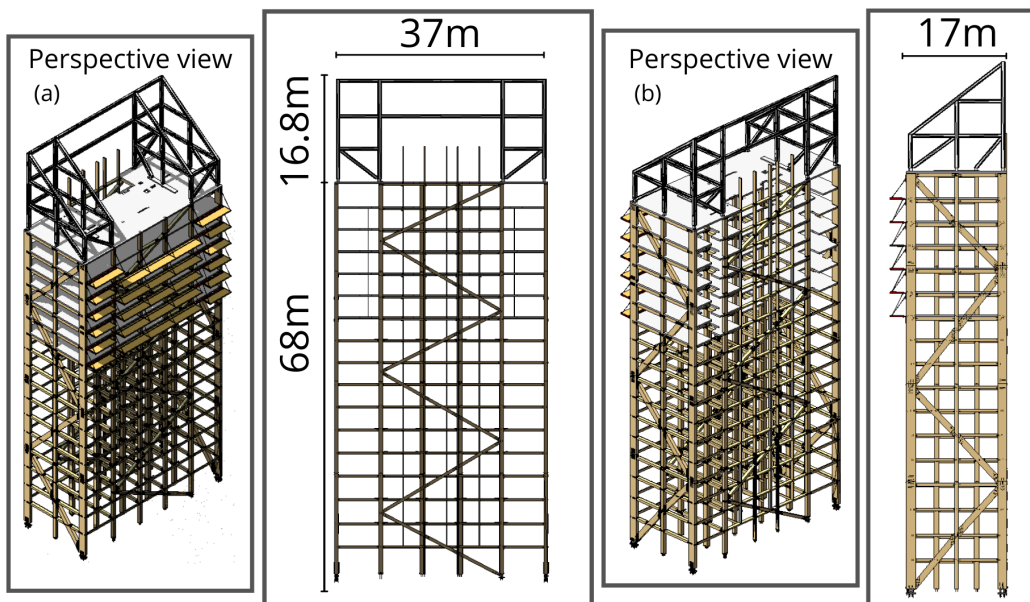


Figure 2.2: Mjøstårnet| Source: MOELVEN.

The foundation of Mjøstårnet can be classified as a piled raft system as there exists a massive concrete slab on the ground floor which acts as a uniform bearing for the poor saturated soil and prevents differential settlements. The slab itself is connected to the bedrock below using a reinforced group of long piles. The structural design of the timber structure is done according to EC5 by the engineering company *SWECO*.

The elevation plans of Mjøstårnet as well as the numbering of each element can be viewed in Appendix A.

2.2.1 Building materials

Timber as a natural material comes with an expected deviation on its material properties. Timber's axial strength comes from the cellulose fibers. The fibers are held together by the lignin that exists in the intercellular space. Consequently, timber as a composite material, exhibits different response dependent on the type of loading and its direction and as such it is categorized as an orthotropic material. Engineered timber, after being dried in a controlled and stable environment loses a big portion of body of water that existed in the cell at the fiber saturation point. The result is a material with high strength and stiffness, and low weight. The strength might be reduced by defects such as knots, and the humidity will influence the quality [10].

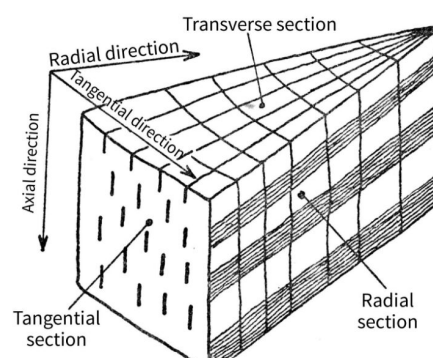


Figure 2.3: Source: Materials for Construction and Civil Engineering pp 557-583 [3]

GLULAM

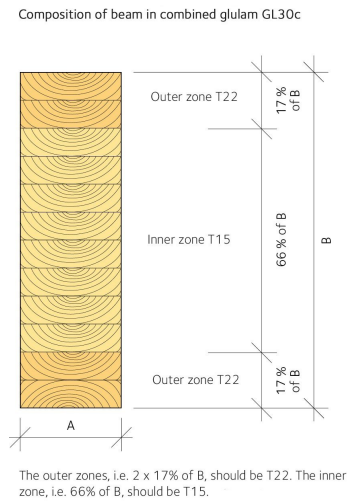


Figure 2.4: GL30c
Source: Swedish Wood [4]

Glued Laminated Timber (GLULAM) is the oldest type of engineered wood. It is produced by the use of individual laminates glued with melamine-formaldehyde or phenol-resorcinol-formaldehyde adhesives and finally compressed. The strength of GLULAM depends on the source material (softwood or hardwood), the quality of the laminates and connective resin applied. The final GLULAM product can be either homogenous, with same strength grade in all laminates, or non-homogenous with a varying strength grade. In GLULAM the fibers of all layers of an element are oriented lengthwise. It is used primarily as straight columns, beams, and arches.

The stiffness and densities for common strength classes of glulam are given in *NS – EN1194* [11]. For Mjøstårnet, the class of *Limtre Moelven Gl 30C* was exclusively used. For combined GLULAM in the strength class GL30c, the outer laminated zones can be at least 17 % of the cross-sectional height.

Strength Class	Value
Bending strength	$f_{m,g,k} = 30 \text{ (MPa)}$
Tensile strength	$f_{t,0,g,k} = 19.5 \text{ (MPa)}$
Compressing strength	$f_{c,0,g,k} = 24.5 \text{ (MPa)}$
Density	$\rho = 430 \text{ (kg/m}^3\text{)}$

CLT

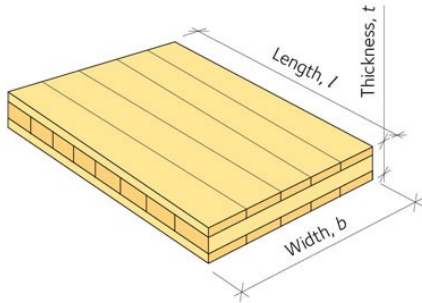


Figure 2.5: CLTc Source: Swedish Wood [4].

Cross laminated timber (CLT) was developed in the 90s and is gaining increasing popularity as it is a very robust material with a wide range of applications due to its ease of combination with other types of laminated timber. It is a composite material comprising solid wood boards.

In contrast to GLULAM, each subsequent laminated layer is glued orthogonally to the previous one in an odd number. Such arrangement gives the material high strength and stiffness in both directions while reducing shrinkage. In Europe, the main material for CLT production is spruce. Cross laminated timber, due to its high strength, is used for erecting high structures as it is suitable to be combined with concrete as well. CLT can be used either as bearing elements in the cladding (due to its mass it offers good thermal and acoustic insulation) or for partition purposes (such as assembling staircase cores). It can also be used for ceilings and staircases [11], [12].

Strength Class	Value
Bending strength	$f_{m,CLT,k} = 28 \text{ (MPa)}$
Tensile strength	$f_{t,0,g,k} = 18 \text{ (MPa)}$
Compressing strength	$f_{c,0,g,k} = 28 \text{ (MPa)}$
Density	$\rho = 420 \text{ (kg/m}^3\text{)}$

2.2.2 Timber to steel connections

The behaviour of timber structures is dominated by the strength and stiffness of connections. This implies that frame elements need to be designed and assembled according to plan to be able to transfer stresses at their steel connections. In Mjøstårnet, all GLULAM elements are connected by use of slotted-in steel plates and dowels as this is a high-capacity connection which is commonly used in bridges and large buildings. The behaviour of said connections can be governed by respective stiffness parameters in timber buildings who evaluate the amount of force needed to apply singular displacement, either transnational or rotational.

The first general strain-stress prediction theory (*Johansen 1974*) of dowel type fasteners assumed that the dowels and the timber element being connected will behave as essentially rigid plastic material. The three (3) main stiffness parameters which influence the load-carrying capacity behaviour of joints with dowel-type fasteners are [13]:

1. Embedding strength of the timber element
2. Bending moment load capacity of the steel dowel
3. Withdrawal strength of the dowel

Designing timber connections

EC5 (*CEN 1995 2004*) provides simple design guidelines for evaluating the stiffness of timber to steel connections. The design procedure must combine the global analysis of the structural timberwork and the local analysis of the connections. The stiffness modulus K_{ser} is dependent on the connection type, the mean density of the timber ρ , and the diameter d . For a dowel fastener connecting steel and timber the stiffness modulus K_{ser} is given per dowel and shear plane by slip modulus K_{ser} . The slip modulus K_{ser} is usually evaluated by push-out tests according to *EN26891* and corresponds to the secant value at 40 % of the load-carrying capacity of the connection.

$$K_{ser,dowel} = 2 * n_{sp} * \rho^{1.5} * \frac{d_c}{23} \quad (2.1)$$

Where,

1. n_{sp} is the number of dowels per shear plane
2. d_c is the diameter of the dowel (not the bore hole's)
3. ρ is the density of the timber element connected

According to *EC5*, when designing frame structures the deformations of the members and joints, the influence of support eccentricities and the stiffness of the supporting structure are considered in the determination of the member forces and moments. A simplified approach would be to assume connections as rationally stiff if their deformation has no significant effect upon the distribution of member forces and moments. Otherwise, connections may be generally assumed to be rationally pinned.

Since this approach is oversimplifying the design process it is rarely followed in a global level. Instead, the rotational stiffness of a joint can be calculated by the following formula:

$$K_{ser,\theta} = K_{ser,dowel} * \sum r_i^2 \quad (2.2)$$

Where,

1. K_{ser} is the slip modulus referred in the previous segment
2. r_i is the polar distance, namely the radius vector between an individual dowel and the geometric center of the dowel group.

It is believed that the *EC5* formula underestimates the overall connection stiffness, because it does not cover the influence of parameters such as the connection width, length of the dowel, and the increased withdrawal strength of its consequent deformed shape [14]. Also, it does not consider the influence of the angle to grain direction. According to test results, Dorn [15] claims that for 200mm wide specimens, the stiffness specified by *EC5* underestimates the observed stiffness value of the joint. However, according to *Siem J (2014)*, the rotational stiffness in the connections is dependent on the mutual placing of the fasteners as well as the stiffness of the fasteners. Guidelines provided in *EC5* imply that the stiffness is proportional with the number of dowels and shear planes. However, it has been reported from experiments that the stiffness is not proportional to the number of dowels; it appears to be less [13].

EC5 does not include any formulation for the withdrawal stiffness $K_{ser,w}$ for timber connections. Moreover, there was a lack of consensus in the references specifically about the withdrawal stiffness for dowel type connections. *Stamatopoulos and Malo (2016)* [16] performed experiments to assess the withdrawal stiffness of axially loaded threaded rods screwed into timber elements using an analytical expression based on Volkersen's theory. Also, the initial slip was proven not to be an attribute of the withdrawal itself when the threaded coupling parts of the set-up were tightly fastened. *Izzi et al (2016)* [17] determined based on experimental results of annular-ringed shank nails for CLT structures that the withdrawal stiffness of a nail is dependent on both the average density of CLT element and the diameter of the fastener. However, due to the lack of analytical expressions capable of predicting the withdrawal stiffness, an experimental value was adopted and its influence on the load-displacement response of the joint was examined. In conclusion, the withdrawal stiffness for each dowel for the specific experiment was adopted as:

$$K_{ser,w} = 1281.1N/mm \quad (2.3)$$

Friction between wood and steel surface

It should be noted, that EC5 does not include the coefficient of friction as a parameter in the designing. Friction, of course, exists and should be applied during the designing process, but the coefficient of friction changes depending on various parameters [18].

The effect of friction between wood and steel is supposed to be dependent on a variety of parameters such as:

- roughness
- surface texture
- wood density
- moisture content
- applied pressure
- orientation of annual rings in respect to the sliding plane
- and the direction of sliding

(*Sjödín et al., 2008*) show, in their experimental and numerical study of effect of friction in single dowel joints, how the coefficient of friction is changing by using different surfaces of dowels. From their work it is obvious that there, in some cases, can be a substantial effect of friction that could be taken into account in calculations. Nevertheless, the current version of EC5, does not explicitly involve friction in design as a parameter. In case of dowel connections used in structural engineering, a lot of previous research has been done, e.g. by (*Sjödín et al., 2008*) and (*Dorn, 2012*). (*Sjödín et al., 2008*) estimated the coefficient of friction between the dowel and the surrounding timber for two groups of dowels – with a smooth surface of the dowel and with a rough one. For joints with smooth dowel surfaces, the value of the coefficient of friction μ was estimated to lie between **0 and 0.3**. For joints with a rough surface dowel μ , was estimated to be between **0.3 and 0.5**.

Experimental investigations also show that the load-bearing capacity increases for single dowel joints when rough surface dowels are used compared to when smooth dowels are used.

(Dorn, 2012) performed structural experiments on single dowel-type timber connections using different roughness of the dowels and density of the wood and studied the influences of the coefficient of friction and the effects on the behaviour and failure of the connection. The outcomes verified the expected influence of increased dowel roughness on connection behaviour: increase of both maximum load and maximum displacement at failure. In finite elements simulations of dowel connections, the previous author used variations of the coefficient of friction from **0.0 up to 0.8** [15].

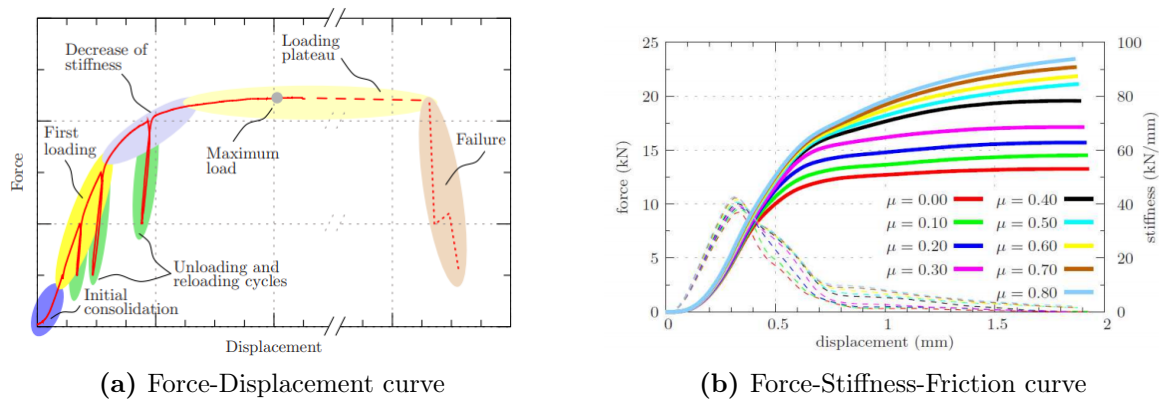


Figure 2.6: Effect of friction on dowel type connections| Source: Dorn(2012)

The results were significantly influenced by the change in friction coefficient; increased friction positively affected load bearing capacity, while stiffness was less significantly influenced.

As of yet the cyclical loading behaviour of timber connections has not been studied in depth. The reduction in secant stiffness under cyclical loading depends on the amplitude and the direction of loads [19].

GLULAM stiffness near connections

Lastly, aiming to simulate the stiffness of the connections realistically, a similar paper regarding the design issues of *Treet* [20], discussed the effect of connection slippage and the reduced stiffness near the connected part of the beam. To evaluate the effect of the connections in the GLULAM frame, all timber elements were cut into three parts, where the segments of each end and start were set to be equal in length to the *width* of the beam, and the properties of the segment were modified to represent the drop of stiffness near connections.

As the stiffness increases in the initial phase of the response curve, an initial effect is clearly present. Plausible causes could be nonlinear contact stiffness between the wood- and steel surfaces, unequal dowel embedment stiffness distribution along the dowels or possibly elastic deformation of the dowels. In structures, initial slips in connections are mainly caused by drilling inaccuracy, misalignments, and possible damage to the wood surface during installation.

The stiffness of the tested connections were compared to the stiffness of the GLULAM member with equal length to the connection.

$$k_{rel} = \frac{Kl_{connection}}{AE} \quad (2.4)$$

The relative stiffness k_{rel} was in the range of 0.35, when the stiffness was defined as secant, and to 1.0, if the stiffness was equal to the cyclic loading stiffness.

Chapter 3

Structural background

3.1 Dynamics of high rise timber buildings

Dynamic wind response is an unsteady time-dependent problem, especially in case of FSI because of the continuous shift in traction between the structure's surfaces and the wind flow. Consequently, for low mass high-rise buildings, even relatively medium intensity gusts can cause oscillations in the buildings weak direction hindering the user's comfort criteria.

The usual approach for determining the wind action induced vibrations is by performing a wind tunnel test using rigid or flexible bodies [21]. The rigid approach is better used in large scale *ABL* studies or in buildings with relative low height. In contrast, in cases where dynamic amplification phenomena cannot be ignored, such as high-rise buildings whose transversal eigenfrequencies lie below $1Hz$, they should be simulated using the flexible approach. Those structures may be subject to important along-wind displacements as well as significant across-wind response, which may be induced by synchronisation between the mechanical vibration and vortex shedding frequencies. This method of investigating the aeroelastic damping will be used in this thesis and further discussed in the appropriate segment.

Four properties are important for proper dynamic structural performance under wind loading:

1. The mass matrix should be adequate as to minimise the accelerations induced by wind loading their respective displacements. Comfort criteria should be considered.
2. Criteria for structural regularity both in plan and in elevation *EC8*(4.2.3.3) (Note: *EC8* is applied to seismic design, however even if the nature of the phenomena is vastly different, the principle of the dynamic response is similar [22]). The mass ideally would be allocated equally in plan.
3. The lateral stiffness matrix must provide enough rigidity in the structure to avoid severe deflections in the top floor. Enhanced damping can be used to avoid big consequent deformations.
4. Load intensity and temporal distribution thereof.

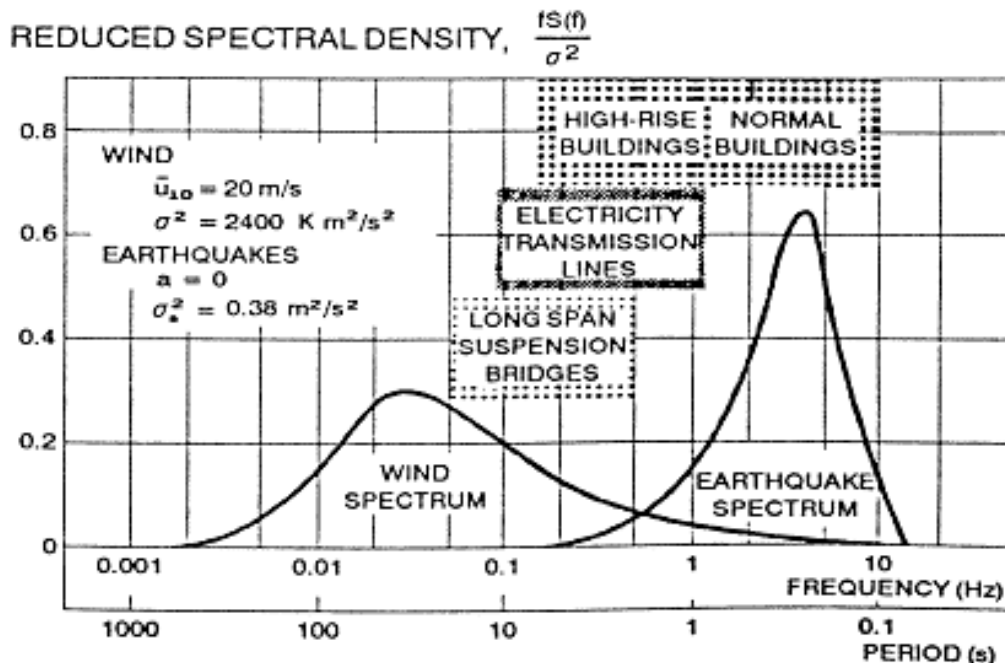


Figure 3.1: Frequency spectra for wind| Source: NatHaz Modeling Laboratory, University of Notre Dame.

A linear dynamic system is described with the well-known equation of motion:

$$\mathbb{M} * \mathbb{U}'' + \mathbb{C} * \mathbb{U}' + \mathbb{K} * \mathbb{U} = \mathbb{P} \quad (3.1)$$

Where,

- \mathbb{U} is the nodal displacement vector, \mathbb{U}' and \mathbb{U}'' are the corresponding nodal values for the velocity and acceleration vectors, respectively.
- \mathbb{M} is the excitation mass assigned to the acceleration vector, \mathbb{C} and \mathbb{K} are the damping and stiffness matrices. Since this thesis is focusing on the elastic spectra, \mathbb{C} and \mathbb{K} remain constant during the analysis.
- Lastly, \mathbb{P} refers to the external wind load excitation.

A multiple *DOF* building follows the same principle, however the higher the building is the more complex the lateral stiffness matrix will become [23]. The first two fundamental eigenmodes should be translational in the perpendicular and horizontal axis. High-rise buildings behave as a cantilever, and the mode shape is expected to be linear. Rotational eigenmodes should produce a torsional image around a point inside the plan of the structure, since Mjøstårnet is symmetrical in plan in both planar axes. When considering dynamic loads such as wind load on buildings, *ULS* factors such as collapse, toppling and fatigue is not the decisive design issue. The governing factor is usually if the wind induced acceleration in the top floors will cause discomfort or in extreme cases nausea. The accepted acceleration is dependent on the eigenfrequency f_0 of the building. [7]

Although the material strength to density ratio is more than 50 % higher for timber than for steel, the choice of cross-sections and connections may bring the ratio between the structural strength and mass quite close to that of steel. Consequently, for a GLULAM truss wooden building, the stiffness and mass will probably not be very different from a similar steel building. A rule of thumb for steel buildings is that the lowest fundamental

frequency can be estimated by $46/H$, where H is the height of the building in meters (*CEN*1991 – 1 – 42002) [20]. For Mjøstårnet, with a total height of 85.4m this would equal to:

$$f_{1,estimate} = \frac{46}{H} = \frac{46}{85.4} = 0.538Hz \quad (3.2)$$

The natural frequency ω_n ($rad * (s)^{-1}$) values can be validated by a precise *FEM* or by measuring ambient vibrations. Natural frequencies can be defined as the free vibrations of an elastic body. They tend to differ from the forced frequencies (the frequency of an applied load), but when they are equal the vibrations increase manifold. This phenomenon is known as resonance. The solution of the equation of free motion for natural frequencies for an nondamped system reduced to:

$$\mathbb{M} * U'' + \mathbb{C} * U' + \mathbb{K} * U = \mathbb{P} \implies \mathbb{M} * U'' + \mathbb{K} * U = 0 \quad (3.3)$$

An harmonic form is the key to the numerical solution of the dynamic problem and it also has physical importance. This form of solutions means that the motion of the degrees of freedom will be synchronised. Following that principle, the forced frequencies will only amplify the excitation of the structure and not change its configuration [24]. Assuming a harmonic solution of the form, where ϕ is the eigenvector and ω the circular natural frequency:

$$U = \phi * \sin \omega * t \quad (3.4)$$

By integrating equation (2.3),

$$-\omega^2 \mathbb{M} * \phi * \sin(\omega * t) + \mathbb{K} * \sin(\omega * t) = 0 \iff \mathbb{K} - \omega^2 * \mathbb{M} \phi = 0$$

Mjøstårnet's dynamic design was implemented without considering the stiffness of CLT walls and slabs. Thus, the first two fundamental design eigenfrequencies lie on the low spectrum [25],

$$f_{1,d} = 0.35Hz$$

$$f_{2,d} = 0.45Hz$$

However, in reality Mjøstårnet exhibits slightly stiffer behaviour. Measurements from ambient vibrations performed in Mjøstårnet by *NTNU* and provided by *Haris Stamatopoulos*, indicate the real fundamental eigenfrequencies to be:

$$f_{1,r} = 0.5Hz$$

$$f_{2,r} = 0.55Hz$$

$$f_{3,r} = 0.85Hz$$

3.2 Damping

Damping refers to the driving force behind energy dissipation of a harmonically vibrating system.

When a system is damped, the amplitude of a free oscillation will decay over time, and the resonance amplitude will be reduced [26]. The damping phenomenon of solid materials in viscoelastic fluids consists of:

- Viscous damping is the energy dissipation of a motion induced system in a fluid or gas. The motion is resisted due to the viscous friction of the fluid which absorbs kinetic energy
- Hysteresis damping or more commonly known as structural damping happens when some of the energy involved in the repetitive internal deformation and restoration

to original shape is dissipated in the form of random vibrations of the crystal lattice in solids and random kinetic energy of the molecules in a fluid [27].

- Coulomb damping is a type of constant mechanical damping in which energy is absorbed via sliding friction. The friction generated by the relative motion of the two surfaces that press against each other is a source of energy dissipation. In general, damping is the dissipation of energy from a vibrating system where the kinetic energy is converted into heat by the friction. Special frictional devices can be in-stalled in the structure to achieve higher frictional damping.
- Radiation damping is defined as energy loss to a surrounding medium. This can be for example dissipation of motion through soil that supports a structure, and it can be stated that the material damping of soil is an important parameter and must be included in the analysis of soil structure interaction, especially to determine the maximum top displacements [28].

This work is focused specifically on the aeroelastic damping of high-rise timber buildings; however, radiation and hysteresis damping will also be investigated in the SSI segment.

Aeroelastic damping refers to aerodynamic forces that depend on structural velocities. There is no clear recommended value in *EC1* for high rise timber buildings. The total damping of an aeroelastic model is due to the sum of the structural damping (equal to that of a rigid model) and of the ‘*equivalent aeroelastic damping*’ which is associated to the FSI, when the building is moving due to the oscillations induced [29]. The main methods of determining the viscous damping are:

- Rayleigh damping. This type of damping is represented by a global damping matrix, as a combination of the *stiffness-proportional* part, and the *mass-proportional* part. Therefore, Rayleigh damping is ideal for a combination of different damping ratios (i.e., in Mjøstårnet), as it is applied to the global mass and stiffness matrix.

- Composite modal damping, where the modal damping ratio is a weighted average of the damping ratio in each material. This gives obviously a constant damping ratio for all modes if the damping ratio is the same for all components and it downgrades to the Rayleigh method.

The real difference between the two methods in representing damping is visible when assigning different damping ratios to different components in the structure. The timber frame is assumed to have higher damping influence than the concrete slabs and massive wood corridor floors [28].

The damping ratio is estimated based on experience from similar buildings and field should be taken to give a more accurate estimate of the actual energy dissipation in the structure. The damping is usually higher than expected due to the complexity of the structure and numerous connections.

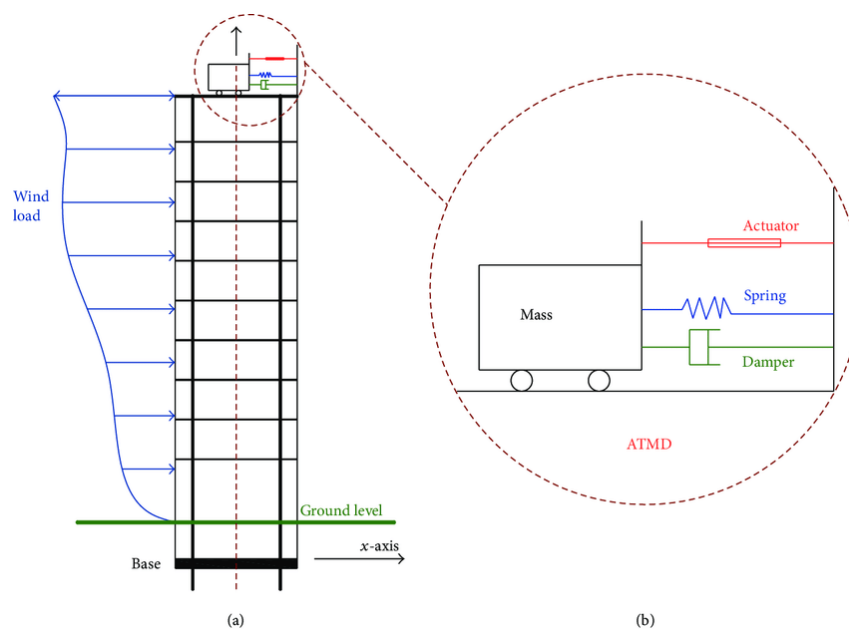


Figure 3.2: Active tuned massdamper (ATMD) as an energy-absorbing system to reduce wind-induced structural response of buildings in the elastic range. | Source: Aly Mousaad Aly and Srinivasa Abburu (2015).

3.2.1 Damping in Mjøstårnet

Tall timber structures can be superior regarding their capacities to dissipate vibration compared to conventional high-rises. Damping as a property is additive and besides the material is also dependant on the type of construction method (i.e. connections), and foundation.

Angela Feldmann et al. (2016) [30] mentions the material damping of timber is given as 0.4 – 0.8% which is higher than material damping of steel with 0.1 – 0.3% and about the same as damping of reinforced concrete with 0.4 – 0.9%. A timber building with dowel type connections contributes additional 0.6 – 0.8%. The type of support adds another 0.1 – 0.3% to the overall damping. Therefore, the range for timber buildings with dowel-type connections ranges from 1.1 – 1.9%. *Labonnote et al. (2013)* [31] denoted experimentally a damping ratio for glulam beams equal to $\xi = 1.13\%$. For Norwegian spruce solid wood, $\xi = 0.64\%$ can be used. About the damping ratio of timber floors, it seems to be dependent of the dead weight applied on them during the excitation [32]. The damping ratio proposed by EC5 is 1 %, but experimental data [32], [33] show that this value is rather conservative in wind loaded structures which is not surprising because the type of structures and excitation are different. For the concrete-timber composite floors, there can be no clear indication of the damping ratio since the detailed construction scheme is not available. *Fragiacomo and Lukaszewska (2010)* [33] tested dynamically a timber–concrete composite structure consisting of timber beams effectively interconnected to a concrete slab cast on top of the timber members. The value of damping was found out to be around $\xi_{composite\ floors} = 6 - 8\%$.

In this study, Rayleigh damping will be used to assign an equivalent structural damping equal to $\xi_{eq} = 1.5\%$ on the model with rigid connections. This value was chosen because it represents a conservative value *EC1-Part 1-4* proposes for the design of timber bridges [34]. Rayleigh damping will also be used to assign the appropriate material damping fac-

tors in each component of the structure, in the model with the semi-rigid connections. By comparing the results, a conclusion will be made between the use of equivalent structural damping and material damping.

3.3 Soil Structure Interaction

High-rise buildings are usually founded on some form of piled foundation subject to a combination of vertical, lateral, and overturning forces [35].

Timber buildings whilst having a subjectively lower vertical load due to their minuscule mass (when compared to conventional reinforced concrete or steel structures), suffer from lateral and overturning forces at their base when subjugated to high wind speeds. For this reason, a thick raft foundation system is to be constructed to resist the overturning moments accrued. The most common approach, however, would be the *piled-raft foundation* system, as seen in Figure 3.3 in which the soil directly supports the superstructure capacity at an *ULS* whilst the piles offer most of the stiffness for controlling the settlements at serviceability loads, as well as provide resistance against the overturning moments by activating passive soil pressure. *Poulos (2001)* proposed the pile raft foundation system to be used ideally on soil profiles consisting of relative stiff clays and/or dense sands. *Horikoshi and Randolph (1998)* suggested that piles could be concentrated in the areas under heavy loads, while reduced or even eliminated in areas without much loading.

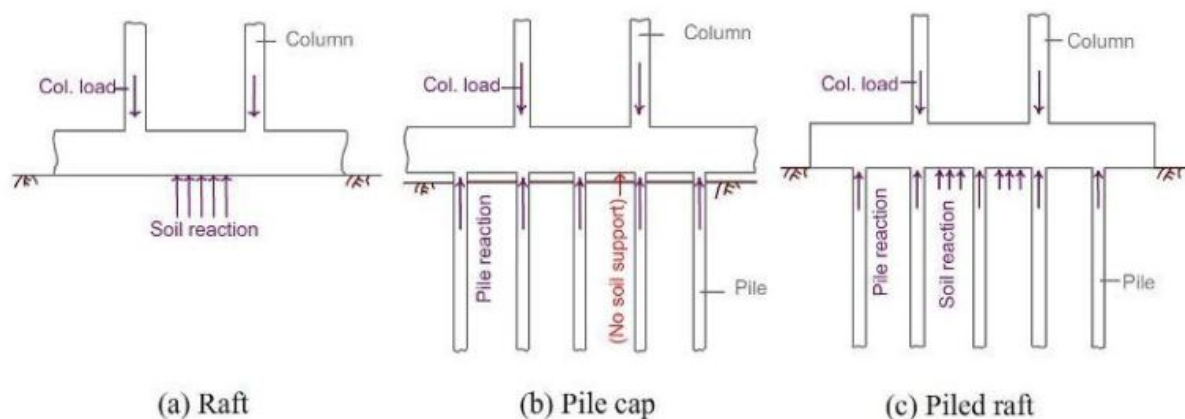


Figure 3.3: The combination of a shallow foundation and a deep foundation enables the sharing of load transfer to the soil. | Source: Article written by Dr. Nainan P. Kurian.

3.3.1 Dynamic response of piled raft foundations

Due to the piled raft dynamic wind induced response being an uncharted area, a similar approach to that of foundation modelling for offshore wind turbines is done. The logical comparison is a similar excitation due to the superstructure receiving lateral pressures by an incompressible flow. The modelling tests can be simplified by using the **apparent fixity method** and the **improved apparent fixity method**, respectively [36]. In most structural analyses, the connection of the structure with the foundation and the soil is thought of as fixed and rigid. However, the *SSI* provided by the interaction of the pile column with its surrounding soil medium, plays a major role on its dynamic response. In the case of vertical motion, the resistance developed by the pile is given by end bearing, skin-friction or by a combination of the two, in case of the pile subjected to horizontal forces the resistance is provided by horizontal bearing of the pile against the soil. Including the soil-foundation flexibility and a flexible pile foundation will give softer models with reduced natural frequencies and fatigue compared to one with a rigid base, because of the significant loss of energy in soil medium. That results in the natural frequency and mode shape in the two cases to be quite different from each other and the frequency parameter has important bearing on the dynamic magnification of the structural response [37]. The damping of the pile motion occurs because of:

- the radiation of wave energy into the far field
- the loss of energy due to internal friction of soil

Thus, the accountancy of both the radiation damping and the material or hysteresis damping are essential in an accurate estimation of dynamic response of pile-supported structures.

The radiation damping is found to be unaffected by the nonlinear soil behaviour [38].

Incorporating the SSI in a FEA

For linear elastic soil response, analytical solutions have been developed for a variety of foundations, such as piles and surface foundations, and for different soil types. Some of these solutions also provide the variation of the foundation impedance with frequency. *Kausel (2010)*, provides an extensive review of these solutions. For structural loads leading to slight soil non-linearity, these solutions have been used by using strain-compatible elastic modulus of the soil. For larger loads leading to non-negligible soil non-linearity or even near-failure conditions, the classical solutions based on fully integrated soil- foundation-structure models in finite elements have been the preferred approach [39].

Simulating SSI involves detailed 3D meshes for the soil and the structure, a big number of DOF and thus huge computational costs. This is the reason why simplified modelling strategies have been extensively developed during recent years. Amongst them, the *macro-element* approach consists in condensing all non-linearities into a finite domain *close field* and works with generalised variables (forces and displacements) at the centre of the foundation. In that way it allows considerably decreasing the necessary degrees of freedom of the numerical model [40].

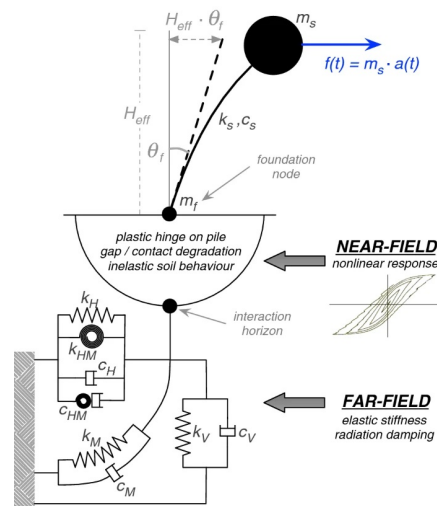


Figure 3.4: Proposed macroelement accounting the near-field plastic deformations and the far-field elasticity. | Source: Sensitivity study on building typologies with pile foundations in Groningen

An oversimplification of the SSI can also be done by implementing a set of *Winkler* springs perpendicular to the pile length. *Zania (2014)* [41] followed the approach of *Novak and Nogami* [42] by using the sub-structuring method and computed the dynamic response of soil-pile interaction. They implemented an iterative two-step analytical method that allows consideration of the off-diagonal terms of the dynamic impedance matrix. The results highlighted the importance of using the frequency-dependent impedance and the off-diagonal impedance terms on the natural frequencies and the damping of the system.

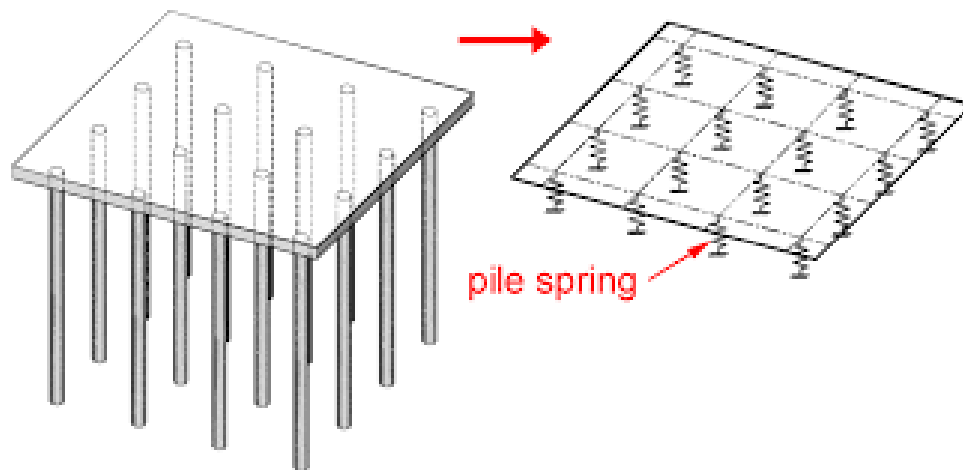


Figure 3.5: Simplifying piles with a set of *Winkler* springs. | Source: Google Commons

Chapter 4

Wind engineering

Whereas structural integrity is dependent on the along-wind vibrations, the comfort criteria is mostly affected by the crosswind vibrations since oscillations in that direction occur in a higher frequency and are connected with higher accelerations. In most cases a wind tunnel test is utilised to evaluate this phenomenon [43]. The response of any structure under a wind load is correlated with:

- a function of the geometry and shape of the building
- dynamic properties of the building (i.e. stiffness, damping)
- the wind conditions at the site.

More specifically, the wind conditions are a result of the surrounding terrain, the mean wind velocity, the mean return period, and the most common wind direction at the site. The mean wind velocities are given for all municipalities in Norway in the national annex of *Eurocode 1-4* [44]. The best representation of a varying of an unsteady wind flow would be by utilising a *stochastic time-series*, validated by either experimental measurements, namely *RMS* peak accelerometers on the structure or long-term measurements on a down-scaled model [45]. *EC1* allows for a simplified calculation, where the wind surface pressures are treated as a static load. This gives reasonable results for deflections but

cannot account for a FSI as well as the time-varying effect that causes vibrations.

An important aspect when considering wind forces calculated from *EC1* is that the wind is assumed to blow orthogonal to the building face. A more accurate procedure to represent the response from wind loading may be achieved by using a wind tunnel test [46].

4.1 Assessing wind loads

The methodology of investigating probable wind loads is not an inherent part of this work, apart from the *Aeroelastic Wind Tunnel* test that is, thus the other options will be mentioned for the sake of inclusion and future validation work. Those are:

- Wind design spectra
- Database-Assisted Design (DAD)
- High-Frequency Force Balance (HFFB)
- Wind pressure test, used for CWE model calibration
- Aeroelastic Wind Tunnel tests

Wind design spectra

Response spectra are used in seismic design, for example, according to *EN1998 – 1*, and are derived and simplified records of the occurred earthquakes. It is then possible to analyse the reaction of the structure to such a response spectrum by means of the modal analysis, for example. The corresponding set of coupled equations of motion for a multiple degree of freedom lumped-mass system is solved through an uncoupled set of modal equations and the design spectra is then applied to compute the contribution of each mode of vibration to the total response, see for example *Chopra(1995)*.

Consequentially and in a similar fashion, wind design employs theoretical wind spectra as an input for stochastic functions that generate partially correlated data series which in

turn give an output of synthetic dynamic response histories. In the case of wind loading, the forces distributed over the height of the structure are not fully correlated. However, the amount of energy imparted to the structural system can be estimated through suitable aerodynamic admittance functions to account for the lack of correlation of the wind gusts in relation to the size of the structure [22]. This is not a good approximation to the actual wind load, as very few structural factors are implemented, thus it represents the variation of wind load above the actual force.

Database-Assisted Design

Database-Assisted Design (*DAD*) represents a unified framework for analysis and design of buildings for wind loads that makes direct use of aerodynamic pressure time histories measured at many pressure taps on one or more wind tunnel models. The pressure taps should be installed in each side of the building. The concept is based on using a rigid model of the building in a wind tunnel. Local meteorological information on extreme wind speeds and their direction-dependence can be used in conjunction with the measured pressures to obtain estimates of peak wind effects with specified return periods to comply with the *EC* standards. Through direct use of measured pressures, rigorous accounting for wind direction, and accurate modelling of structural dynamics for flexible buildings, *DAD* enables more accurate estimation of peak wind effects than is allowed by simplified procedures in current use, thus facilitating more risk-consistent designs. The output of a *DAD* is quite rigorous, and one can extract data about the internal forces, capacity ratios as well as deflections and accelerations [47].

High Frequency Force Balance

High Frequency Force Balance (*HFFB*) test is used to estimate wind loads, wind frequencies and the wind induced accelerations of the building for the *SLS* criteria. In the *HFFB* test, light and rigid model is used to measure the effect of wind loads by six internal stress parameters at the base of the structure (shear and moment of axis). The

wind force coefficient is computed by time dependent force data and the response of the model is evaluated by the spectral modal analysis. The wind forces on the building can then be found from the support reactions. *HFFB* is a good approach for buildings with linear fundamental mode shapes [48].

Wind Pressure Test

Wind Pressure Tests are based on in-situ performed measurements to evaluate wind pressure on the outer cladding of a building and use them to calibrate numerical schematic solvers [49]. The wind pressure is then converted into an equivalent wind load. This method is indicated for the evaluation of wind loads on complex structures, such as open stadiums or factory roofs. Due to the mandatory system identification required to evaluate the measurements, *BIM* models or detailed plans of the structure should be available as a pressure applied to a point may vary in account of construction deviations from the model. The results provide pressure coefficients (means, *RMS*, peak value). In similar fashion to the High Frequency Force Balance approach, the results are derived by pressure integral method *PIM* and results are subsequently used to provide the estimates of the full-scale response of the buildings.

Aeroelastic Wind Tunnel Test

Aeroelastic testing is considered as the most effective technique for a vibration structural response study. By modelling 3D vibration mode shapes of the building, one can assess all excitation mechanisms of wind, including buffeting, wake buffeting, vortex-induced vibration, and galloping [50]. Aeroelastic wind tunnelling is suitable for slender, flexible, and dynamically sensitive structure, such as high-rise timber buildings.

The objective of the aeroelastic model test is to investigate the vortex shedding-induced vibrations in which the narrower elevations are particularly vulnerable and aerodynamic instability within range of target wind speed. Bridge aerodynamics have shown that turbulence mitigates drastically vortex-induced vibration. While the height of timber

buildings increases steadily, the wind will be less turbulent in higher altitudes due to a more stable air temperature increment, thus they will be especially prone to across-wind vibrations.

In a laboratory setting for an aeroelastic wind-tunnel test, a model is prepared respecting both aerodynamic and structural dynamics scaling laws, resulting to the model behaving as the real structure would. In a physical wind tunnel test, responses are directly measured in the wind tunnel, using non-contact displacement meters (optical sensor type) or accelerometers. To include both torsional and translational motions, the accelerometers should be distributed over the plan of the building, preferably located in the corners. The wind-structure interaction is accounted for through by parameters such as:

- Aerodynamic damping
- Virtual fluid mass
- natural frequency of the building



Figure 4.1: Lab setting ABL study using a wind tunnel test. | Source: Google Commons.

Another important aspect is the load correlation effect and its dependence on vibration amplitude in the across-wind vibrations due to *vortex shedding* [50]. Aeroelastic testing is a must for those cases, as it can study the lock-in effect which is dependent on the vibration amplitude and FSI. **Another interesting topic would be to investigate the fatigue rate near the connections due to across-wind excitation making *rainflow-counting algorithm* indispensable.** For structures with low natural frequency, the structural response is dominated by the background response i.e., the *vortex shedding* in the wake region, while for higher natural frequency the resonant response becomes more significant [51].

Timber structures, due to their flexibility are expected to be in the lower frequency regions. However, during an aeroelastic wind tunnel test, one significant expectation is the flexural load due to mass unbalance in stories (i.e., the use of power stories 12-18 in Mjøstårnet) of a high-rise timber building. Lastly, a wind tunnel test is also an optimal way of resembling an *ABL* since the near elevation-obstacle elevation can be easily reconstructed. For example, regarding the wake buffeting due to other nearby tall buildings, *EC1 (ENV1994)* suggests that along-wind building acceleration may be up to three times the original value and instructs on performing a wind tunnel analysis for more detailed info. Wake buffeting does not affect peak gust wind velocity, but it retards mean wind velocity and increase turbulence intensity thereof.

4.2 Wind flow simulations

The governing equations for a general fluid flow simulation are those of momentum, mass, and energy conservation over the wind tunnel space, which may be simplified when some physical assumptions are accounted for. Those are:

- The wind streams in the wind tunnel are composed by incompressible air.
- The wind flow is characterized as an isothermal process with a constant temperature.
- Those wind streams are in the turbulent flow range.
- The work of gravity is neglected in the wind flow.
- Air acts as a Newtonian fluid.

Linear Momentum Equation

$$\sum F = \frac{\partial}{\partial t} \int_{C_v} \rho * V * dV + \int_{C_s} V \rho * V * n * dA \quad (4.1)$$

Law of Mass Conservation

$$\mathbf{M} = \rho_i * U_i * A_i * dt - \rho_o * U_o * A_o * dt \quad (4.2)$$

Incompressible Euler equations with constant and uniform density

$$\begin{cases} \frac{Du}{Dt} = -\nabla w + g \\ \nabla * u = 0 \end{cases} \quad (4.3)$$

The most important aspect of in CWE modelling is to effectively simulate the coupled translational and torsional modes derived from a wind tunnel excitation. The conventional method of simulating the structure as a rigid linear model has been proved not adequate since only the linear modes can be considered [51].

Hence, the next step on aeroelastic modelling were non rigid, planar models. Whilst turbulence modelling has been efficiently tackled, turbulence effects near sharp corners (i.e. the façade of the building) have been proven difficult to simulate [52].

The main turbulence models used for an aeroelastic numerical simulation are primarily:

- *LES* (large eddy simulation), which simulates turbulent flows by numerically solving the *Navier–Stokes* equation. The principal idea behind *LES* is to reduce the computational cost by ignoring the smallest length scales. It requires resolving a very wide range of time and length scales, all of which affect the flow field. Such a resolution can be achieved with direct numerical simulation (*DNS*) [53].
- The *K-ε* model is one of the most common turbulence models, although it just does not perform well in cases of large adverse pressure gradients. It is a two-equation model, that means, it includes two extra transport equations to represent the turbulent properties of the flow. This allows to account for history effects like convection and diffusion of turbulent energy [51].
- The *K-ω* model is the similar iteration of the *K-ε* model, however it accounts better for the near wall flows as well as the boundaries. This is the preferred model for large wind tunnel simulation near structures.
- The Detached eddy simulation (*DES*) is a hybrid modification of the previously mentioned *LES* model, which attempts to use *RANS* equations to treat near-wall regions and treat the rest of the flow in an *LES*-like manner [54].

For a stationary flow of an incompressible Newtonian fluid, RANS equation is:

$$\rho * \bar{u}_j * \frac{\partial \bar{u}_i}{\partial x_j} = \rho \bar{f}_i + \frac{\partial}{\partial x_j} * [-\bar{p} * \delta_{ij} + \mu * (\frac{\partial \bar{u}_i}{\partial x_j} + \frac{\partial \bar{u}_j}{\partial x_i}) - \rho * u'_i \bar{u}'_j] \quad (4.4)$$

Chapter 5

FEA Methodology

This segment will analyze and expand on the simulation progress and methodology of the simplified *ABAQUS* model of Mjøstårnet. All the information used hereby (dimensions, materials and area) are taken directly by the *BIM* frame truss model provided by *MOELVEN*. Certain simplifications were made and they were mentioned in 2.1.2. Furthermore, four (4) separate models were developed which correspond to four (4) different damping mechanisms in conjunction with aeroelastic damping. Those were:

1. A fully rigid model, whose only damping mechanism is that of structural damping equal to $\xi=1.5\%$.
2. A semi rigid model, whose damping mechanism is material damping applied in different structural parts and reduced stiffness in connections will also be introduced.
3. A fully rigid model, whose damping mechanism is material damping $\xi=1.5\%$ and soil hysteresis damping introduced through the piled raft system (*SSI*).
4. A fully rigid model, with nonexistent structural damping. This model will be used to evaluate the damping introduced purely by aeroelasticity.

The damping values correspond and are derived from the review made in 3.2.

The instruction of this chapter will follow the format of *ABAQUS/CAE* modules and it will not correspond to the timewise procedure.

5.1 Geometry

The geometry of the model is the same in all scenarios. The most important aspect one should consider before starting modelling in *ABAQUS*, is to decide on consistent unit measurements.

For this Thesis, **SI** units were used by default from the following table [5]. The principle

Table 1. Consistent units.

Quantity	SI	SI (mm)	US Unit (ft)	US Unit (inch)
Length	m	mm	ft	in
Force	N	N	lbf	lbf
Mass	kg	tonne (10^3 kg)	slug	$\text{lbf s}^2/\text{in}$
Time	s	s	s	s
Stress	Pa (N/m^2)	MPa (N/mm^2)	lbf/ft^2	psi (lbf/in^2)
Energy	J	mJ (10^{-3} J)	ft lbf	in lbf
Density	kg/m^3	tonne/ mm^3	slug/ ft^3	$\text{lbf s}^2/\text{in}^4$

Figure 5.1: Consistent units, SI. | Source: ABAQUS/CAE Manual [5]

followed was to have as little intersections between different parts as possible in order to avoid *overconstraint checks* in the **Assembly** module. Overconstraint checks pose a real analysis threat only in the case of fully rigid models and not in the semi rigid approach. The following table briefly highlights them and expands on their properties. Their annotation can be seen in Figure 5.2 through 5.6 .

Their Material & Mesh properties will also be discussed in depth in the next segments.

Geometry Table

Name	Type	Material	Mesh
Back Beams	3D Deformable Wire element	GL30c	B31, Global size: 0.5m, 1207 elements
Back Columns	3D Deformable Wire element	GL30c	B31, Global size: 0.5m, 1230 elements
Back Diag	3D Deformable Wire element	GL30c	B31, Global size: 0.5m, 284 elements
Front Beams	3D Deformable Wire element	GL30c	B31, Global size: 0.5m, 812 elements
Front Columns	3D Deformable Wire element	GL30c	B31, Global size: 0.5m, 837 elements
Front Diag	3D Deformable Wire element	GL30c	B31, Global size: 0.5m, 284 elements
Inner Beams	3D Deformable Wire element	GL30c	B31, Global size: 0.5m, 2858 elements
Inner Columns	3D Deformable Wire element	GL30c	B31, Global size: 0.5m, 1402 elements
Inner Diag	3D Deformable Wire element	GL30c	B31, Global size: 0.5m, 366 elements
RIGID	3D Deformable Wire element	GL30c	B31, Global size: 0.5m, 9309 elements
Facade	3D Planar Shell	CLT	S4, Global size: 2.0m, 2156 elements
Foundation	3D Planar Shell	Concrete	S4, Global size: 2.0m, 152 elements
Truss Shell	3D Planar Shell	CLT	S4, Global size: 0.6m, 6208 elements

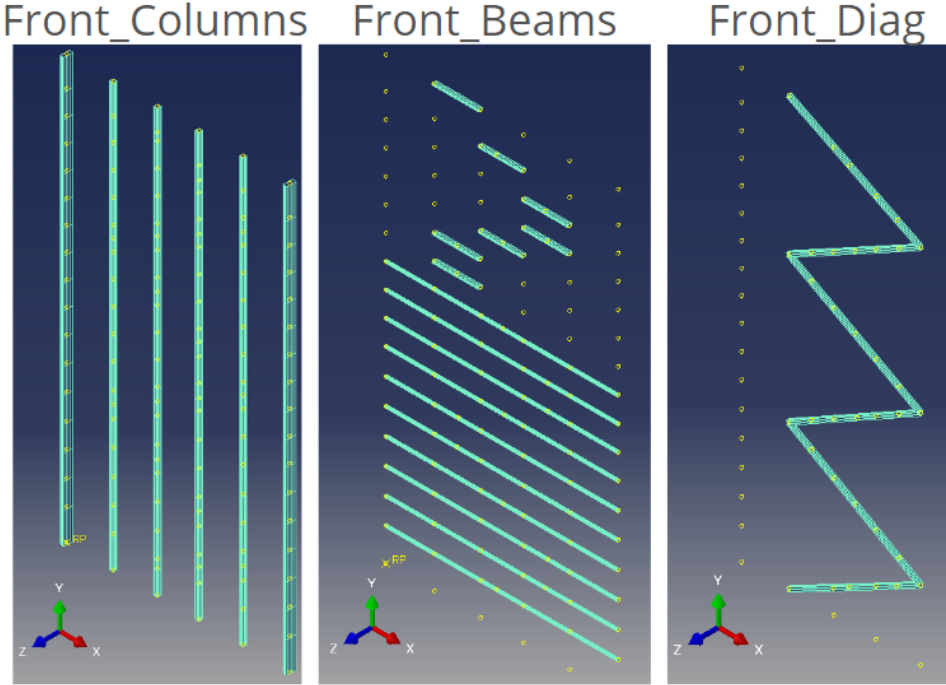


Figure 5.2: Front beam geometry.

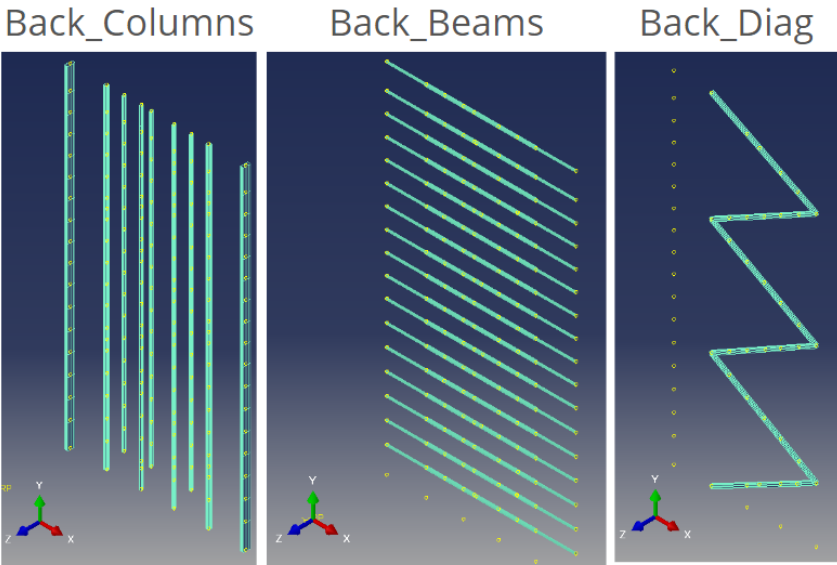


Figure 5.3: Back beam geometry.

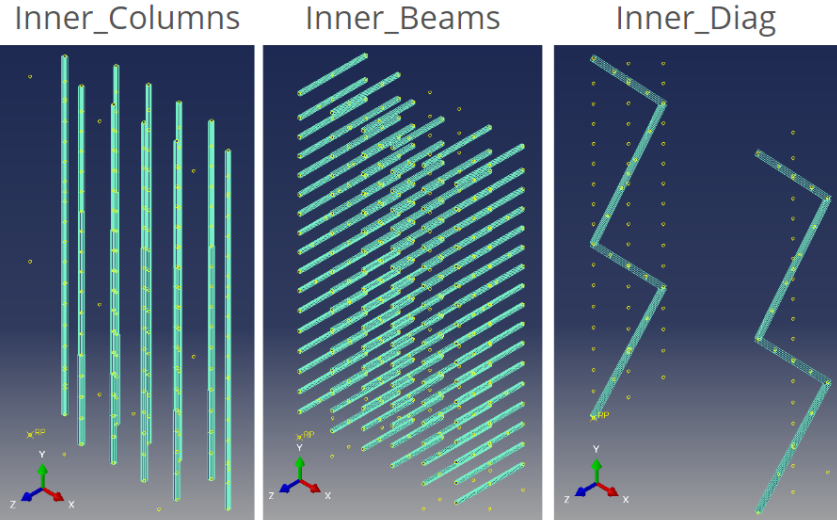


Figure 5.4: Inner beam geometry.

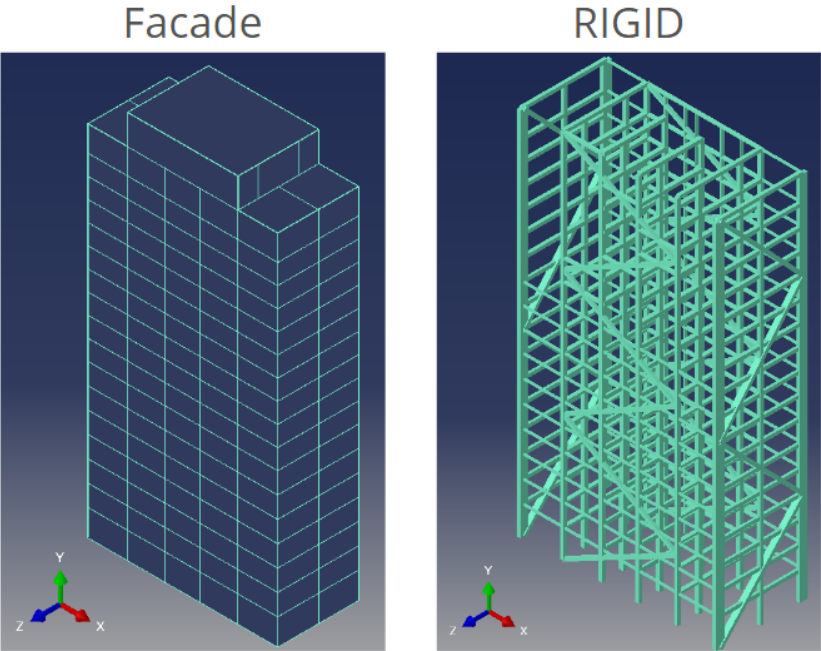


Figure 5.5: Rigid beams and facade shell geometry.

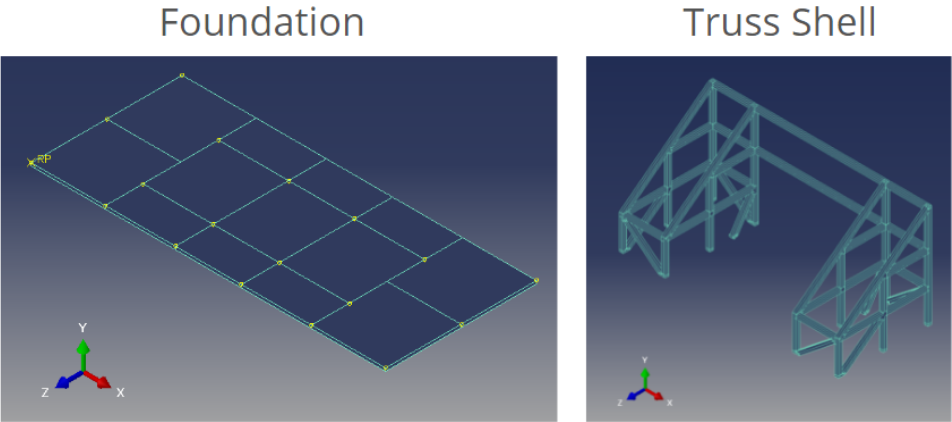


Figure 5.6: Foundation and Truss shell geometry.

It should be noted that during the Sketch procedure, using the *Create Datum Point: Offset* from point tool, the parts must be equipped with corresponding points on their connections. A good practice would be to also check the *Make Independent* box in their creation, so the referencing nodes can be deleted after without altering the whole part and assembly.

It should also be noted that the Frames can be modelled as Wire elements in two ways. They can be sketched using the *Wire: Planar tool* in an appropriate Datum Plane or they can be sketched directly in the Part Module, using the *Create Wire: Point to Point* and connecting two datum Points. If the latter method is used, one should be cautious to create the wires as Disjoint and sketching them keeping in mind the normal direction of the Global Coordinate System(X,Y,Z). This will help in creating the geometry sets and assigning correct element (wire) orientation. Before assigning Material Properties and Section Assignments, the best practice is to create Sets with each corresponding group of section profiles to help visualise them and to save time since those sets will also be transferred to the united rigid model in the assembly module. The following Sets were created in the process which correspond to the different type of Section Profiles, as provided by the *BIM* file. The cross sections sketched would be presented in the Appendix A.

The same principle can be extended in the sketching of the Facade shell. All shell parts should be sketched **counterclockwise** to result in a conventionally positive shell normals. However, the element normals can easily be flipped using the *Assign Element Normal* tool under the property module. Visualisation can be done by looking for the **Brown element faces** to be in the same direction as the Global Coordinate system.

For the Truss shell, the same principle as the Façade shell was followed. Due to complicated geometry, it is recommended to use the *Create Shell: Extrude tool*. This is not the optimal way to model truss beams, since the constitutive behavior of shells regards

only membrane and thin elements and not rectangular beams. A better way to model the beams is as homogenous solid elements, since surface faces are needed for the coupling, however solid elements are computationally more expensive to solve than shells.

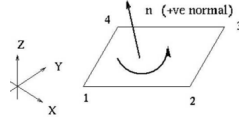


Figure 5.7: Default shell normals orientation.

5.2 Properties

In this module, material property assignment, section assignment and element normals can be configured.

5.2.1 Material properties

The analysis will be restricted on the elastic spectrum due to the innate brittle failure of construction timber. Thus, the materials have linear elastic properties and nonexistent plasticity. Material damping will be applied in the GLULAM frames, because material damping due to cracking, slipping and friction is concentrated near their connections, where shear stress is significant [55]. In *ABAQUS*, orthotropic material properties can be defined by selecting the engineering constants option. For timber, elasticity properties are derived from *EC5* for parallel to grain $k_{,0,d}$ and perpendicular $k_{,90,d}$. Poisson's ratio for GL30c beams was taken from a similar study [56] as well as the Poisson's ratios for the CLT elements [57].

Material	Density kg/m^3	Type	Damping
GL30c	430	Engineering Constants(<i>EC5</i>)	Rayleigh
CLT	430	Engineering Constants(<i>EC5</i>)	(-)
Concrete	2500	Isotropic	(-)
Timber, Norwegian spruce	405	Isotropic (Simplification)	(-)

GL30c, Engineering Constants(EC5)

Parameter	Value	Unit
E1	13000000000	Pa
E2	300000000	(-)
E3	300000000	(-)
Nu12	0.35	(-)
Nu13	0.35	(-)
Nu23	0.1	(-)
G12	650000000	Pa
G13	650000000	Pa
G23	650000000	Pa

CLT, Engineering Constants(EC5)

Parameter	Value	Unit
E1	11000000000	Pa
E2	370000000	(-)
E3	370000000	(-)
Nu12	0.4	(-)
Nu13	0.4	(-)
Nu23	0.1	(-)
G12	690000000	Pa
G13	690000000	Pa
G23	500000000	Pa

Concrete, Isotropic, No Tension Enabled

Parameter	Value	Unit
E	32100000000	Pa
Nu	0.2	(-)

Timber, Norwegian spruce, Isotropic

Parameter	Value	Unit
E	9700000000	Pa
Nu	0.3	(-)

5.2.2 Assigning material normals

As mentioned previously all element normals will be designed to point in the same direction as the global coordinate system.

This can be visualised in the **Property** module, under Assign- Beam orientation, for wire elements and Element normal for shell elements.

The local coordinates of the wire elements are as shown in the figure below,

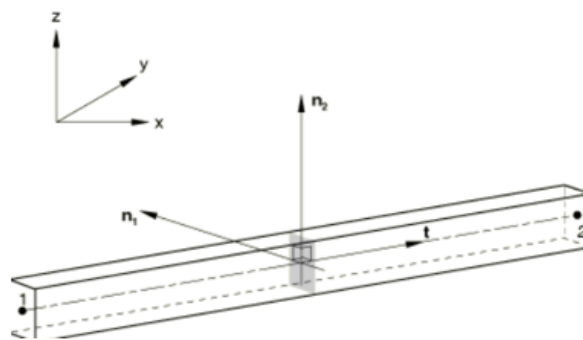


Figure 5.8: Beam normals orientation.

For the Wire elements in the YX datum planes:

- Columns and Diagonal elements (0,0,1)
- Beams (0,0,-1)

The Wire elements in the YZ datum planes:

- Diagonal elements (1,0,0)
- Beams (1,0,0)

5.2.3 Material damping of GL30C

Material damping will be applied in the GL30c. In *ABAQUS* the material damping can be defined as:

- Composite modal damping
- Rayleigh damping
- Structural damping

As mentioned before in 3.2.1, the overall damping of Mjostarnet has been identified as $\xi = 1.5\%$. Overall damping can be applied via Rayleigh damping coefficients α and β or via the parameter ξ_{st} in structural damping. Structural damping assumes that the damping forces are proportional to the forces caused by stressing of the structure and are opposed to the velocity. However, this form of damping can be used only if the displacement and velocity are exactly 90° out of phase, which is the case when the excitation is sinusoidal, so structural damping can be used only in steady-state and random response analysis and not in a Dynamic Analysis.

Rayleigh damping is defined by a damping matrix formed as a linear combination of the mass and the stiffness matrices:

$$\mathbb{C}^{\text{MN}} = \alpha * \mathbb{M}^{\text{MN}} + \beta * \mathbb{K}^{\text{MN}} \quad (5.1)$$

Factor α introduces damping forces caused by the absolute velocities of the model and simulates the model moving through a viscous “ether” (a permeating, still fluid, so that any motion of any point in the model causes damping). This damping factor defines mass proportional damping, in the sense that it gives a damping contribution proportional to the mass matrix for an element.

Factor β introduces damping proportional to the strain rate. It defines damping proportional to the elastic material stiffness. Since the model may have quite a general nonlinear response, the concept of “*stiffness proportional damping*” must be generalised, since it is

possible for the tangent stiffness matrix to have negative eigenvalues (which would imply negative damping). To overcome this problem, it is interpreted as defining viscous material damping in *ABAQUS*, which creates an additional “damping stress,” σ_d , proportional to the total strain rate:

$$\sigma_D = \beta * \mathbb{D} * \dot{\epsilon} \quad (5.2)$$

It is generally preferable to damp out low frequency responses with mass proportional damping rather than stiffness proportional damping. However, mass proportional damping can significantly affect rigid body motion, so large α is often undesirable. To avoid a dramatic drop in the stable time increment and numerical instability, the stiffness proportional damping factor, β , should be less than or of the same order of magnitude as the initial stable time increment without damping. Conclusively, for the fully rigid model mass proportional damping will be used to simulate the overall damping in order to get better and faster convergence.

In contrast, for the semi rigid modelling on the basis that damping is additive [58], the factor β will only be employed to simulate stiffness proportional damping in the connections equal to $\xi_{st} = 1.5\%$, whilst factor α will be used to employ the material damping intrinsically in GLULAM beams equal to $\xi_{glulam} = 1.1\%$.

Mass proportional damping

The lowest eigenfrequency which stimulates the along wind oscillations, is calculated as $f_1 = 0.5Hz$ from transient spectral analysis performed in Mjøstårnet, whilst the highest $f_3 = 0.85Hz$ corresponds to torsional excitation.

$$\xi_i = \frac{\alpha}{2\omega_i} + \frac{\beta * \omega_i}{2} \quad (5.3)$$

For the Rigid and SSI model (*Model 1 and 3*), both Rayleigh factors will be used to emulate the equivalent overall damping of $\xi_{st} = 1.5\%$. By solving the above equation, the

factor of α for the $\omega_1 = 3.14159rad/s$ and the factor of β for $\omega_3 = 5.341rad/s$.

$$\beta = \frac{2 * \xi}{(\omega_1 + \omega_3)}$$

$$\alpha = \frac{2 * \xi * \omega_1 * \omega_3}{((\omega_1 + \omega_3))}$$

By substituting,

$$\beta = 0.00381972$$

$$\alpha = 0.05654697$$

In contrast, for the semi-rigid Model (*Model 2*) Rayleigh damping will also be used, however the mass damping factor α will solely be used to emulate the damping that occurs because of the internal friction of GLULAM beams, $\xi_{glulam} = 1.13\%$. Stiffness damping factor β will be used to simulate the damping that occurs near the connections due to cracking and slipping of dowels $\xi_{st} = 1.5\%$. The range of its damping effects will be minimised in the first three angular velocities in the same fashion as in the rigid scenario.

$$\beta = \frac{2 * \xi_{st}}{(\omega_1 + \omega_3)}$$

$$\alpha = \frac{2 * \xi_{glulam} * \omega_1 * \omega_3}{((\omega_1 + \omega_3))}$$

By substituting,

$$\beta = 0.0064$$

$$\alpha = 0.0628$$

5.2.4 Slab damping

Regarding the damping in the semi-rigid model (*Model 2*), in order damp out the corresponding frequencies via Rayleigh damping, a damping analysis should be run first. This can be done by implementing a *Modal Analysis* after a *Frequency Analysis*.

After the analysis has been finished, the following *History Output* reports will be created:

- Composite Modal Damping, CD
- Effective mass
- X-component, Y-component and Z-component
- X-rotation, Y-rotation and Z-rotation

Available literature gives damping ratios under crash tests in floors, because their main concern is the in-plane vibrations of the floor which relate to the acoustic impedance of the structural system [59]. By following that train of thought, the objective is to identify the eigenvalues which dominate the *Y – component* excitation, in order to apply the appropriate floor damping.

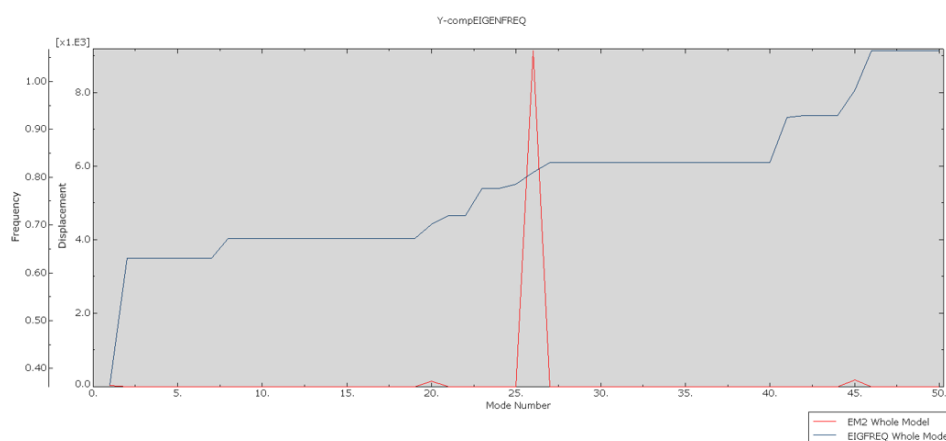


Figure 5.9: Y-component excitation modes.

It becomes apparent that the **Mode N.26** dominates the Y-component. The corresponding eigenfrequency is $f_y = 0.81026Hz$ and the angular velocity $\omega_y = 5.0910137212rad/s$. The slabs will be simulated as single point masses in the *Interaction* module. As a zero length inertia point, only mass proportional damping can be applied.

For the damping of composite timber concrete floors,

$$\xi_y = \frac{\alpha}{2 * \omega_y} \implies \alpha = \xi_y * 2 * \omega_y = 0.07 * 2 * 5.0910137212 = 0.7127419208$$

For the damping of timber floors,

$$\xi_y = \frac{\alpha}{2 * \omega_y} \implies \alpha = \xi_y * 2 * \omega_y = 0.011 * 2 * 5.0910137212 = 0.11200230184$$

5.3 Assembly

The assembly module will be different for each one of the four (4) separate models. ABAQUS does not automatically recognize the contact between parts, therefore contact constraints should be assigned between them to ensure seamlessness.

This can be done by:

1. Translating each Instance part to their corresponding location and then using the tool *Merge Instances*.
 - For solid parts, the tool *Translate To* should be used to create contact between faces. For the rest of the element types only the *Translate Instance* tool is applicable.
 - Select *Merge Geometry*. Merging meshes instead of geometry will be computationally expensive for the Interactions later.
 - ABAQUS should be prompted to remove any intersecting boundaries. By this option each part will be rigidly connected to the rest, meaning each intersecting node will have 6 *D.O.F.*
2. For the shell elements, it is applicable and often preferred to use the tools *Create Constraint*. Translational arrows should point in the same direction.
 - For intersecting Edges (such as is the case in the main rectangular facade of Mjøstårnet if each side is modelled separately, the tool *Create Constraint: Edge to Edge* should be used.
 - For modelling the contact between the Truss shell and the facade, *Face to Face* can be used to unite the bottom faces of the Truss with the top faces of the facade.
3. For the shell elements, it is also possible to simulate their connection using *Attachment Points* and rigid fasteners. However, this technique is both computationally

heavy and demands an unprecedented amount of precision by the user for this type of application.

4. For the wire elements, it is possible to create *MPC* between datum points of different parts. This can be done in the Interaction section and will be discussed later.

5.3.1 Fully rigid connections (Model 1)

For the fully rigid model (*Model 1*), in order to avoid overconstraint checks, one simple united model will be generated through the joining of different *Parts*. Under the Assembly-Instances tree, one should select all the *Parts* created and assign them to a *Dependent Instance*. This basically means that all the *Parts* should be meshed on the respective module. Meshing can therefore predate the Assembly step.

After successfully generating each part in the assembly, one should group them by type of elements meshed. For example, suppress or Hide the shell element parts so that only the wire element parts can be viewed, then merging them. Note that the new part should be assigned beam orientations and be meshed again, however if appropriate *Geometry Sets* were created before the merging, they will continue to exist in the merged part. That way the selection of elements is easy and not time consuming. The connection between the Rigid frames and the shell elements will be modelled by *Constraints* and *Interactions*, and as such it will be discussed further below.

5.3.2 Semi Rigid Connections (Model 2)

For the Semi rigid model, the user will need to connect manually each datum point of intersecting part by creating unique Wire Features corresponding to different types of connections. The Wire Features will be zero length elements with assigned stiffness. It is possible to assign more than one stiffness matrix per zero length element. This will be done to include the reduced stiffness between GLULAM connections.

As mentioned previously in the theory segment 2, the stiffness in timber connections is dependent on three parameters.

- $K_{ser,d}$, is the stiffness existing in the shear planes of the connection
- $K_{ser,\theta}$, is the rotary stiffness perpendicular to the dowel direction
- K_w , is the withdrawal resistance parallel to the dowel direction

That being said, under the ***Interaction*** module wire connectors (*CONN3D2 elements*) will be used to simulate the timber connections. Note that stiffness is multiplied by the number of dowels existing and as such, the stiffness will be doubled in crosswise connections.

5.4 Interactions

In the Interaction module, the following properties will be modelled:

1. Point masses and their distribution to each floor
2. Connection interaction between different parts
3. SSI springs and dashpots
4. Tie constraints

5.4.1 Point masses

One of the core simplifications made, was the simulation of slab inertia and weight by point masses and diaphragm conduct. According to the *BIM* file and *MOELVEN*, the following prefabricated slabs were used:

- **Floor 3-11**, Metsä timber floors
- **Floor 12-18**, Prefabricated composite concrete floors

The absolute weight (W) of each floor was calculated by multiplying the *Volume* (derived from the *BIM* file) with the appropriate material density. The rotary inertia (I) of each floor was applied only in the I_{22} direction, in order to affect only the torsional responses. Furthermore, for the calculation of the angular mass the following equations was used [60].

$$I_c = \frac{1}{12} * m * (l_x^2 + l_y^2) \quad (5.4)$$

, where l_x is the width of the building perpendicular to the wind flow, whereas l_y is the length parallel to the wind flow. The calculations can be viewed in the following table.

Floor(s)	Density (kg/m^3)	Volume (m^3)	Mass (kg)	Rotary Inertia ($kg * m^2$)
3-11	430	149.597	64326.71	8163595.555
12-17	2300	149.597	344073.1	43665743.67
18	2300	162.256	373188.8	47360768.63

To attach the mass/inertia points to the *Assembly*, first a *reference point* for each floor must be created.

Having assumed that the axis of rotation is in the center of the slab, the reference point should have coordinates that coincide with this assumption. *Reference points* can be created in the *Interaction* module by the *Tools- Reference Point* tool. Subsequently, inertia points can be created and attached by the *Special- Inertia Manager* tool. It should be noted that, since the masses were created in the Assembly module, *ABAQUS* doesn't recognize their contact with the other parts. Thus, they must be connected rigidly with a beam connector, to at least 3 other points in the diaphragm and then their masses should be distributed on the floor via coupling constraints. Neither of those points should not coincide in the same line as their purpose is to restraint the 3 translational and rotational *DOFs*.

To create the diaphragm constraints, select in the Manager tab a *Coupling* type constraint. There are 3 options given, however, to avoid overconstraint checks one should select the *Continuum or Structural distribution* option since they do not conflict with the *DOFs* of the slave surface. The constrained *DOFs* will include all the translational ones as well as the *UR2*. As slave surface, all the nodes in each floor will be selected except the Reference Points created. Selecting the *RPs* as well in the selection will result in Zero Pivot errors. Note, that for each floor another constraint ought to be created.

5.4.2 Interaction between shell and wire elements

In *FEA* it is generally recommended to avoid coupling different mesh types. For that reason, the preferable method of interaction between those elements is to set up a *MPC constraint*, meaning, to couple their *DOFs* in a single node [61].

This technique was followed for the interaction between the foundation shell and the frames, whilst the facade shell interacts with the frames using a *Tie constraint*. The same principle applies to the interaction between the Truss shell and the facade shell, due to the ability of a Tie constraint to connect effectively regions of different meshing.

Foundation- Frames

1. Using the *Create Wire Feature* tool, connect with zero length elements the contact nodes of the frame columns and the corresponding nodes of the foundation.
2. Using the *Create Connector Section* tool select on the *Basic* connection category tab,
 - For the Rigid model (**Model 1**), select the *Translational type as Join* and the *Rotational type as Align*. This will ensure that the *DOFs* between the 2 nodes selected will be identical.
 - For the Semi Rigid model (**Model 2**) , select Cartesian and Rotation respectively. Proceed to assign Elasticity and Integration.

Frame end- Frame start, (Model 2)

- (a) Using the *Create Wire Feature* tool, connect with zero length elements the contact nodes of the frame columns and the corresponding nodes of the foundation.
- (b) Using the *Create Connector Section* tool select on the *Basic* connection category tab:

- For the Semi Rigid model, select Cartesian and Rotation respectively. Proceed to assign Elasticity and Integration and Friction-Penalty.

The extensive calculations and stiffness properties can be viewed in the Appendix B.

The following Sets of *zero length* elements were created:

Set(s)	Start	End	$K_{ser,d}$	$K_{ser,\theta}$	K_w
1,2	BackBeams	BackColumns	D11, D22	D66	D33
3	InnerBeams	BackColumns	D22, D33	D44	D11
4	InnerBeams	FrontColumns	D22, D33	D44	D11
5	InnerBeams	FrontColumns	D11, D22	D66	D33
6	BackDiag	BackBeams	D11, D22	D66	D33
7	FrontDiag	FrontBeams	D11, D22	D66	D33
8	FrontDiag	FrontColumns	D11, D22	D66	D33
9	Foundation	InnerColumns	D11, D22	D66	D33
10	Foundation	OuterColumns	D22, D33	D44	D11
11,12	FrontBeams	FrontColumns	D11, D22	D66	D33
13,14	InnerBeams	InnerColumns	D22, D33	D44	D11
15	SideDiag	BackColumns	D22, D33	D44	D11
16	SideDiag	FrontColumns	D22, D33	D44	D11
17	SideDiag	SideColumns	D22, D33	D44	D11
18	SideDiag	InnerBeams	D22, D33	D44	D11

Facade-Frame

For this interaction, Tie constraints will be used.

- Firstly, create a unified surface for the rectangular facade. Use the *Flip a Surface* tool, to orient all surfaces in a way that their normals will be directed out of the frame sections.
- Do the same for the columns. Select *Yellow End* if the beam orientation had been assigned as $(0,0,-1)$.
- In the Create Constraint dialog, select Tie and check *Surface to Surface* discretization method.
- Check both options of *Adjusting slave surface initial position* and *Tie rotational DOFs*. If the slave surface initial position is left unchecked, then it is recommended to create an additional Step in which a small amount of deformation displacement will be applied as a *BC* for the surfaces to come in contact. This will reduce the computational residuals and increase convergence.

Assigning a surface as either **Master (Facade)** or **Slave (Column)** must be decided according to these 3 rules of thumb,

1. The Master surface should be the one in which the loads are applied.
2. The Master surface can penetrate the mesh of the slave surface. Therefore, the Slave surface should be the one with a finer mesh.
3. The Master surface should be the material which is stiffer. That way the penetration in the slave surface can be avoided.

Facade-Truss shell

For this interaction, *Tie constraints* will be used. Another way to model their interaction is by using *Fasteners* or *Contact constraints*.

Repeat the process above, selecting as Slave surfaces the bottom faces of the truss, and as **Master** surface the top shell of the Facade.

Superstructure- SSI

There are two common ways to simulate the *SSI* in *ABAQUS*.

The first way would be to create another **3D Solid** part for the soil as well as individual solid piles. The second method, which will be the one used, is to decouple the kinetic and inertial behaviour of the foundation. This method faces certain limitations and is better used during linear elastic analysis of the soil medium. It should also be noted that *SSI* analysis has been limited so far in seismic design and shear waves excitation, and not wind loading (with the exception of monopile wind turbines).

The kinematic response of the Foundation Input Motion (*FMI*) will be simulated by the calculated wind load induced stresses that reach the foundation level, whilst the dynamic interaction will be simulated by using **dashpots and springs** with appropriate values taken from the *Dynamic Impedance* matrix that is calculated below.

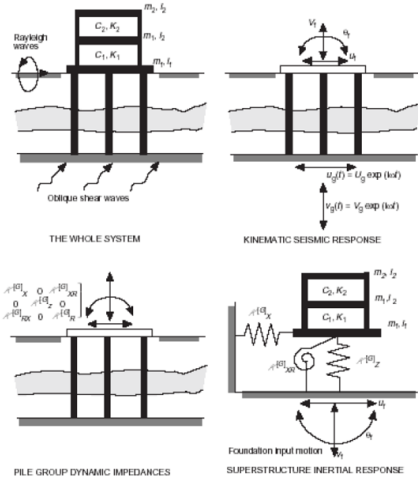


Figure 5.10: Decoupling SSI| Source: Graduate course ASTE07 by Dimitris Pitilakis.

Since the plans of the foundation and the soil characteristics were not readily available by the time of writing this thesis, a draft foundation plan was created.

The pile group consists of 15 piles, arrayed in 3 rows and 5 columns. Every pile is considered identical to the other. The perpendicular distance between each pile is 5 meters. The number of piles, their in-between distance as well as their diameter was chosen in accordance with the typical floor's lengths (37x17) m. The depth of the bedrock is 130m below the surface level, and thus was used as the pile's length also.

The soil medium properties such as soil density ρ_{soil} , modulus of elasticity E_{soil} and undrained strength C_u were chosen out of approximation. *J. Lag & Norges Landbrukshogskole*[62] have created a national soil survey map for Norway that is readily available. The dominant soil profile in the location of Mjøstårnet, is brown earth with high and medium saturation as well as podzols, in agreement to approximate values of Silty Clay derived from *CPT* tests [63]. In this segment the methodology and the application in *ABAQUS* will take place, however the extensive calculations as well as the matrices can be viewed in the Appendix C.

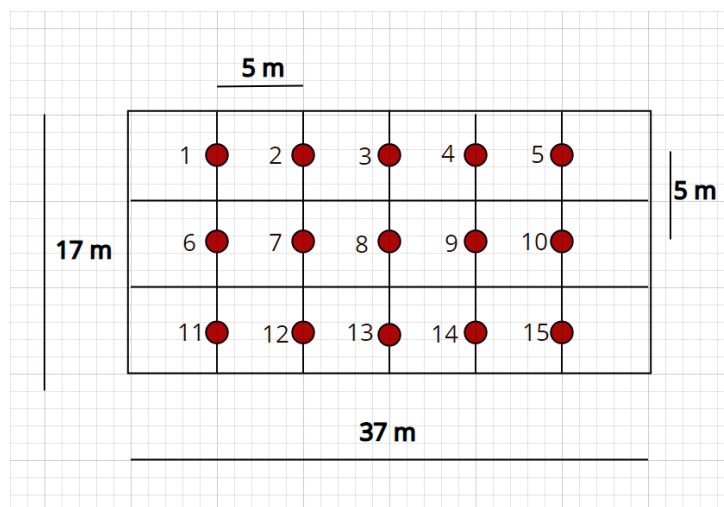


Figure 5.11: Piled raft foundation plan.

The geometry of the piles as well as the predefined soil properties were elected as:

Pile group information		
Property	Value	Unit
Distance between piles	$S = 5$	(m)
Distance to pile diameter ratio	$S/D_p = 3.33$	(-)
Pile length	$L_p = 130$	(m)
Length to pile diameter ratio	$L_p/D_p = 86.67$	(-)
Modulus of elasticity	$E_{C30,p} = 30000$	(MPa)
Pile density	$\rho_{C30,p} = 2200$	(kg/m ³)
Soil medium information		
Property	Value	Unit
Shear wave velocity	$V_s = 200$	(m/s)
Soil density	$\rho_{soil} = 20$	(kg/m ³)
Material damping	$\beta_s = 0.05$	(-)
Undrained shear strength	$C_u = 40000$	(Pa)
Concrete Pile elasticity to soil ratio	$E_p/E_s = 1000$	(-)

The active length of an individual pile, L_a , and the radiation velocity V_a can be calculated using the formulas proposed by *Randolph*(1981):

$$\text{Active pile length: } L_a = 1.5 * \left(\frac{E_p}{E_s}\right)^{0.25} * D_p = 12.6527m \quad (5.5)$$

$$\text{Pile weight: } w_p = A_p * \rho_{CEM} = 4.417tn/m \quad (5.6)$$

$$\text{Pile inertia: } I_p = \frac{\pi}{4} * r^4 * 0.2485m^4/m \quad (5.7)$$

$$\text{Active radiation velocity: } V_a = 3.4 * \frac{V_s}{\pi} * (1 - \nu) = 360.751 m/s \quad (5.8)$$

In a group pile, each pile's individual response is affected by a certain degree from the response of the other individual piles in the group, thus being subjugated in the group piled effect.

The group pile effect, based on the *Superposition Principle*, can be modelled by the multiplication of a single pile's dynamic impedance $K^{[1]}$ with the matrix of dynamic interaction coefficients $\epsilon_{(i,j)}$.

$$K_{dyn}^G = \begin{bmatrix} K_{xx}^G & K_{xr}^G \\ K_{rx}^G & K_{rr}^G \end{bmatrix} = \begin{bmatrix} K_{xx}^1 * \sum_{i=1}^N \sum_{j=1}^N \epsilon_{xx}^{ij} & K_{xr}^1 * \sum_{i=1}^N \sum_{j=1}^N \epsilon_{xr}^{ij} \\ K_{rx}^1 * \sum_{i=1}^N \sum_{j=1}^N \epsilon_{rx}^{ij} & K_z^1 * \sum_{i=1}^N x_i \sum_{j=1}^N x_j * \epsilon_{rr}^{ij} \end{bmatrix} \quad (5.9)$$

The matrix refers to a 2D problem (the vertical stiffness is infinite, and the vertical damping is zero). To project this problem to a 3D space, it is assumed that the same conditions are present in the other direction as well.

To use the generic impedance matrix of a single pile $K^{[1]}$, the following requirements must be met:

1. The actual length of the pile should be bigger than the active length and
2. the soil profile is homogeneous.

$$K_{dyn}^1 = \begin{bmatrix} K_{xx}^1 & K_{xr}^1 \\ K_{rx}^1 & K_{rr}^1 \end{bmatrix} = \begin{bmatrix} 4 * E * I * \lambda^3 & 2 * E * I * \lambda^2 \\ 2 * E * I * \lambda^2 & 2 * E * I * \lambda \end{bmatrix} \quad (5.10)$$

$$\lambda = \left\{ \frac{k_x + i * \omega * c_x - m * \omega^2}{4 * E_p * I_p} \right\}^{1/4} \quad (5.11)$$

As mentioned earlier at the theory segment 3.3.1, the lateral stiffness and damping of a single pile can be simplified by a line of *Winkler* spring properties, k_x and c_x respectively. While there are many formulas proposed in literature to approximate the lateral stiffness, the most simplified one will be used. The other formulas will also be available in the Appendix C.

Firstly the calculation of the dynamic parameters is as follows:

Pile group information		
Property	Value	Unit
Modulus of elasticity	$G_s = \rho_s * V_s^2 = 80000$	(kPa)
Modulus of shear	$E_s = 2 * G_s * (1 + \nu) = 224000$	(kPa)
Eigenperiod of piles	$T_o = 4 * \frac{H}{V_s} = 2.6$	(s)
Eigenfrequency of piles	$\omega_o = \frac{2*\pi}{T_o} = 2.41661$	(rad/s)
Dimensionless eigenfrequency of piles	$a_o = \omega_o * \frac{D_p}{V_s} = 0.01812$	(-)

$$k_x = 1.2 * E_s = 268.8 \frac{MN}{m^2}, \text{ Makris and Gazetas (1992)} \quad (5.12)$$

Regarding the damping coefficient, c_x , a complex formulation will be used to account for both hysteresis and radiation damping.

$$c_x \simeq 2 * a_0^{-1/4} * \rho_s * V_s * D * \left[1 + \left(\frac{V_{La}}{V_s} \right)^{5/4} \right] + 2 * \beta_s * \frac{k_x}{\omega} = 10.10708537 \frac{MN * s}{m^2} \quad (5.13)$$

Lastly, the dynamic impedance matrix of a single pile is:

$$K_{dyn}^1 = \begin{bmatrix} K_{xx}^1 & K_{xr}^1 \\ K_{rx}^1 & K_{rr}^1 \end{bmatrix} = \begin{bmatrix} 808.78781118286 - 3.43349345162784i & 1345.96158857224 - 3.80926848252556i \\ 1345.96158857224 - 3.80926848252556i & 4479.81274006478 - 6.33925048539393i \end{bmatrix} MN/m$$

After the previous set of parameters has been identified and the dynamic impedance matrix of a single pile has been defined, the next step is to calculate the matrix of dynamic group fixed head pile interaction coefficients (*Mylonakis 1995 Makris and Gazetas 1992*), where:

- ϵ_{xx} refers to the lateral translational interaction between 2 piles
- $\epsilon_{xr} = \epsilon_{rx} = \frac{1}{3} * \epsilon_{xx}$ refers the translational- rotational interactions between 2 piles
- $\epsilon_{rr} = \frac{1}{3} * \epsilon_{xx}$ refers to the rotational interaction between 2 piles

$$\epsilon_{xx} = \frac{U_{21}(0)}{U_{11}(0)} = \frac{3}{4} * \psi(r, \theta) * \frac{k_x + i * \omega * c_x}{k_x + i * \omega * c_x - m * \omega^2} \tag{5.14}$$

The interaction properties depend on the distance between those 2 piles and the excitation angle. The kinematic coupling between them exists in a displacement field, where U_{11} is the displacement of the first pile and U_{21} is the displacement of the second pile.

It becomes clear that the displacement on the second pile due to the soil displacement caused by the first pile will be getting meeker relative to their in-between distance. Those 2 functions are correlated by the dimensionless weakening coefficient ψ [64].

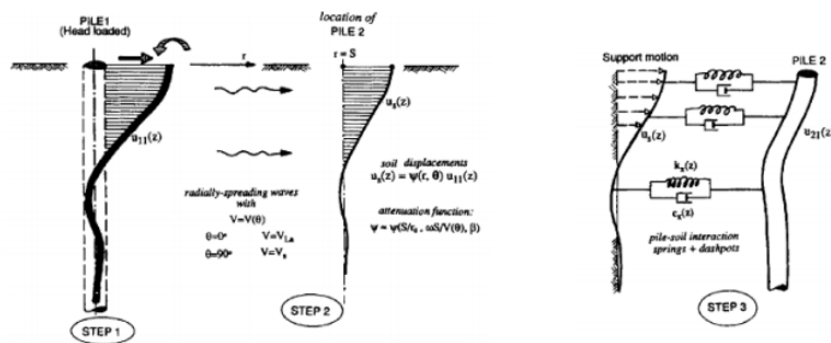


Figure 5.12: Group pile kinematic interaction| Source: Graduate course ASTE07 by Dimitris Pitilakis.

Presuming the (*FMI*) is solely stresses causes by the wind loading on the facade, it can be assumed that the piled foundation is loaded laterally

$$\psi(S, \frac{\pi}{2}) = (\frac{2 * S}{D_p})^{-0.5} * \exp \left[- (\beta_s + i) * (\frac{S - D_p/2}{D_p}) * a_0 \right] \tag{5.15}$$

Since the foundation is comprised by 15 piles, the matrices created will be (15x15). Those matrices will also link the real and imaginary part of the dynamic impedance matrix.

The dynamic impedance matrix of the group pile is:

$$K_{dyn}^G = \begin{bmatrix} K_{xx}^G & K_{xr}^G \\ K_{rx}^G & K_{rr}^G \end{bmatrix} =$$

$$\begin{bmatrix} 58922.661450952 - 4224.12359088665i & 89413.73117936 - 6131.56332763266i \\ 89413.73117936 - 6131.56332763266i & 182411.920042567 - 10040.8948446904i \end{bmatrix} MN/m$$

In the simplified *SSI* model (**Model 3**) *Springs/Dashpots* under the **Interaction, Special** module were used to simulate the overall soil-group pile stiffness and dashpots to simulate the damping. *Connect to ground* spring/dashpot elements were used. The spring elements were applied in the start level of the columns.

Since the pile ends are fixed on the bedrock, the Y translational *DOF* will be set in the *BC*, so one should create only (5) springs for each remaining *DOF*. *ABAQUS* annotation on *DOF* can be visualized below.

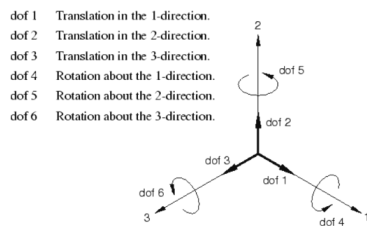


Figure 5.13: Single point’s degrees of freedom. |Source: *ABAQUS/CAE* manual

Conclusively, the following parameters were set,

1. Spring/Dashpot in (1) Direction = Spring/Dashpot in (3) Direction

- $K_x=5.89227E+10$ N/m
- $C_x=4.22412E+09$ Ns/m

2. Spring/Dashpot in (4) Direction=Spring/Dashpot in (5) Direction

- $K_x=8.94137E+10$ N/m
- $C_x=6.13156E+09$ Ns/m

3. Spring/Dashpot in (6) Direction

- $K_x=1.82412E+11$ N/m
- $C_x=1.00409E+10$ Ns/m

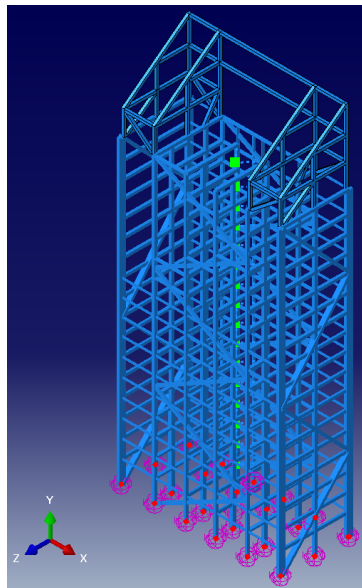


Figure 5.14: Springs/Dashpots connected to columns

5.5 Steps

In the **Step** module, the sequence of the Analysis can be defined. It is also generally encouraged to do some ‘*dummy*’ static analysis in order to check the convergence of the model and its rigidity. For the FSI purpose, it is vital to check:

- The rigidity of the *FEM* and the interaction of said connections by applying a *Static, General* pressure on the facade.
- Record and evaluate the eigenfrequencies of the model by performing a *Frequency* linear perturbation analysis.
 - In the case where the real natural frequencies of the buildings are known, the evaluation is simply numerical.
 - For buildings that are nearly symmetrical in elevation and plan, *EC8* proposed that the first dominant eigenfrequencies should be translational, followed by the flexural and rotational ones.

After those checks, a dynamic procedure must be created to study the transient wind loads. Those can be:

1. *Modal Dynamics*, initializing from the Frequency procedure. Modal dynamics can be used only in linear elastic systems and to identify the composite modal damping. It has been used for the identification the dominant Y-mode for **Model 2**.
2. *Dynamic, Implicit*. Can be used in linear and nonlinear problems and uses direct time integration. Can be used as a *Co-Simulation* option with *Star – CCM+*. This option was chosen for the coupling procedure.
3. *Dynamic, Explicit*. Can be used in linear and nonlinear problems and used direct time integration in addition to lumped mass matrices. Can be used as a *Co-Simulation* option with *Star – CCM+* but is significantly more computationally expensive.

NLgeom takes into account second-order effects, meaning that the deformed geometry of the model will be used in each time integration to calculate the next step's deformations and stresses. It is not required for a non-linear analysis without big deformations. However, since enabling *NLgeom* provides more accurate results and big deformations are expected as the wind loads reach the critical velocity, it will be turned on.

For the Dynamic, Implicit analysis the following values were used:

Property	Value
Time period	30s
NLgeom	(ON)
Max. number of increments	(1000)
Initial increment size	(0.001)s
Min. increment size	(1E - 09)s
Max. increment size	(0.1)s
Numerical damping <i>HTT</i>	(-0.005)s

5.6 Loads

Here both *BCs* and step *Loads* can be set.

5.6.1 Boundary Conditions

For all models except the one with the *SSI* enabled, Model 1, Model 2, Model 4 ,the foundation shell and the nodes of the facade at $Y = 0$ shall have all of their *DOFs* rigidly constrained from the *Initial* step, using the *Encastre* option.

For the model with the *SSI* (**Model 3**), only the translational degree of freedom [*U2*] will be rigidly constrained, which corresponds in the gravitational translation; the piles are welded in the bedrock.

5.6.2 Load Conditions

For the *FSI*, it is desirable to create Pressure Loads that will act on the facade in the *Dynamic, Implicit* step as boundary conditions. This will ensure:

- The validity of the model and the time step during a test iteration,
- faster convergence during the coupling procedure.

Below are the test pressures for each coupling model and the corresponding acting *Surfaces*:

Critical wind speed fraction	BackFacade	FrontFacade	Right & LeftFacade
$V_h/nW=2$	$200Pa$	$100Pa$	$80Pa$
$V_h/nW=4$	$300Pa$	$150Pa$	$100Pa$
$V_h/nW=6$	$400Pa$	$200Pa$	$120Pa$
$V_h/nW=8$	$600Pa$	$300Pa$	$200Pa$
$V_h/nW=10$	$800Pa$	$400Pa$	$300Pa$
$V_h/nW=11.1$	$1000Pa$	$500Pa$	$400Pa$

5.7 Meshing

A lot of attention was given in proper meshing, since most numerical errors can be attributed to bad cells and/or a bad mesh continuum.

It is of paramount importance to mesh the wire elements finer than the facade since they are incorporated as the **Slave surface** in *Tie* constraints. That being said, in the tie constraint between *Columns* and the *Facade*, it is good practice to align the edges of the meshed cells of the facade to osculate with the wire elements. This can be achieved by manually **Partitioning** the surfaces, as it will be later in this section.

5.7.1 Wire Elements

All parts with wire elements are meshed as *B31* elements, a 2-node linear beam in space (6 *DOFs*). Global seeds were applied and created with a size of $0.5m$. No partitioning was done. After meshing the Validity was checked by using the tool *Verify Mesh*.

```
1 #Part: RigidFrames
2 #Number of elements: 9309, Analysis errors: 0 (0%), Analysis
   warnings: 0 (0%)
```

The same values and mesh element was used for the individual parts of the semi-rigid (**Model 2**).

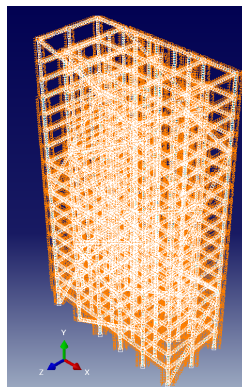


Figure 5.15: Rigid frame mesh seeds.

5.7.2 Shell Elements

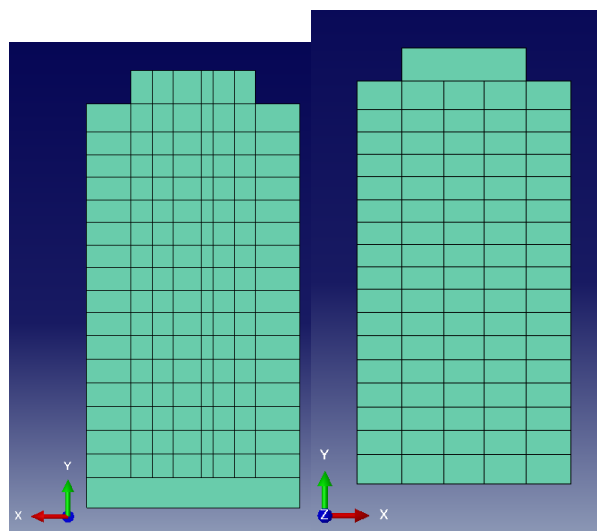
For the *Facade* part all shell elements are meshed as *S4R* elements, a 4-node doubly curved thin or thick shell, reduced integration, hourglass control, finite membrane strains. *Reduced integration* option is checked for computational efficiency, since using reduced integration will basically mean it will take less time to run the analysis, but it could have a significant effect on the accuracy of the element for a given problem. Displacement-based FE formulations always over-estimate the stiffness matrix and the use of fewer integration points should produce a less stiff element.

Global seeds were applied and created with a size of $2.0m$. Surface partitioning was done in order for the shell edges to match the column wires, as shown below. After meshing the Validity must be checked by using the tool *Verify Mesh*.

Everything mentioned for the facade part applies to the foundation shell as well.

```
1 #Part: Facade
2 #Number of elements : 2156, Analysis errors: 0 (0%), Analysis
  warnings: 0 (0%)
```

Partitioned facade surfaces.



Partioned facade surfaces.

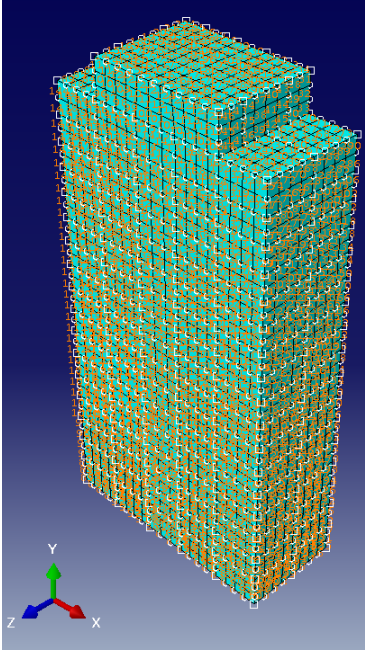
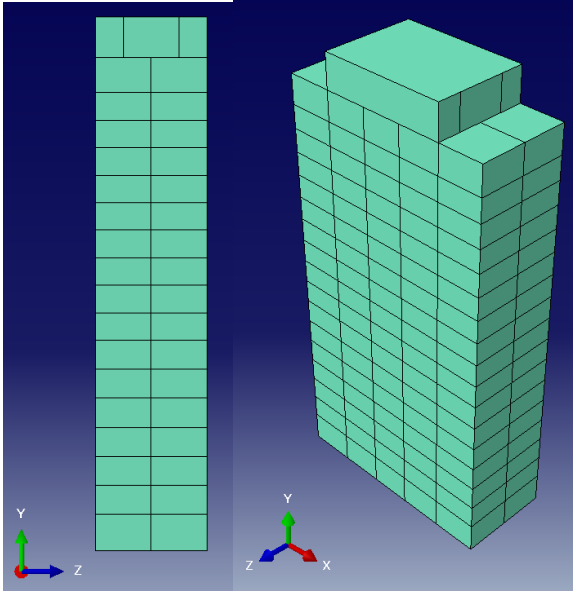


Figure 5.16: Facade shell mesh seeds.

For the *Truss Shell* part all shell elements are meshed as *S3* elements, a 3-node triangular general-purpose shell, finite membrane strains. Another *Mesh* control was applied for the better meshing of the Part, *Tri* elements with mapped meshing. This was done due to the complex geometry of the part. Global seeds were applied and created with a size of $0.6m$. Surface partitioning was done in order to simplify the complex geometry into simpler shapes, ones that the meshing algorithm can handle effectively. After meshing the Validity must be checked by using the tool *Verify Mesh*.

```
1 #Part: TrussShell
2 #Number of elements : 6208, Analysis errors: 0 (0%), Analysis
  warnings: 6 (0.0966495%)
```

Partitioned facade surfaces.

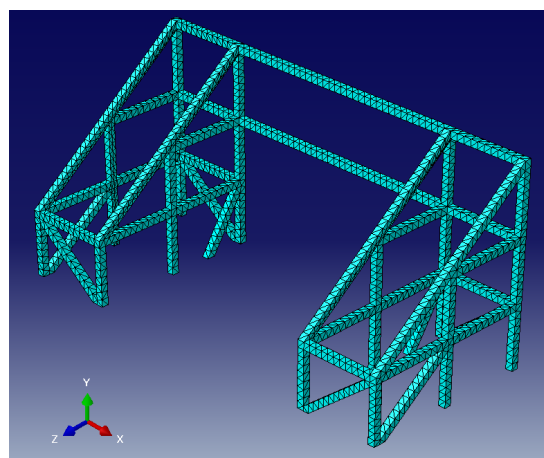
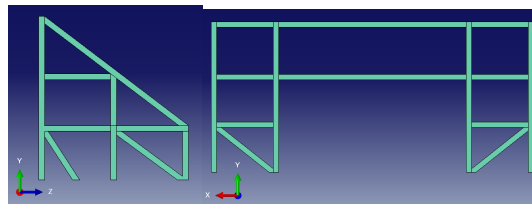


Figure 5.17: Truss shell mesh.

5.8 Jobs and Output

In each *FEM*, 7 Jobs were created in total. The first *Job-Frequency* holds the results of the frequency analysis. The other 6 Jobs hold the initial conditions and loads for each *Dynamic, Implicit* simulation, as referenced in the Load section of this report.

For each Step a *History and Field output* must be created with an increment of $n=1$, to effectively capture the output in each iteration.

5.8.1 Preparing the ABAQUS model for the co-simulation.

The preparation of the model was done in accordance with the requirements of *Star – CCM+*'s inputs. *Star – CCM* accepts either *Sheet* or *Solid bodies* as input geometry. Thus, in the **Assembly** module by selecting the facade surfaces, a *Boolean-Union* operation can be performed to create the initial closed shell surface that will be transformed into a solid part later on. Afterwards, in the same manner the *Rigid models* were created by merging the individual parts, the assembly was once again merged into a new part.

Now, in the **Part** module, the tool *Create: Solid from Shell* was used to transform the closed shell surfaces into solid. After such an operation, a geometry query should be run to highlight the free edges and problematic faces that have been created as well as the wire elements that might exist in the solid. Consequently the tool *Geometry Edit* can be used, more specifically the *Remove redundant entities*, *Remove wire* and *Remove Faces* operations. The Solid Part was scaled by 1000 units (*ABAQUS* basic unit is mm) and then exported in a *.stp* format.

The coupling process will occur between the input files and the External Links in *STAR – CCM+* and will not be influenced by the *3D* model.

5.8.2 Frequency analysis results

Rigid models, (Model 1,4)

$$f_1 = 0.52818Hz \quad f_2 = 0.87558Hz \quad f_3 = 1.1364Hz \quad (5.16)$$

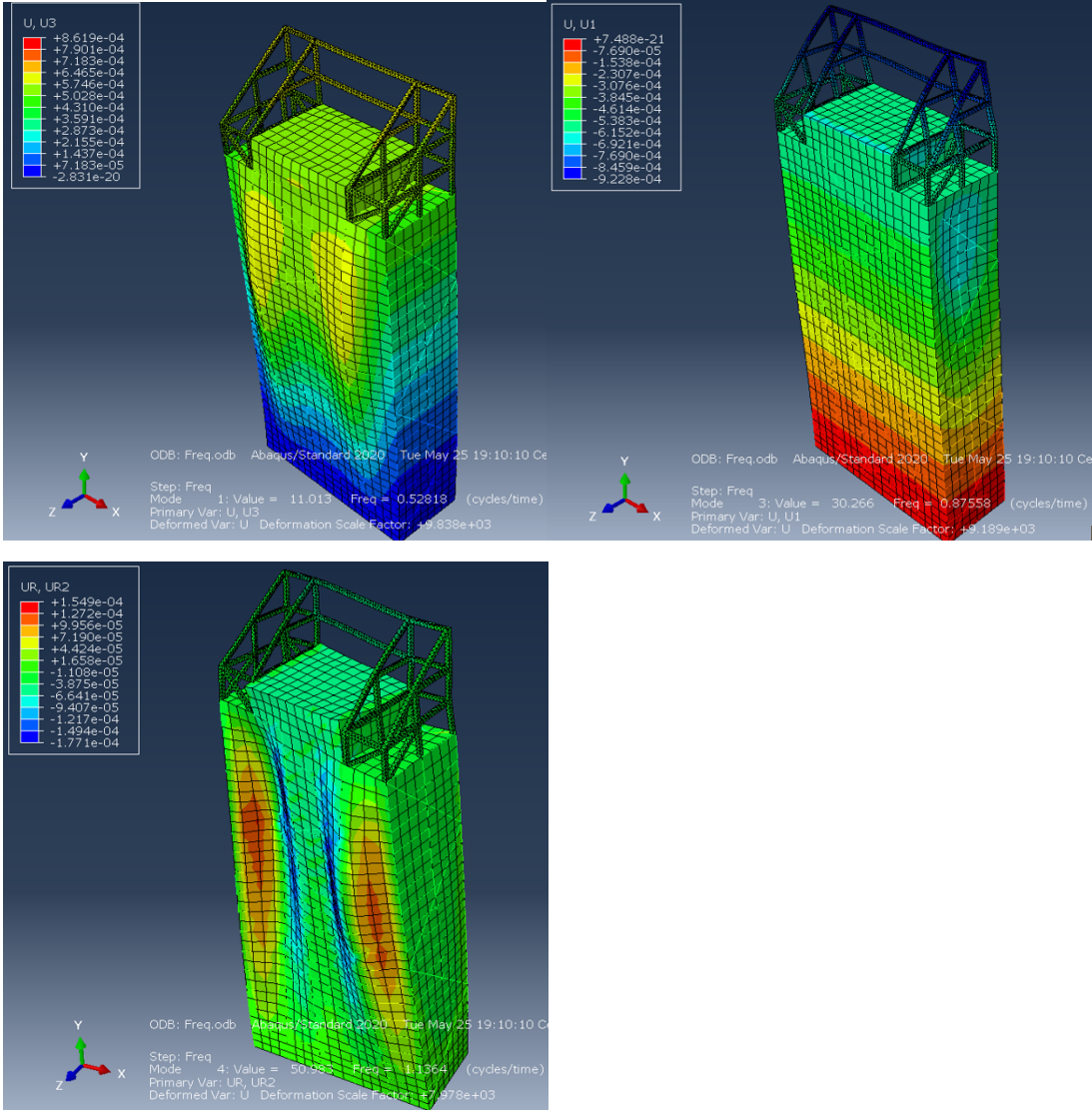


Figure 5.18: Fundamental eigenvalues of Model 1 and 4.

Semi-rigid model, (Model 2)

$$f_1 = 0.36534Hz \quad f_2 = 0.78858Hz \quad f_3 = 0.92529Hz \quad (5.17)$$

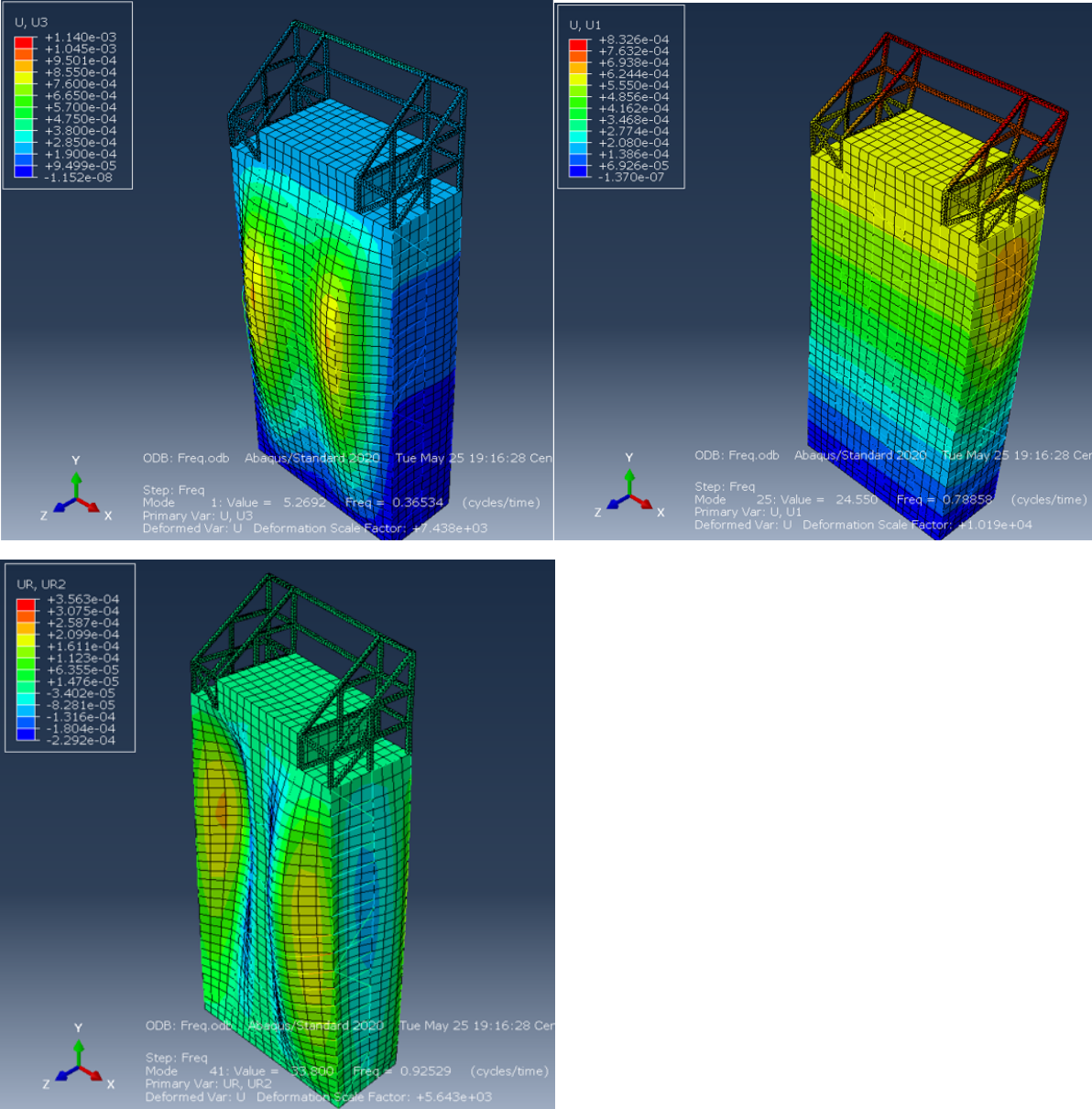


Figure 5.19: Fundamental eigenvalues of Model 2.

SSI model, (Model 3)

$$f_1 = 0.48634Hz \quad f_2 = 0.74788Hz \quad f_3 = 1.0391Hz \quad (5.18)$$

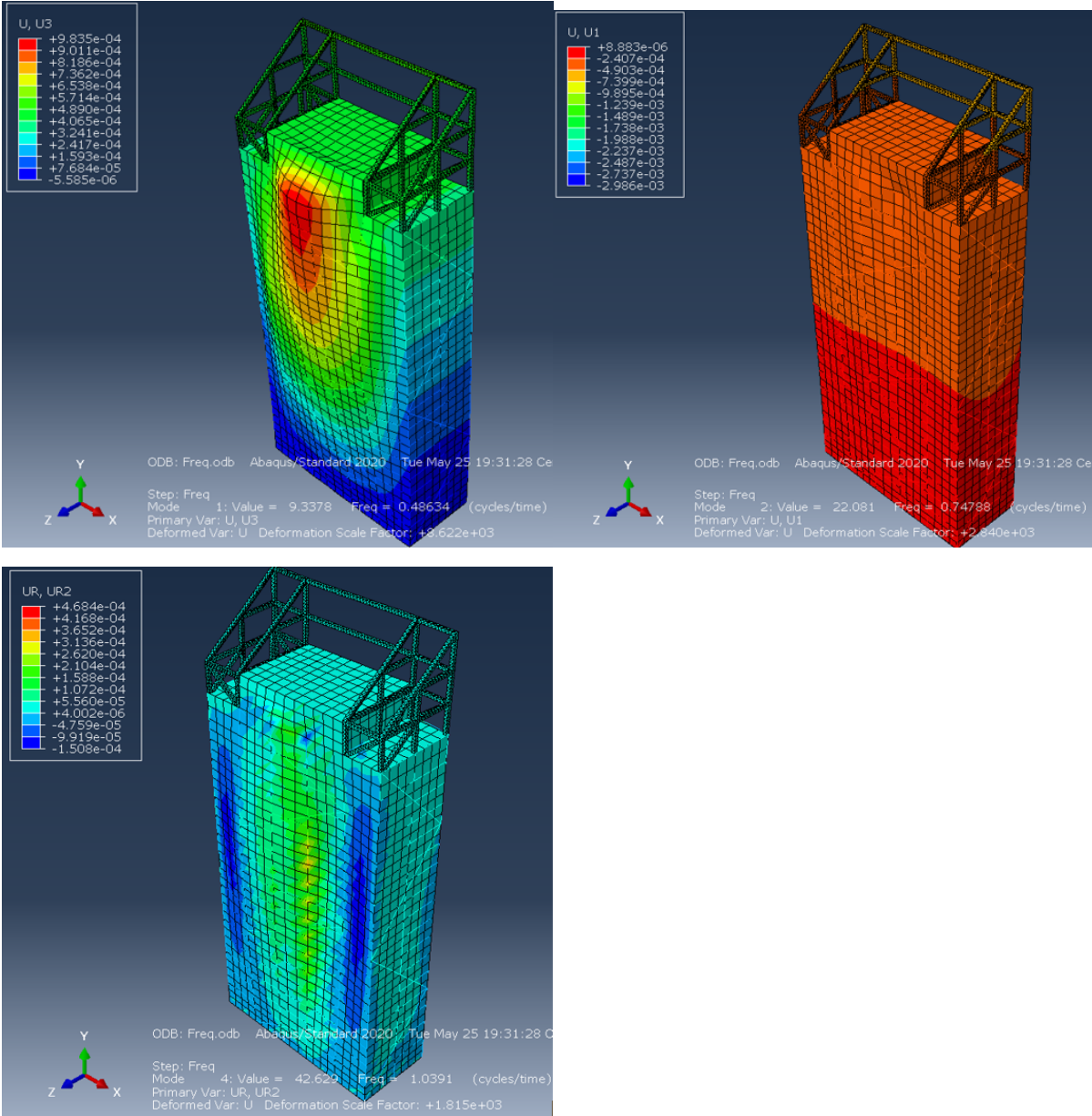


Figure 5.20: Fundamental eigenvalues of Model 3.

5.9 Comments and discussion on the FEM part

Based on the measured and designed eigenfrequencies of Mjøstårnet, as mentioned in 3.1, the fundamental eigenfrequencies ω_i of the created FEM in this study do not deviate from them significantly. Moreover, some conclusions are:

- Regarding the semi-rigid model, the designed frequency $f_{1,d} = 0.35Hz$ coincides with that of the replicated model. This can be attributed to the design connection stiffness applied by *EC5*, which ought to be relatively the same.
- The difference between the realistic fundamental frequency provided by ambient measurements, $f_{1,r} = 0.5Hz$ and the designed frequency $f_{1,d} = 0.35Hz$ can be attributed to the fact that *EC5* provides a simple yet universal way of calculating connection stiffness, without taking into account all the parameters that play a role in deciding that value. Additionally, it is a common practice between engineers to always pick the '*worst case scenario*' by applying the factor of safety in play. In this problem, a less stiff building gives worst results in a wind analysis.
- The difference of the second modelled fundamental eigenfrequency and that of ambient analysis', is perhaps the amount of columns in the back facade modelled, more specifically those of the elevator shaft, providing more stiffness.
- The third fundamental eigenfrequency of Model 2 is near the realistic one. In contrast, the rigidly connected models overestimate the torsional stiffness as it was expected, because timber connections in their nature are pinned and not welded.

Chapter 6

CFD Methodology

This segment will analyze and expand on the simulation and methodology of the wind tunnel domain of Mjøstårnet. The aeroelastic analysis was run on the commercial software *STAR – CCM+* by *Siemens*. The wind flow domain dimensions remained the same for each case run. Also in all scenarios the local coordinates are identical to the global coordinate system that is default to *Star – CCM+* (X, Y, Z) and *ABAQUS/CAE*. The $|X|$ coordinate indicates the width of the domain perpendicular to wind flow, the $|Y|$ coordinate indicates the height of the domain, whilst the $|Z|$ coordinate indicates the width of the wind in the along wind direction. The dimensions of the building in all scenarios remain the same.

6.1 Preparing the Geometry.

A *CFD* analysis near an obstacle follows a slightly different principle than *FEA*. In contrast to a *FEA*, it is not the obstacle that needs to be modelled, but rather the absence of fluid continuum in that area. As it becomes apparent, the first step would be to input the obstacle (building) geometry from *ABAQUS*. The export process has been explained in the previous segment 5.8.1.

After importing the *ABAQUS* file by selecting **3D-CAD Model**, the following procedures can be applied in the *Body* by selecting *Repair Tools*:

- *Optimize edges*, where unclosed or overlapping face edges are repaired
- *Remove redundant edges*, where identical edges and faces are merged
- *Repair Body*
- *Check Validity*, to check if all faces on the 3D CAD are valid. If they are not further surface preparation is required.

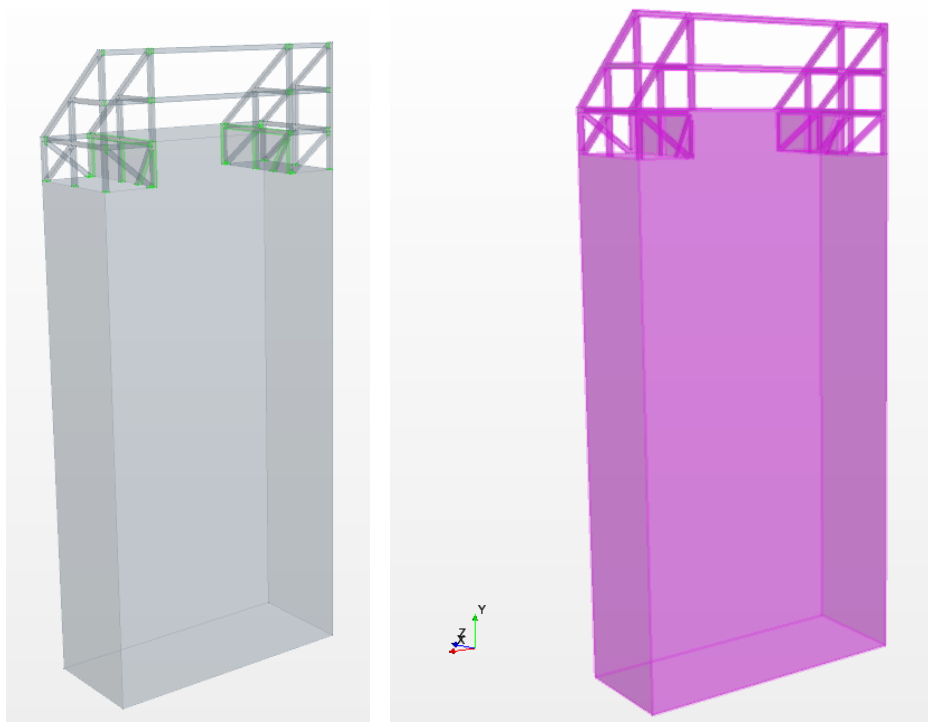


Figure 6.1: Imported solid geometry part|Right: Before geometry edit, Left: After geometry edit.

After the initial inspection of the 3D Geometry, it is possible to proceed with the creation of a *New Geometry Part* and eventually with the creation of the wind flow domain. The domain can be created in this module as a *Solid Primitive* or later on in the **Parts** module by creating a *New Shape Part*. It should be noted that for external wind flow simulations, it is recommended to use the latter option since it does not constrict the creation dimensions of the solid.

The initial dimensions of the wind domain can be calculated by selecting appropriate domain sizes so that air flow on its boundaries is not affected by buildings placed in it [65]. For an *ABL* simulation the correlation is:

- $5 * H_{max}$ for the upstream dimension
- $15 * H_{max}$ for the downstream dimension
- $5 * H_{max}$ for the domain height
- $5 * H_{max}$ for the crosswind dimension

For an $H_{max} = 84.8m$, which includes the truss on top of the building, the following dimensions were used initially according to the mentioned *ABL* study:

Type	Upstream	Downstream	Crosswind	Height
Length (m)	424	1272	424	424

The dimensions mentioned are quite controversial and also used in an *ABL* study, where more than 1 building exists. After some testing, the proper wind domain dimensions can be visualised by running a *SRANS* analysis and making sure:

1. the separation field has properly been developed in the crosswind and height dimensions
2. the wake field has converged and stabilised in the downstream
3. the separation field in the upstream is fully captured

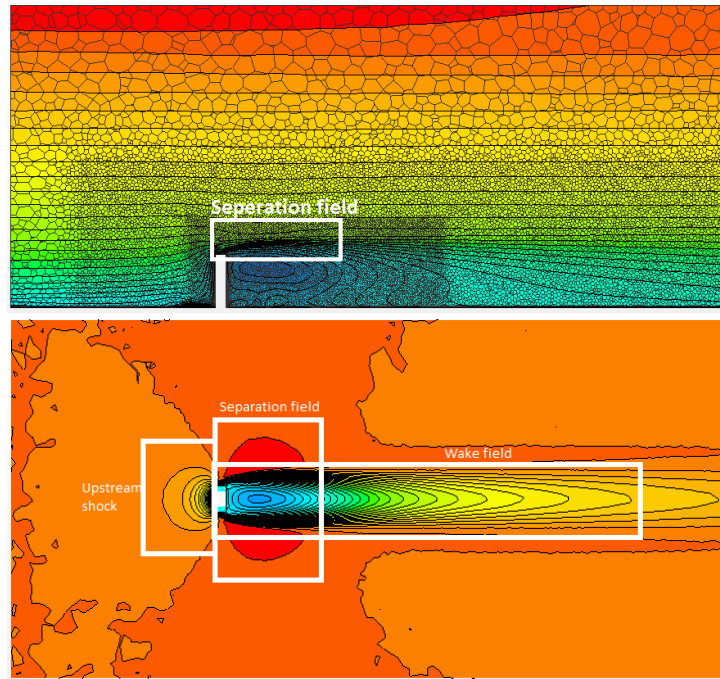


Figure 6.2: Preliminary *SRANS* domain testing. |Up: Separation field at the top of the building, Down: Wake field.

After some initial testing, the final values of the wind domain are visualised below. The building was also placed in the centre of the X direction, allowing adequate length for the lateral separation field to be developed. In the Y direction, the building was placed in the lowest end of the domain and in the Z direction the building was translated $Z_{trans} = -300m$, for the wake field to properly develop. In the following table the dimensions can be viewed in a more detailed fashion.

Coordinates	Building length (m)	Formulation	Initial domain dimension	Final domain dimension
X	35.9	$5*(84.8)$	424	560
Y	84.8	$5*(84.8)$	424	400
Z	15.3	$15*84.8+5*84.8$	1696	1200
X_{domain}		$(560-35.9)/2$		262.05
Y_{domain}		$400-84.8$		315.2
$Z_{domain}^{upstream}$		600-300		300
$Z_{domain}^{downstream}$		600+300		900

After successfully generating the wind domain, the next step is to create the assign the discrete surfaces which will be assigned a *BC* later. To do so, select surface of each part and proceed with the option *Split By Patches*. It is of vital importance, when creating the surfaces of the building to match them **identically** with the coupling surfaces from the *Dynamic, Implicit* step in *ABAQUS*. Refusing to do so will result in mapping faces and vertices errors in the *FSI* step.

In regard to the building's surfaces, namely facade and the truss shell they were split further due to the difference in their surface dimensions. For each part the following surfaces were created:

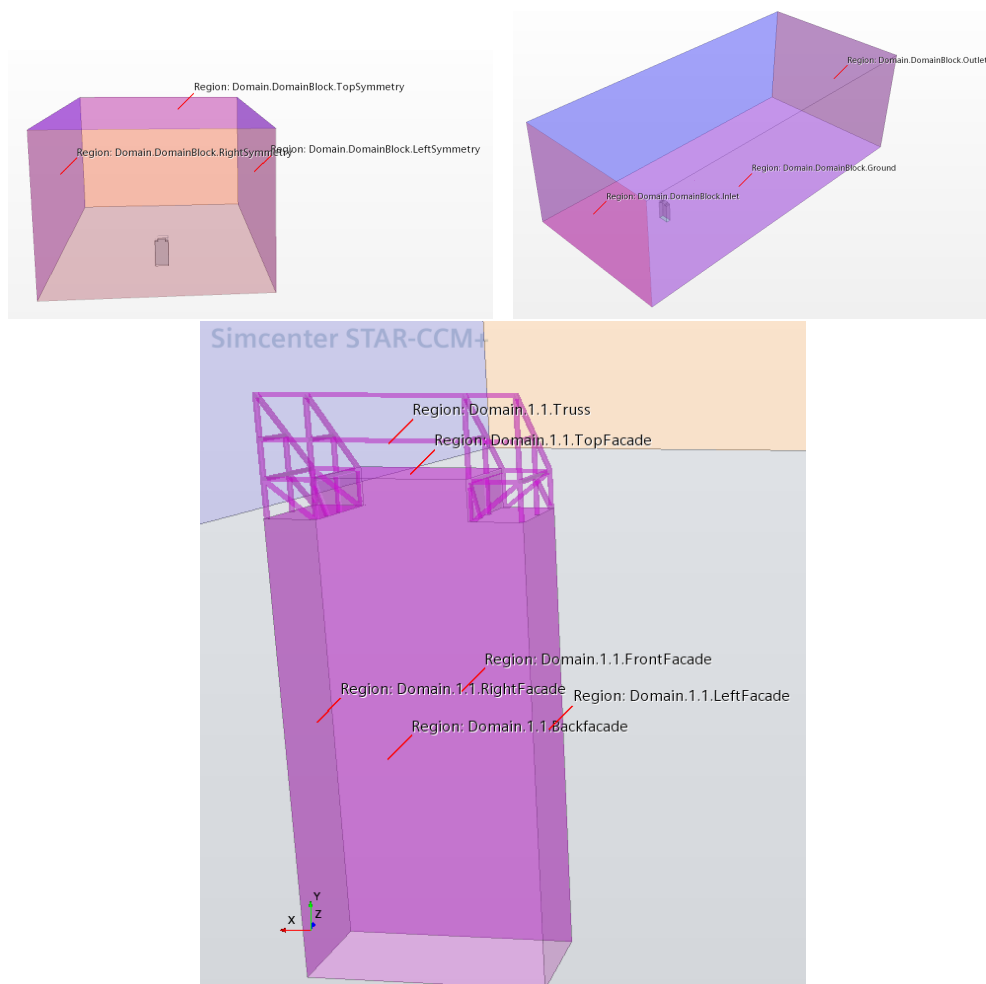


Figure 6.3: Split surfaces of the wind domain.

In the meantime, to create the final domain, the final step of subtracting the *3DCAD* model from the domain Block must be made. To do so, both parts were selected to undergo the *Imprint* operation before the *Subtract* one, under the *Boolean* tree in **Part Operations**. It is important to choose while *Subtracting* the **Resulting Mesh Type** as *Conformal*, as this will enhance the quality of the surface meshing afterwards (this does not apply when using a Polyhedral Mesher, but it is a good practice nonetheless). Select as Input parts both the 3D CAD and the Domain Block and only the Domain Block as target part. By executing the operation, a new part will be created which will serve as the **Region** for the *CFD* analysis. By creating these operations, any alteration that needs to be done in the *3D* or the Domain will be automatically generated in the resulting part without any need for creating a blank slate file.

6.2 Creating the Region.

6.2.1 Assigning boundary conditions to surfaces.

Selecting the *Subtracted* Domain part and applying the option *Assign Parts to Regions* will result in the creation of the region.

In the **Region** tree, BC can be set to the corresponding surfaces. The *Physics* continuum will be solved in this region. Note to select the option *Create a Boundary for Each Part Surface*, elsewise the surface splitting done above won't transfer properly. The created surfaces can be seen in 6.3, and their respective boundary conditions can be reviewed in the following table:

Part	Name	Boundary Condition
Domain	Inlet	Velocity Inlet
Domain	Outlet	Pressure Outlet
Domain	LeftSymmetry, RightSymmetry, TopSymmetry	Symmetry Plane
Domain	Ground	Wall
Building	FrontFacade,BackFacade, RightFacade,LeftFacade, TopFacade, Truss	Wall

The physics conditions for each boundary will be explained in segment 6.5.

6.3 Meshing.

Parts Based Mesher will be used. *PBM* detaches the meshing from the physics and provides a flexible and repeatable meshing pipeline. This strategy provides several advantages over region-based meshing [66]. This can be enabled by applying an *Automated Mesh* operation in the *Parts* tree and selecting “**Per Parts Meshing**” in the *Properties* menu. The meshing models that were used were:

- Surface Remesher
- Trimmed Cell mesher
- Automatic Surface Repair
- Prism Layer Mesher, which will be used to properly capture near wall boundary layers.

Trimmed Cell Mesher

The reason **Trimmed Cell** mesher was chosen over the *Polyhedral*, was due to computational limitations. The polyhedral cells that are created typically have an average of 14 cell faces. In contrast, trimmed cells have only 4. An additional feature that is useful in modelling external aerodynamic flows is the ability to refine cells in a wake region. This region is generally the volume of fluid at the rear of a moving body.

In general, the memory requirements for meshing are:

- Trimmed mesh: About 0.5 GB / million cells.
- Polyhedral mesh: About 1GB / million cells.

The downfall of the trimmed cell mesher, is that near surfaces the cells collapse from polyhedral to tetrahedral or hexahedral. What this means is that when a *Volumetric Control* is applied on a trimmed cell mesh, the abrupt change in cell size will cause the *Cell Quality* to drop near that surface area. However, this can be combated to a certain

degree by enabling the *Run Post Mesh Optimizer* setting.

Surface Remesher

The **Surface Remesher** can be used to retriangulate the surface. This option improves the overall quality of an existing surface mesh and optimises it for the volume meshing and it also aids the subsurface generator when the prism mesher option is selected.

The quality of an overall mesh is first and foremost dependent on the surface meshing performed. Therefore, it is vital to select the following options in the Surface Remesher dialog:

- Meshing Method as *Enhanced Quality Triangle*
- Select *Perform Curvature, Proximity & Compatibility Refinement*
- Set the *Minimum Face Quality* as low as possible. A recommended value is 0.02.

This value can be set in the *Automatic Surface Repair* as well.

Prism Layer Mesher

Regarding the **Prism layer mesher**, it is required to resolve efficiently the wall boundary layers and improve the accuracy of the flow solution [67].

Prism layers allow the solver to resolve near wall flow accurately, which is critical in determining not only the forces on the wall, but also wind flow features such as separation, which in turn affects integral results such as drag, lift or pressure drop. Accurate prediction of these flow features depends on resolving the velocity and temperature gradients normal to the wall. These gradients are much steeper in the viscous sublayer of a turbulent boundary layer than would be implied by taking gradients from a coarse mesh. Prism layer meshing resolves the viscous sublayer directly (*low $y^+ < 1$*) and for coarser meshes it allows the code to fit a wall function more accurately (*high $y^+ > 30$*).

The quality of the Prism layer can be viewed in a Geometry scene, by making sure the layers created capture the surface of the geometry effectively. Also a scalar scene can be created to view prism layers.

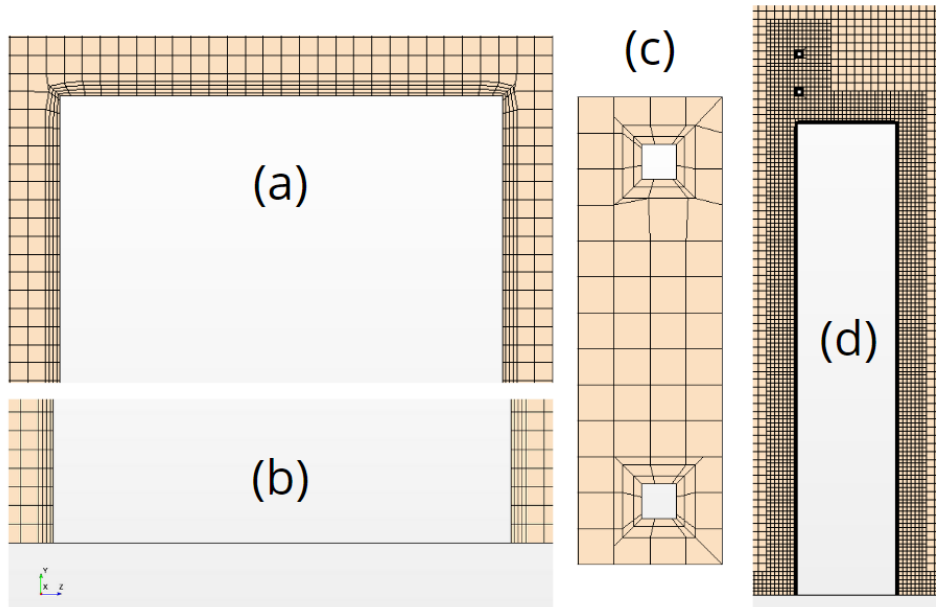


Figure 6.4: Details of the prism layer| (a) Prism layer on top of the building, (b) Prism layer near the ground, (c) Prism layer around the Truss elements, (d) Overall prism layer

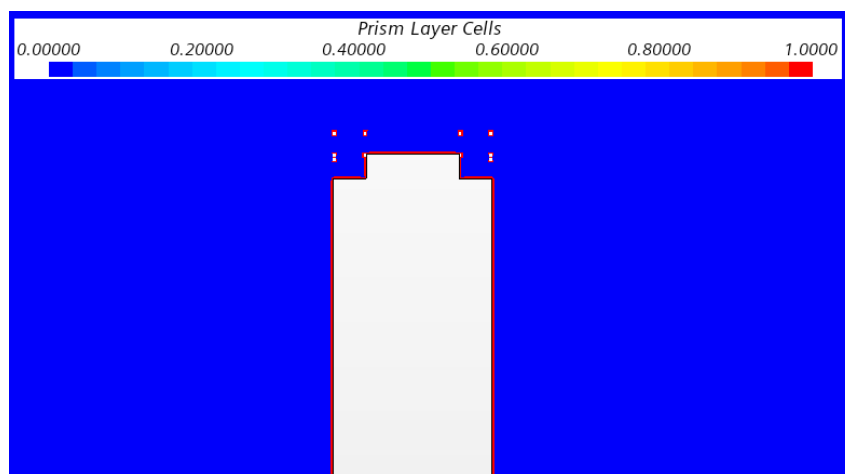


Figure 6.5: Prism layer quality scalar

If a prism cell layer setup is not used, the gradients can alternatively be solved by using a manually calculated VC . However, depending on the Reynold's number, a turbulent shear layer requires an excess of 10-20 cells in the cross-stream direction for accurate resolution of the turbulence flow profiles. To resolve the viscous sublayer, a few prism layers can yield acceptable results, while several VC s must be setup. That can be attributed not only in the increased near wall mesh density a prism layer provides, but also since high-aspect-ratio cells are to be used, they offer better cross-stream resolution without incurring an excessive stream-wise resolution.

Prism layers also reduce numerical diffusion near the wall. Numerical diffusion is a discretization error that smears discontinuities and steep gradients in a finite volume advection scheme. Numerical diffusion is minimised when the flow is aligned with the mesh. The use of prism layers greatly enhances accuracy as a result [67]. The calculations for the first cell height in prism layer is always done manually and the calculation will be expanded upon at the Appendix D.

It should be noted that modelling the Prism Layer correctly is quite tricky, especially for complex geometries with gaps and corners, such as Mjøstårnet. There exists no definitive answer on how to properly model the prism cells. The author of this work would suggest finding the optimal mesh resolution through trial and error by replicating the following *preprocessing* process in the segment 6.3.2. In this work, the following parameters were set in the *Prism Layer Mesher* dialog:

1. The Stretching Function can be set as *Hyperbolic Tangent*. This will allow a smoother transition in the prism cell layers.
2. Select *Thickness Ratio* as the distribution method. The value of this ratio will depend on the target wall $y+$ value and the number of prism layers.
3. Set the *Minimum Thickness Percentage* as low as appropriately possible. If the viscous sublayer is to be resolved (*low $y+$* 1), one can expect minuscule first layer

thickness. In that case, if the minimum thickness is not set low, the first layer will be retracted.

4. *Boundary March Angle*, *Concave Angle Limit*, *Convex Angle Limit* and *Near Core Layer Aspect Ratio* are all options that guide the prism layer mesher to capture optimally the irregularities of the geometry. In this work only sharp corners exist in the geometry, thus only the *Convex Angle Limit* is to be evaluated. The angle between rectangular edges is 270° . Always set *Near Core Layer Aspect Ratio* to 1, to improve prism cell quality.

6.3.1 Default meshing values.

Property	Value
Base size	10m
Target surface size	10m
Minimum surface size	5m
Surface growth rate	1.2m
Number of prism layers	8
Prism layer thickness ratio	1.9
Prism layer thickness	0.5m
Number of growth rate cells	8
Custom surface growth rate	6
Maximum Cell size	10m
Post Mesh Optimisation	<i>Enabled</i>

6.3.2 Surface and Volumetric controls

Solving the wall boundaries and the wake field requires a finer meshing in certain areas in the wind domain [68].

The wall surface refinement can be done by implementing *SCs* on the building as a finite element refinement approach, whilst *VCs* can be applied in the wind domain by a finite volume refinement approach. To apply a *Surface Control*, the following part surfaces were selected. This will be done to fine tune the Prism layer and apply custom surface values on smaller surfaces.

Surface Control 1

Part Surface	Prism layer	Target surface size	Minimum surface size
Domain.Ground	Disabled	10m	2m

Surface Control 2

Part Surface	Target surface size	Minimum surface size
Domain.BackFacade,Domain.FrontFacade, Domain.RightFacade,Domain.LeftFacade	0.5m	0.5m

Surface Control 3

Part Surface	Number of Prism layers	Target surface size	Minimum surface size
Domain.Truss	4	0.6m	0.5m

Postprocessing evaluation of surface mesh

The resulted mesh consists of 2543610 cells, 7651706 faces and 2649677 vertices. The completed mesh can be evaluated from two main standpoints. Firstly, one must make sure that the Mesh Diagnostics are giving a value in the expected regions and that no Bad Cells were created. Secondly, using Scalar Scenes one should plot Mesh Metrics and make sure the image being given is expected.

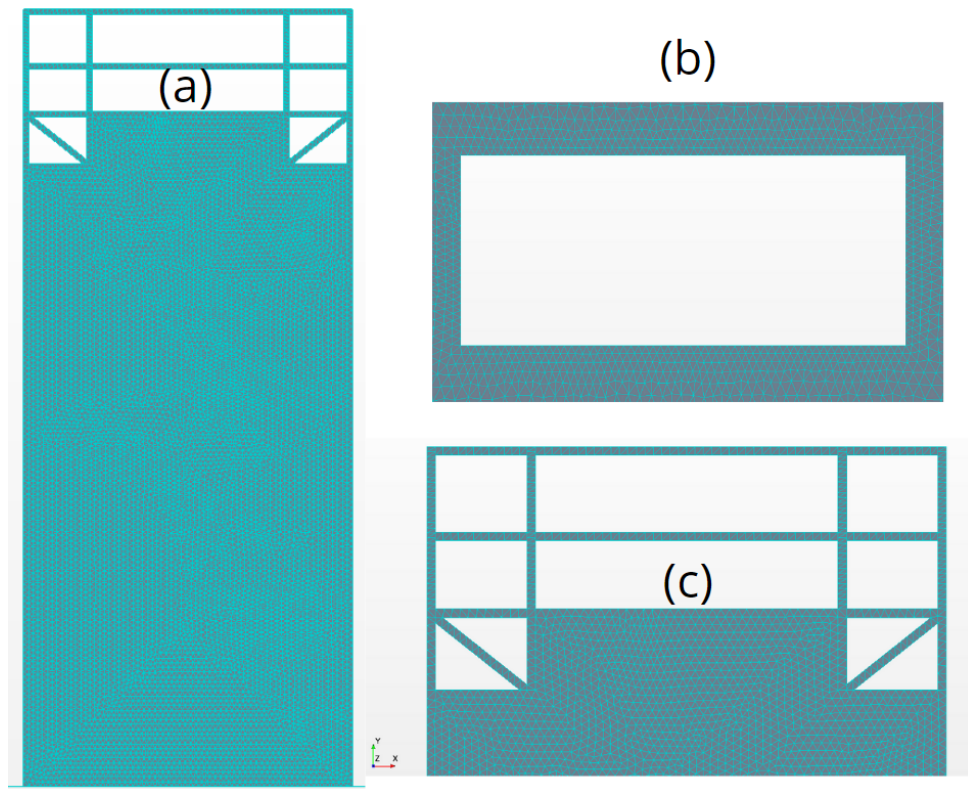


Figure 6.6: Details of the surface mesh| (a) Surface mesh on the building, (b) Transitional ground-building surface mesh, (c) Surface mesh on truss

Furthermore, the full *Mesh Diagnostic Tool* should be run. The quality of the surface mesh is linked by the *Face Validity* and the *Tri quality*.

```

1 -> MESH VALIDITY:
2   Mesh is topologically valid and has no negative volume cells.
3 Face validity:
4 #Minimum Face Validity: 1.0000000000e+00
5 #Maximum Face Validity: 1.0000000000e+00
6 #1.00 <= Face Validity           2543610   100.000%
7 Tri Quality      Faces      Percent
8 # < 0.7         73         0.1
9 # < 0.8         861        0.6
10 # < 0.9        6714        4.9
11 # < 1.0       137316       100.0
12 Worst quality is 0.00947
13 final number of faces: 137316

```

Setting up Volumetric Controls

To apply a *Volume Control*, the following part shapes must be created, as they can be seen in 6.7. This will be done in the **Parts** tree.

- VC_1 , which aims to limit the cell size to 2m.
- VC_2 , which aims to limit the cell size to 4m.
- VC_3 , which aims to limit the cell size to 8m.

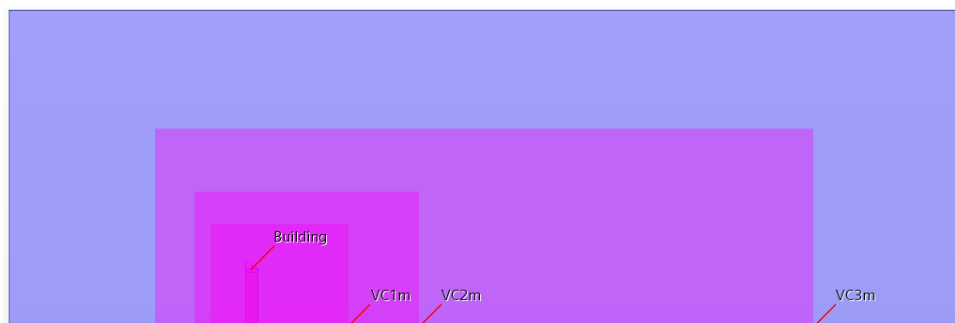


Figure 6.7: Volumetric Controls.

Evaluating the Volume Mesh

The *FVM* mesh can be evaluated by seven (7) standpoints [66]:

- (a) *Cell Warpage Quality*, which identifies thin and warped cells. These types of cells can cause issues for the flow solver, especially for high fidelity simulations. Cells with a cell warpage quality lower than 0.15 are bad cells.
- (b) *Least Squares Quality*, which value is based on the ratio of the maximum and minimum eigenvalue ratios of the symmetrical vector matrix. Cells with a least squares quality less than $1.0E - 3$ are considered bad.
- (c) *Volume Change*, a large jump in volume from one cell to another can cause potential inaccuracies and instability in the solvers. Cells with a volume change of 0.01 or lower are considered bad cells.

- (d) *Skewness Angle*, is the angle between the face area vector (face normal) and the vector connecting the two cell centroids. Cells often have the same skewness angle corresponding to the face that they share. To reduce the impact on robustness, skewness angles greater than 85° must be avoided.
- (e) *Cell Quality*, flat cells with highly non-orthogonal faces have a low cell quality. The cell quality is expected to be low in the near prism layer cells. A degenerate cell has a cell quality approaching zero. Cells with a face quality less than $1.0E - 5$ are considered bad.
- (f) *Chevron Quality Indicator*, are pairs of thin slender cells which meet at a common face at an angle such that the line joining the cell centres does not pass through the common face. Chevron cells are marked by the value of 1.0 and must be removed.
- (g) *Bad Cells*, if areas are identified as bad cells should be removed and the region remeshed.

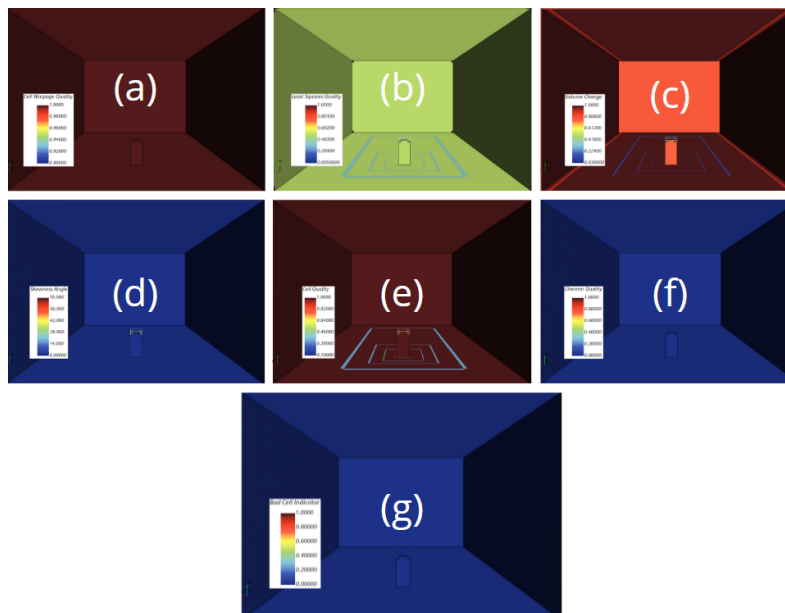


Figure 6.8: Mesh quality scalars|Small irregularities occur in the expected regions.

Furthermore, the full *Mesh Diagnostic Tool* should be run. The quality of the surface mesh is linked by the *Face Validity* and the *Tri quality*.

```

1 Volume Change :
2 Minimum Volume Change: 2.101071e-02
3 Maximum Volume Change: 1.000000e+00
4
5 #1.000000e-03 <= Volume Change < 1.000000e-02          0      0.000%
6 #1.000000e-02 <= Volume Change < 1.000000e-01        5139    0.202%
7 #1.000000e-01 <= Volume Change <= 1.000000e+00      2538471 99.798%
8 Maximum boundary skewness angle in region = 6.457827e+01 deg

```

Another important part of evaluating the volume mesh is to see clear identification between the Prism Layer Topography and the Geometry. This is done by viewing a Planar mesh scene that cuts through the geometry part and making sure the prismatic layers follows the geometry without intersecting it. The prism layer details can be seen in Figure 7.1. Thus, it becomes clear that the Prism layer does not intersect with the Geometry. The result is that during the *Morphing* step in the *FSI*, no unclosed or negative volume cells will be created.

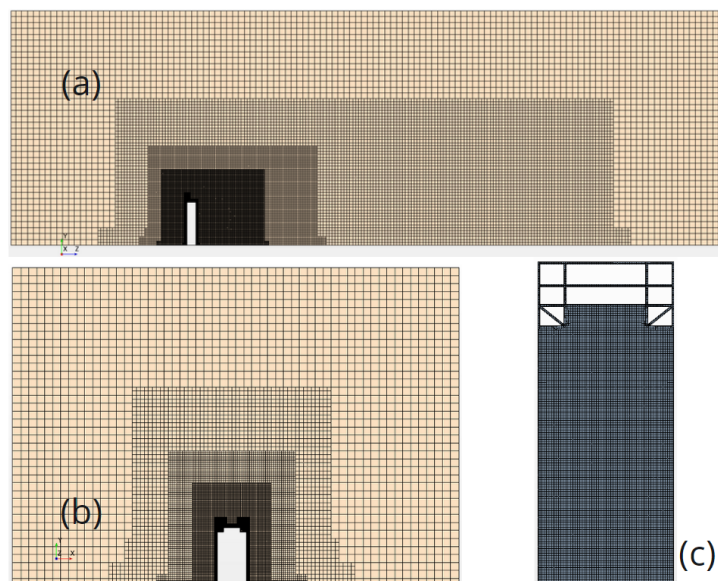


Figure 6.9: Volume mesh. |(a) Mesh perpendicular to the wind flow, (b) Mesh lateral to the wind flow, (c) Building surface mesh.

6.4 Creating Physics continua

Running the *FSI* co-simulation with *ABAQUS* required that both *FEM* and *CFD* analysis have already converged separately. Hence, it is considered good practice to run a standalone *CFD* simulation until the wind flow field has been resolved.

As mentioned previously in the theory segment 4.2, the standard *SST(Menter) $k - \omega$* (*SSTKO*) turbulence model can be used to solve the eddies in the wake field. In this study fixed turbulent inlet conditions will be met and their calculations can be seen in Appendix D based on the Wilcox (1988) $k - \omega$ turbulence model [69]. More refinement can be done by applying the revisited $k - \omega$ model [70], or by applying height dependent turbulent models [71].

For the initial solution, both *SRANS* and *URANS* can be used. However, in the case of simulating an *ABL* by introducing implicit surface roughness on the ground level, most academic work so far focuses on applying the other two-equation turbulence model $k - \epsilon$ in *SRANS* implementation [72], [73]. In the same manner, for an *ABL* setup in urban pollutant problems *LES* or *DES* is preferred [74].

In this thesis, *SRANS* was first implemented to check the validity of the computational domain, see Figure 6.2, because it is based on time-averaging of *Navier - Stokes* equation and provides a steady and stable description of the turbulence model. Afterwards, the *URANS* as an assemble-averaging the *Navier - Stokes* equation for repeatable transient solution was used to create the initial solution.

This approach was followed because:

1. *URANS* converged faster to an initial solution when provided with a relative high time step,
2. and the dynamic implicit co-simulation setup is by definition a time variable problem.

6.4.1 Numerical *URANS* model

For the uncoupled convergence run, under the **Continua** tree, a new *Physics Continuum* was selected with the following models enabled:

- *Space*, Three Dimensional
- *Material*, Gas, Constant Density
- *Flow*, Segregated Flow, Implicit Unsteady, Turbulent, Segregated Fluid Isothermal
- *Turbulence*, RANS, K-Omega, SST (Menter) K-Omega, Gradients, Wall Distance, All Wall Y+, Turbulence suppression
- Cell Quality Remediation, Solution Interpolation.

The semantics of each model are not the subject of this Thesis and as such only a few comments will be made.

Segragated Flow was chosen instead of *Coupled Flow* due to computational restrictions. *Segregated Fluid Isothermal* was chosen to introduce the temperature factor in the turbulence equations. This was done to validate the dynamic viscosity of air and later on Reynolds' number.

SSTKO

All Wall Y+ was chosen so the both high and low y+ values can be solved. *Cell Quality Remediation* and *Solution Interpolation* were chosen to establish better convergence in the coarse mesh.

$$\text{Kinematic Eddy Viscosity } : \nu_t = \frac{\alpha_1 * k}{\max \alpha_1 * \omega, S * F_2}, \quad (6.1)$$

$$\text{Turbulence Kinetic Energy } : \frac{\partial k}{\partial t} + U_j * \frac{\partial k}{\partial x_j} = P_k - \beta * \omega + \frac{\partial}{\partial x_j} * \left[(\nu + \sigma_k * \nu_t) \frac{\partial k}{\partial x_j} \right] \quad (6.2)$$

Specific Dissipation Rate :

$$\frac{\partial \omega}{\partial t} + U_j * \frac{\partial k}{\partial x_j} = \alpha * S^2 - \beta * \omega^2 + \frac{\partial}{\partial x_j} * \left[(\nu + \sigma_\omega * \nu_t) \frac{\partial \omega}{\partial x_j} \right] + 2 * (1 - F_1) * \sigma_{\omega 2} * \frac{1}{\omega} * \frac{\partial k}{\partial x_i} * \frac{\partial \omega}{\partial x_i} \quad (6.3)$$

The standard *SSKTO* coefficients will be applied in this simulation,

Coefficient	Value
α_1	0.31
σ_{k1}	0.85
σ_{k2}	1
$\sigma_{\omega 1}$	0.5
$\sigma_{\omega 2}$	0.856
β^*	0.09
β_1	0.075
β_2	0.0828

6.5 Boundary Conditions

6.5.1 Upstream Boundary

Inflow equation

In wind energy studies, two mathematical models or 'laws' have generally been used to model the vertical profile of wind speed over regions of homogeneous, flat terrain. The first approach, the *log law*, has its origins in boundary layer flow in fluid mechanics and in atmospheric research. It is based on a combination of theoretical and empirical research. The second approach is the *power law*. Both approaches are subject to uncertainty caused by the variable, complex nature of turbulent flows [75].

In this study, the incident wind is modelled using a boundary layer profile for smooth flows given according to the power law equation and the BC is set as **Velocity Inlet**.

**Boundary layer
profile:**

$$V_1 = V_0(Z/\delta)^n$$



$$\text{Power law : } V_1 = V_o * \frac{Z^n}{H_{building}} \quad (6.4)$$

For this study, the reference height equals to the height of the main part of the building $H_{building} = 68m$. The reference velocity at that height will equal to an incremental fraction of the critical velocity and will be discussed below Typical values of the wind shear exponent normally range from 0.1 – 0.25 depending on the terrain [76].

However, in this case the wind shear exponent, n , was chosen identical to the first eigenfrequency of the building, $n = 0.5$. This change is based on the numerous experimental studies which show that the damping in various solid materials increases with frequency over a finite bandwidth, and the increase is weak if the damping is low [77]. Further studying should be implemented to navigate a correlation between the power law exponent and the oscillation period in aeroelastic analyses. The aeroelastic oscillations in this study show perfect alignment with the factual period of 2(s).

Critical wind speed, V_{cr} is defined as the speed in which the vortex shedding phenomenon occurs.

$$V_{cr} = \frac{f_n * D}{St} \quad (6.5)$$

where St is the Strouhal number, a dimensionless number describing oscillating flow mechanisms. In this work $St = 0.08$ was adapted from another aeroelastic study [78] due to lack of data for the specified geometry. A sensitivity analysis should be done by testing St numbers 0.1 – 0.2, which correspond to the proposed Strouhal numbers for rectangular buildings. Vortex shedding is defined when a wind blows alongside of a structure and

vortexes are shed alternately from one side to the other. This results in alternating low-pressure zones to be generated on the downstream giving rise to a fluctuating force acting at crosswise to the wind direction [79]. Usually the across-wind response of tall slender structures is a result of the asymmetry in the wake flow, although aeroelastic instability may occur when the natural frequency of the structure in the transverse direction is near to the vortex shedding frequency of the flow field around the building, leading to greater oscillations in the across-flow direction. At this point the mechanical frequency of the building controls the vortex shedding process. This phenomenon is known as *lock-in*. In this work, the goal is to identify the aeroelastic damping of high-rise timber buildings, thus the investigation of the *lock-in* phenomenon is not studied. Furthermore, the critical velocity for the across-wind oscillations for $f_2 = 0.87Hz$ and $St = 0.08$ is nearing the speed of sound, in which Mach number will exceed the subsonic barrier and the SST K-omega turbulence model becomes inaccurate [80].

The power-law equation for wind flow was implemented in Star-CCM+ by creating the following scalar field function.

```

1 {{{Position}[1] >=0 && {{{Position}[1] <68 ?
2 V_{h}*pow(({{{Position}[1]/68),0.5) :
3 ({{{Position}[1] >= 17.95 && {{{Position}[1] <=400 ? V_{h} :V_{h} )

```

By solving equation 6.5 and then dividing the V_{cr} by fractions of 2, the test speeds were derived as follows:

$$V_{cr} = \frac{f_n * D}{St} = \frac{0.5 * 35.9}{0.08} = 224.375m/s$$

V_{cr} fraction	$V_{cr}/nW = 1$	$V_{cr}/nW = 2$	$V_{cr}/nW = 3$	$V_{cr}/nW = 4$	$V_{cr}/nW = 10$	$V_{cr}/nW = 12.5$
Value (m/s)	17.95	35.9	53.85	71.8	179.5	224.375

Turbulence Inlet Conditions

In order to specify the turbulent conditions in the wind domain, the first step was to estimate Reynolds' number.

$$Re = \frac{\rho * U * L}{\mu} = 41134193 \quad (6.6)$$

Where the constant temperature defined in *Segragated Fluid Isothermal* under the *Physics Model* tree at 25° and,

- ρ is the density of the air at 25°, as 1.18415 kg/m³
- U is the reference velocity, V_h
- L is the characteristic length, here chosen as the width of the building $D = 35.9m$
- μ is the dynamic viscosity in regards to the reference velocity V_{h1} , μ_h

The flow can be characterised as highly turbulent, which is to be expected in an external wind flow. In this study, the Reynolds number was kept the same in all wind speed scenarios and only the dynamic viscosity μ was changed in accordance with the corresponding reference velocity U . This was done purely for convenience, since that the mesh (first cell height) will not need to be further refined for higher wind speeds. For more information about the first cell height see 6.3.

Reference Velocity, V_h (m/s)	Reynolds' number (-)	Dynamic Viscosity, μ (Ns/m ²)
17.95	4113493	1.85508E-5
35.9	4113493	3.71015996E-5
53.85	4113493	5.56523995E-5
71.8	4113493	7.42031999E-5
179.5	4113493	0.000185550799
224.375	4113493	0.00023188499

For low speed, or subsonic conditions, the Mach number is less than one, $M < 1$ the change in air density is very small. For the low subsonic conditions, compressibility of the fluid can be ignored. For the last speed scenario, $Vh_6 = 224.375m/s$, Mach number equals to $M = 0.653061$, meaning it is within the **subsonic speed limit** [81].

Next for the turbulence intensity I_v the length scale (l) of the turbulence at the inlet needs to be defined.

For an internal pipe flow, this is usually $\sim 10\%$ of the pipe's diameter. For external flows the length scale is likely to be significantly different and an appropriate value should be choosing carefully, depending on the ambient conditions. In this work a *Python* script was used [82] to approximate the turbulent intensity.

The script was based on internal flows, thus for the pipe radius, the half size of the wind domain was used and for the surface roughness the value $z_0 = 0.10$ was used in accordance to the ground's roughness. Thus the following value was used as turbulence intensity:

$$I_v = 4.190902\% \quad (6.7)$$

Based on the above turbulent intensity and the reference velocities Vh , the turbulent kinetic energy k can be calculated for each scenario.

$$k = \frac{3}{2} * Vh^2 * I_v^2 \quad (6.8)$$

The turbulent dissipation rate (ϵ) and the specific dissipation rate (ω) can be calculated next, where $C_\mu = 0.09$ as the turbulent model coefficient and $L = 35.9m$ as the reference length.

$$\epsilon = C_\mu * \frac{k^{3/2}}{L} \quad (6.9)$$

$$\omega = \frac{\epsilon}{C_\mu * k} \quad (6.10)$$

The turbulent kinetic energy k , the turbulent dissipation rate (ϵ) and the specific dissipation rate (ω) for each wind speed scenario can be visualised below. The extensive calculations for each wind speed case can be reviewed in Appendix D.

Reference Velocity, V_h (m/s)	TKE k	ϵ	ω
Vh_1	0.849	0.00196	0.0257
Vh_2	3.4	0.0157	0.0513
Vh_3	7.64	0.0529	0.077
Vh_4	13.6	0.125	0.103
Vh_5	84.9	1.96	0.257
Vh_6	133	3.83	0.321

6.5.2 Wall treatment for the ground surface

The inner turbulent boundary layer can be divided into three sublayers, i.e. *viscous sub-layer* next to the wall which is dominated by viscous effect, *log layer* next to the outer boundary layer which is dominated equally by viscous and turbulent effects, and *buffer layer* in-between.

The ground in the wind flow domain is set as a *Wall Boundary* with *No-Slip* conditions to emulate the zero velocity gradient of the fluid at the wall surface. The terrain roughness was modelled implicitly by applying the actual terrain roughness y_o corresponding to a roughly open landscape [83].

Hence the value chosen for the actual terrain roughness is, $z_o = 0.10m$.

For all turbulence models the roughness modelling approach is not physically meaningful if the roughness height is larger than the height of the wall-adjacent cell ($R+ > y+$). It is hence critical to model the first cell layer thickness correctly to the desired sublayer with $y+30$ for external aerodynamics. To implement the terrain roughness in *STAR-CCM+*, the integrated roughness height equation will be used, where $E = 9$ and $C = 0.253$ are

the built-in wall coefficients [66].

$$r = \frac{E * y_o}{C} = 3.56m \quad (6.11)$$

To properly capture the *ABL*, the mesh should be coarse enough near wall boundaries so that $y \gg y_0$, where y is the distance of the first cell centroid from the wall boundary [71].

6.5.3 Downstream boundary

The downstream *BC* is set as **Pressure Outlet**. Another valid option would be to set the *BC* as **Outlet** since the flow is incompressible.

The pressure outlet boundary is an outflow condition which imposes the working pressure. This boundary pressure can be considered as the static pressure of the environment into which the fluid enters. By applying the working *Pressure* as zero it is ensured that the absolute pressure equals to the domain pressure in the outlet. **Turbulent kinetic energy k and the specific dissipation rate ω must be set as zero to prevent reversed flow in the outlet boundary.** The boundary face velocity at the pressure outlet surface equals to $v = v_{ext}$, where the superscript *ext* indicates that the value is extrapolated from the adjacent cell.

6.5.4 Symmetry planes

A symmetry plane boundary condition allows the reduction and the extension of the computational domain in locations where the geometry and the flow are symmetric.

It is vital for the separation and wake field to be developed fully before to ensure that the solution that is obtained with a symmetry plane boundary is identical to the solution that would be obtained by mirroring the mesh about the symmetry plane. **In a symmetry plane, the normal velocity and the normal gradient of all other variables are zero.** Consequently, there is zero flux across the symmetry plane boundary.

The superscript *ext* indicates that the value is extrapolated from the adjacent cell and $n = a/a$ with a being the outward pointing face area vector.

$$v = v^{ext} - (v^{ext} \bullet n) \bullet n$$

6.6 Fluid continuum solvers

The essential difference between a solver and a model is that the scope of a model is limited to the continuum in which is defined, while the solver can span continua.

It is an accepted rule of thumb that optimum **under-relaxation factors** for *velocity* and *pressure* add up to 1 for steady-state simulations. If the residuals are converging well, it is acceptable to try increasing the under-relaxation factor for velocity (up to 0.9) and decreasing the pressure under-relaxation factor (to 0.1).

For Transient Simulations Under-relaxation factors of 0.9 (*velocities* and scalars) and 0.5 (*pressure*) work well in most cases. These values are higher than in steady-state cases since the contribution of the transient term to the partial flow equations has the same effect as under-relaxation.

6.6.1 Time-step configuration

For transient simulations, time is an additional coordinate.

Generally, numerical procedures require that this coordinate is taken into account in addition to the spatial discretization, that is, the total time interval is subdivided into time-steps. The solution of the governing equations is obtained at different time levels whereby the solution at time t requires the solutions from previous time-levels. Time integration schemes are distinguished between the number of time-levels they use for integration and on which time-level the fluxes and sources are integrated.

To get the initial convergence for the wind flow in the domain, an Implicit Unsteady (*URANS*) analysis will be run. The following values were set under the **Solvers** tree:

- *Time-Step* is set as 1s
- *Temporal Discretization* is set as 2nd which equals to the Newmark's method of integration and allows bigger time steps to be used due to its increased accuracy over Euler's method.

The following values were set under the **Stopping Criteria** tree:

- *Maximum inner iterations* is set as 2. For more unstable cases and for higher accuracy that value can be increased.
- *Maximum Physical Time* is set as 200s.

6.6.2 Postprocessing

The evaluation of the physics continua and the convergence of the initial solution can be done by creating **Scenes** and **Monitors**.

Monitors

The convergence of the wall boundary solution can be done by monitoring the sum of equivalent wind forces acting on the building surfaces.

The reports were created, each one monitors the acting forces in each direction. Note that *Star – CCM+* uses the vector coordinates $[i, j, k]$.

In the **Report** tree under the *Flow/Energy* option, three (3) new *Force* reports were created. In the dialog box, these options were chosen:

- $[0, 0, 1]$ for the **Drag** force in the along wind direction

- $[0, 1, 0]$ for the **Lift** force
- $[1, 0, 0]$ for the drag force in the across-wind direction named **Side**
- As input parts, all the surfaces of the building were chosen.
- The forces were selected to be calculated both by *Shear* and *Pressure*.

To visualise the reports, all of them were chosen at once and the option *Create Monitor and Plot from Report* in a single plot was chosen. To assess that the wind flow has properly converged, all the forces need to have stabilised.

Scenes

By creating *Scalar Scenes* the planar distribution of the

1. wind velocity,
2. Pressure coefficient,
3. Wall shear stress
4. and wall y^+ values can be reviewed.

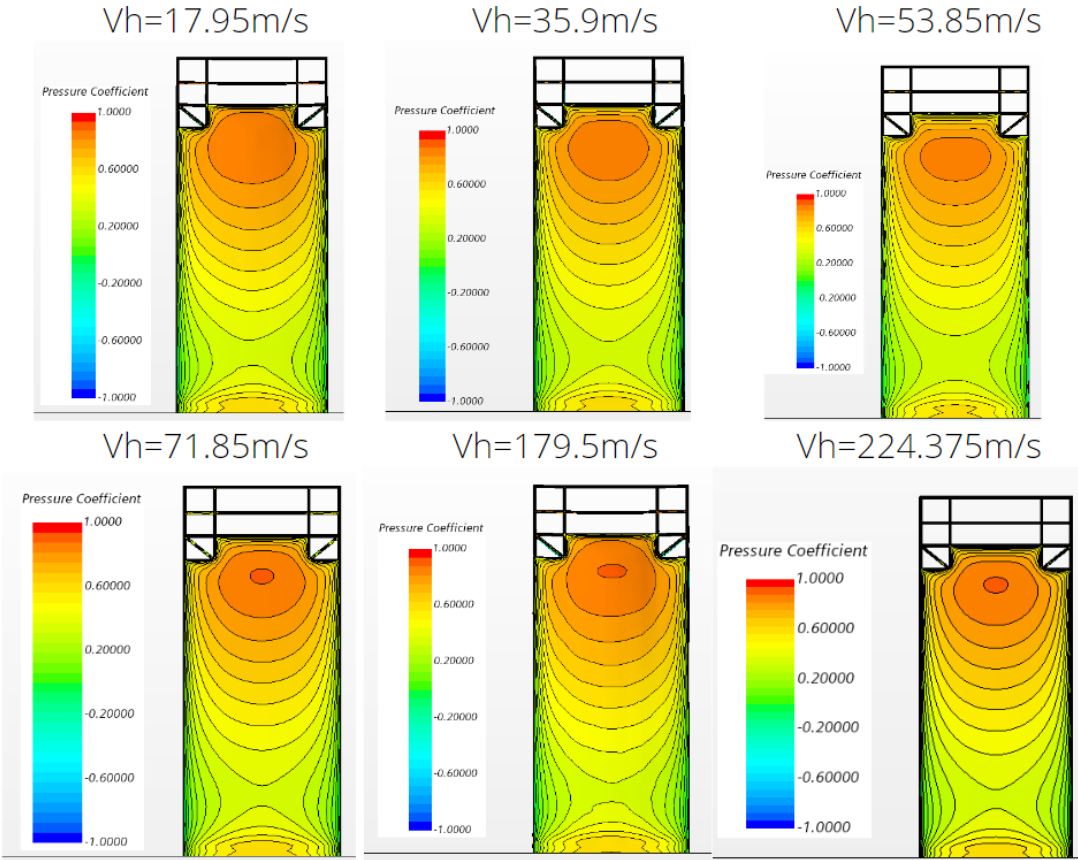


Figure 6.10: Pressure Coefficient

Velocity profiles parallel to wind flow

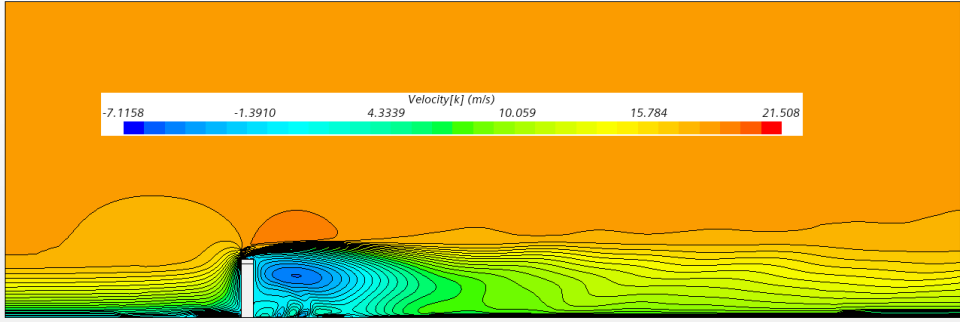


Figure 6.11: $V_{h1} = 17.95 \text{ m/s}$

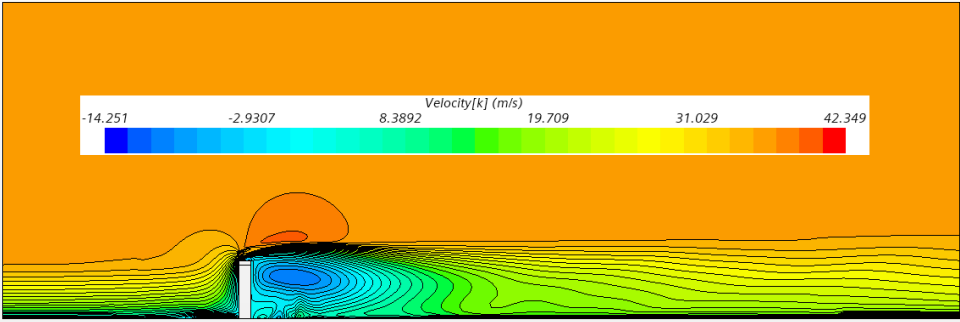


Figure 6.12: $V_{h2} = 35.9 \text{ m/s}$

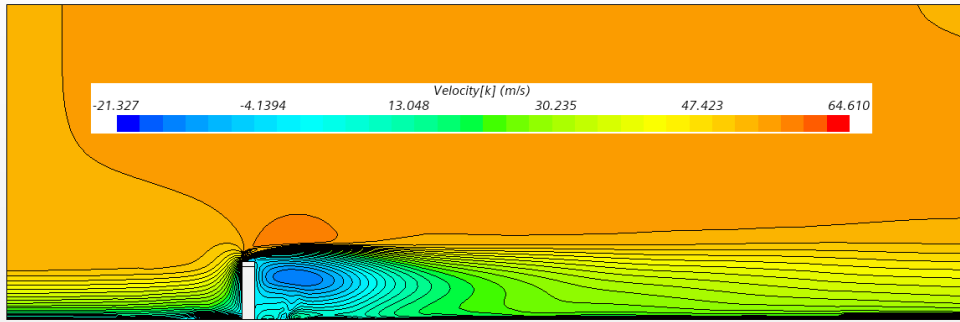
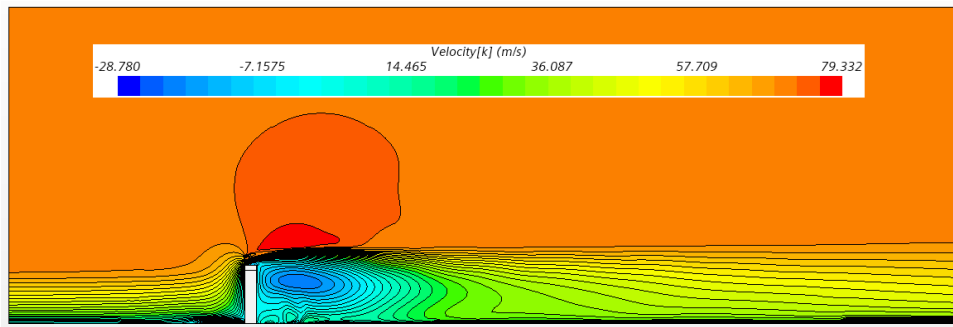
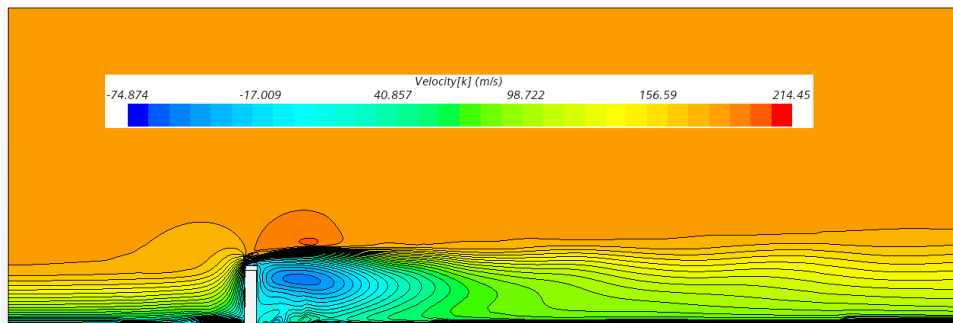
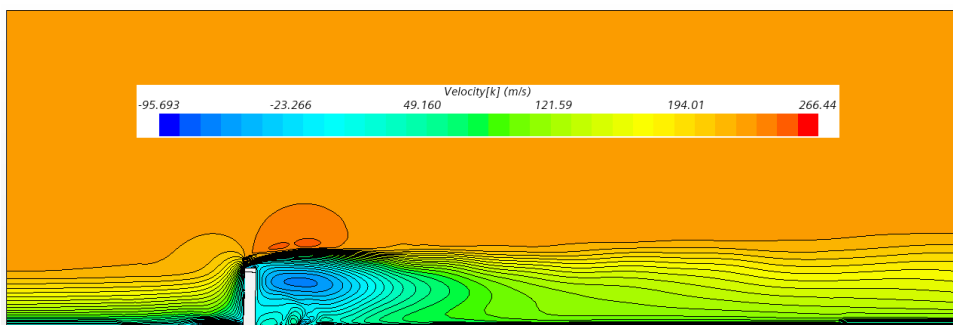


Figure 6.13: $V_{h3} = 53.85 \text{ m/s}$

Velocity profiles parallel to wind flow

**Figure 6.14:** $V_{h4}=71.85\text{m/s}$ **Figure 6.15:** $V_{h5}=179.5\text{m/s}$ **Figure 6.16:** $V_{h6}=224.375\text{m/s}$

Wall shear stress

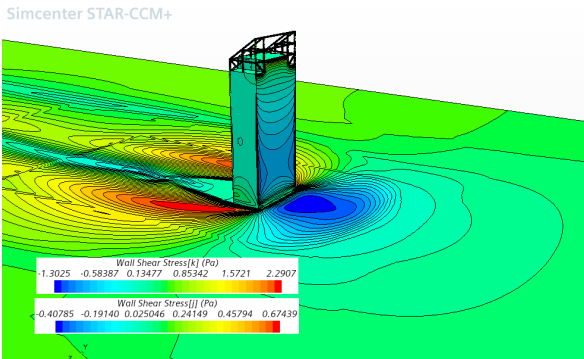


Figure 6.17: $V_{h1}=17.95\text{m/s}$

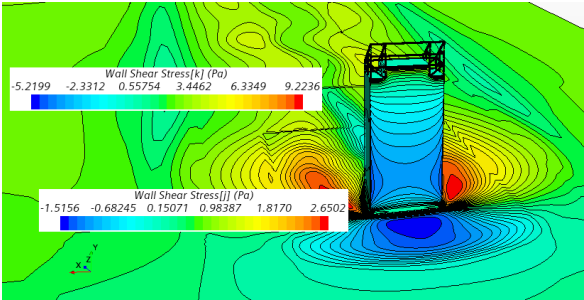


Figure 6.18: $V_{h2}=35.9\text{m/s}$

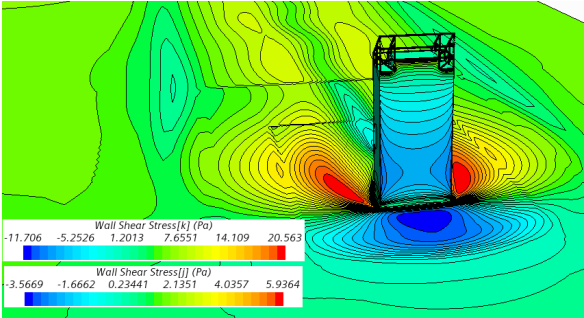


Figure 6.19: $V_{h3}=53.85\text{m/s}$

Wall shear stress

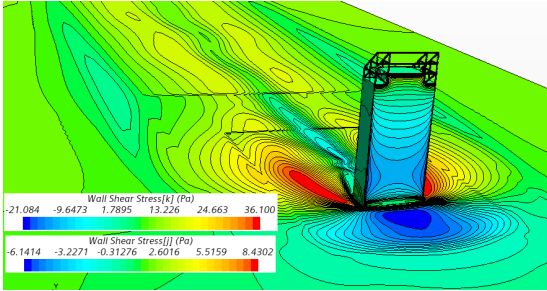


Figure 6.20: $V_{h4}=71.85\text{m/s}$

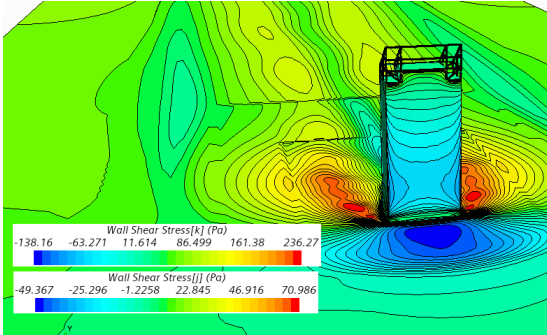


Figure 6.21: $V_{h5}=179.5\text{m/s}$

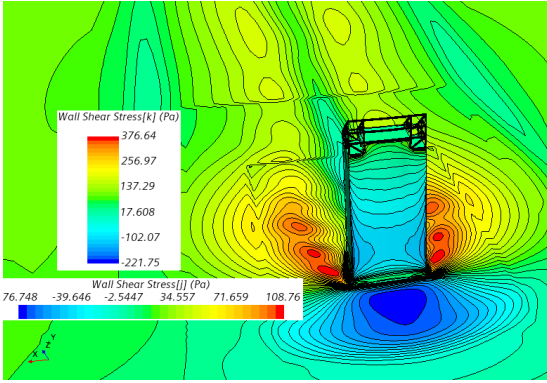


Figure 6.22: $V_{h6}=224.375\text{m/s}$

Wall y^+

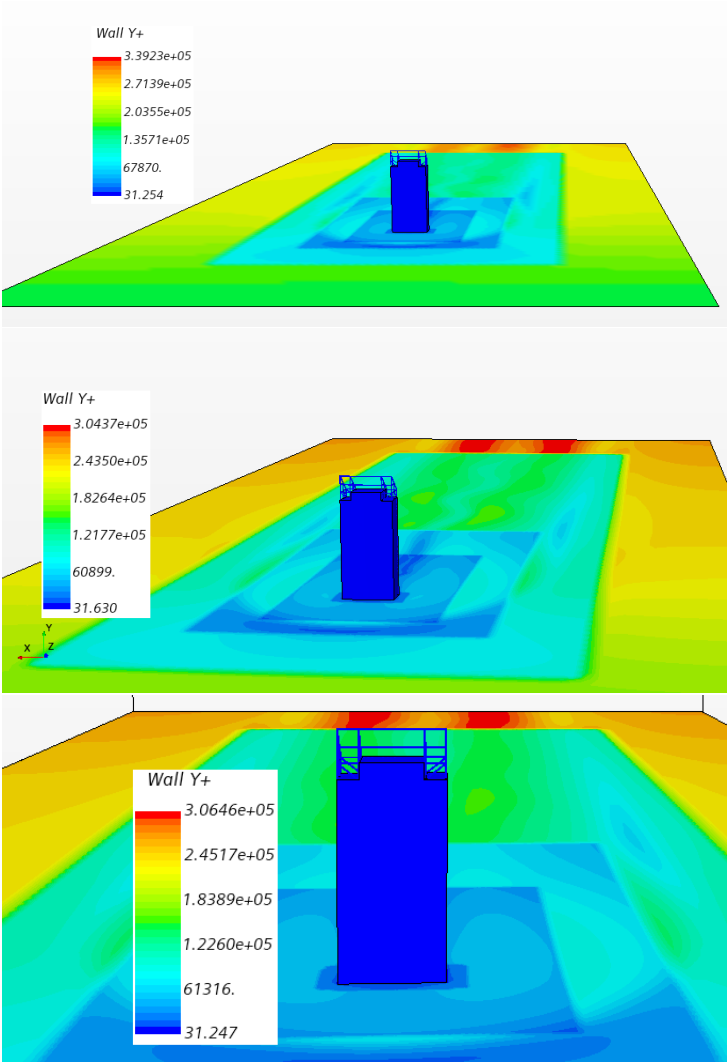


Figure 6.25: $V_{h3}=53.85\text{m/s}$

Wall y^+

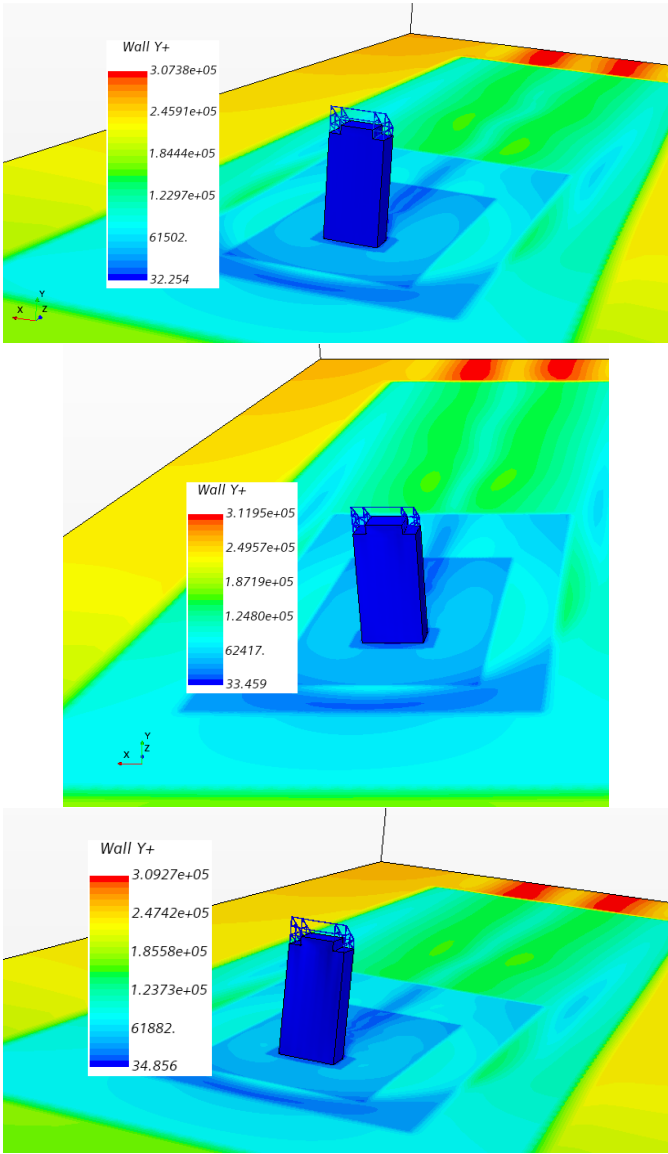


Figure 6.28: $V_{h6}=224.375\text{m/s}$

6.7 Discussion on the CFD part.

Pressure Streamlines

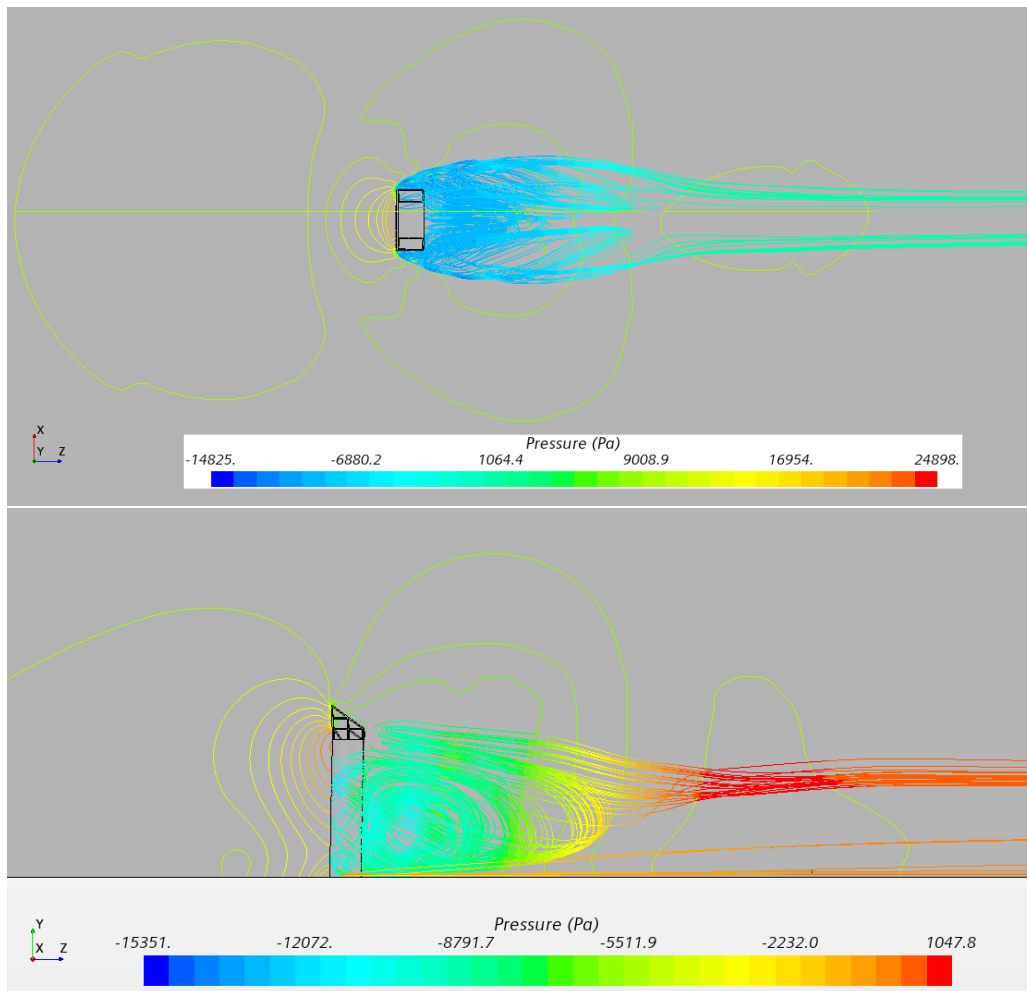


Figure 6.30: Suction field.

In regards to the *Wall Shear stress* and *Pressure Streamlines* scalar, two horseshoe vortices can be identified. Those vortices are characterised by a recirculation field developed within a narrow zone near the ground comprehending frontal and lateral areas upstream the building. On the other hand, fluid masses approaching the building at altitudes near the building height are raised up to pass by the building top and the truss structure and then they are launched above the recirculation zone behind the building to the wake region.

Two well-defined separation zones are found at the lateral walls of the building, where large vortexes are being shed alternatively, leading to strong oscillations of the building in the across-flow direction, as it will be shown in the last segment. The frontal recirculation zone is identified in the pressure field by a high pressure area on the ground in front of the building and the horseshoe vortexes are characterised by a narrow suction region (negative pressure, high turbulent wake field). This region cannot be dissipated due to a physical barrier formed by the presence of the horseshoe vortexes. This barrier acts on fluid masses flowing upstream the building and near the ground. The recirculation zones beside and behind the building are identified by regions with high suction (fields with negative pressure).

The *wall* y^+ values on the building are correctly in the log-law region, since their values exceed that of 30. This is desirable and planned so the wall treatment can be applied effectively. Also, *Pressure Coefficient* scalar gives desirable and expected results on the distribution of surface pressure.

Chapter 7

Coupling between CAE and CFD code

STAR – CCM+ enables the implementation of a built-in two way coupling scheme, in which the *CFD* code transfers the traction wall loads, *Pressure* and *Wall shear stress* to *ABAQUS* at a constant interval time. After *ABAQUS* solves the dynamic, implicit step for those loads it transfers back the corresponding displacements which are used as input for the morphing phase.

During the co-simulation, data is automatically exchanged between *Simcente STAR – CCM+* and *ABAQUS* using the *SIMULIA Co-Simulation Engine*. This technique differs from the file-based method in that the coupling between the codes is much stronger, and *Simcenter STAR – CCM+* and *ABAQUS* run simultaneously. Co-simulation can happen either by **surface-to-surface** mapping or by **node-to-surface** mapping. *Star – CCM+* offers additionally two coupling schemes, with their main difference being that of data transfers in the internal iterations. For weakly coupled applications, where the effect of the structure on the fluid is much larger than the effect of the fluid on the structure, the *Explicit Coupling* is recommended. Elsewise, for strongly coupled applications, choosing the *Implicit Coupling*, allows the simulations to exchange data more than once per time-step, and therefore allows the use of larger time-steps.

The data transfer in the coupling phase is done in this work via surface-to-surface mapping. For that reason, it is essential the coupling surfaces to be the exact same in both codes, more so in geometry and less in mesh size. Additionally, *Implicit Coupling* was chosen as the coupling scheme, being better for *FSI* applications.

The coupling scheme can be visualised below via a flow chart which indicates also the transfer interval frequency:

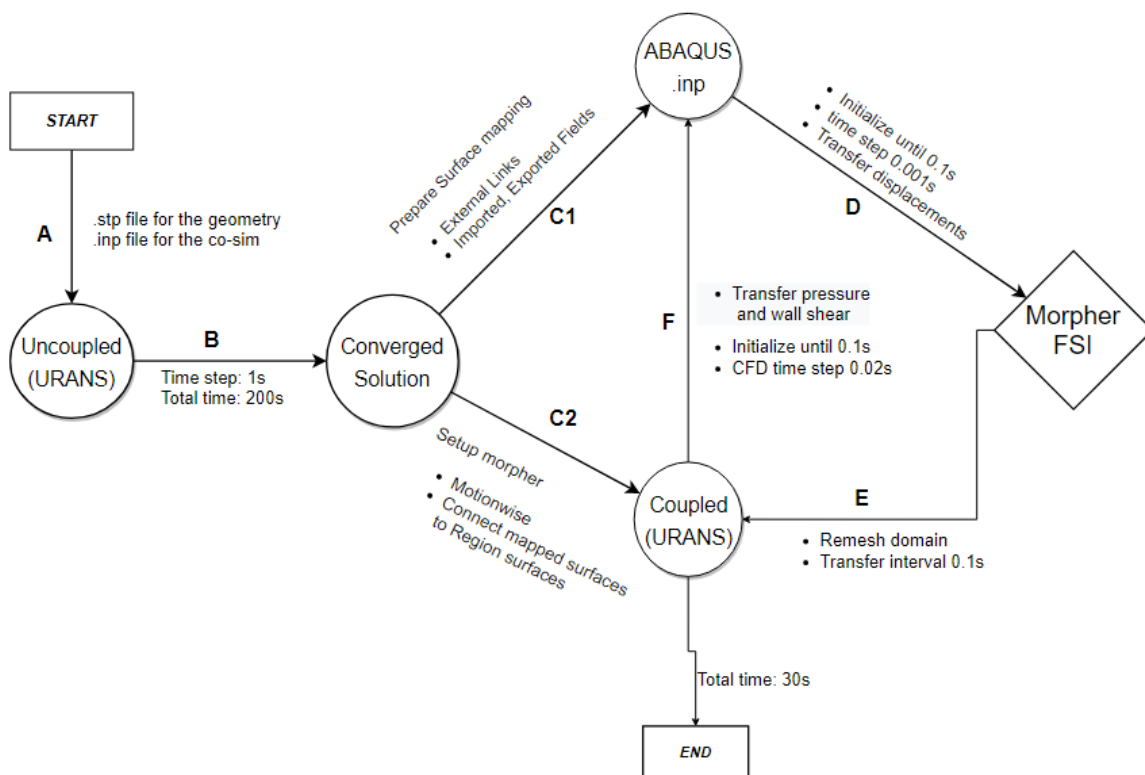


Figure 7.1: Co-Simulation flow chart

7.1 Setting up coupling

After the wind field has been established and converged, the following co-sim models must be enabled in the *Physics* continua:

- Co-Simulation
- Abaqus
- Abaqus Implicit Coupling

Furthermore, one additional *Physics Continuum* should be created for the external application. The external continua is set in the *External Links* tree. The following options were set:

- External Continuum
- External Application
- Abaqus
- Implicit Unsteady
- Surface Three Dimensional

Lastly, if one wishes to start the co-sim from $t_0 = 0.0s$ and not $t_0 = 200.0s$, under **Clear Solution** only the *History* should be erased.

7.1.1 Solvers configuration for the co-simulation

The following values were changed under the **Solvers** tree:

- *Time-Step* is set as $0.02s$
- *Maximum inner iterations* is set as 3. For more unstable cases and for higher accuracy that value can be increased.

- *Maximum Physical Time* is set as 30s. This value should be the same as the implicit dynamic's time period in *ABAQUS*.

7.1.2 Setting up morphing

Simulating the *FSI* requires that the mesh is being updated in each transfer interval with the displacements from *ABAQUS* solution. This is controlled by the mesh morpher.

Under the **Motion** tree, a new *Motionwise* morphing motion was created. It is important to enable the *Automatic Thin-Out* option as well and set its value to 0.5. This value increases the strength of the automatic thinning algorithm, which increases the density of control vertices.

Surface-to-surface mapping

Defining the coupled surfaces can be done by setting up **External Links**. The surfaces can be defined in the *Zones*. For *FSI* coupling, **Pressure** and **Wall Shear Stress** are set as *unmanaged* exported fields and displacements should be set as *managed* imported fields. The coupling /textitTransfer Interval time step is set as 0.1s.

Chapter 8

Results and discussions

As mentioned previously in segment 3.1, damping is directly correlated with the deformations of the structural system; it becomes apparent that the resulting discussion must be based on them. Hence, four point probes were created in the surface of the building to monitor the displacements there.

1. *TopPoint*, is placed in the centre of the building's plan, at an elevation of $Y = 68m$. The damping parameters will be calculated by the displacements there.
2. *FrotPoint*, is placed at the highest point of the building's surface, $Y = 73.6m$ and on the leeward side. This point will be used as a validation for the displacements measured at the previous probe.
3. *RightY*, is placed at the rightmost corner of the building's plan, at an elevation of $Y = 68m$
4. *LeftY*, is placed at the leftmost corner of the building's plan, at an elevation of $Y = 68m$. The last 2 points will be used to validate that only the translational eigenmodes will be activated during the wind load excitation, and not torsion.

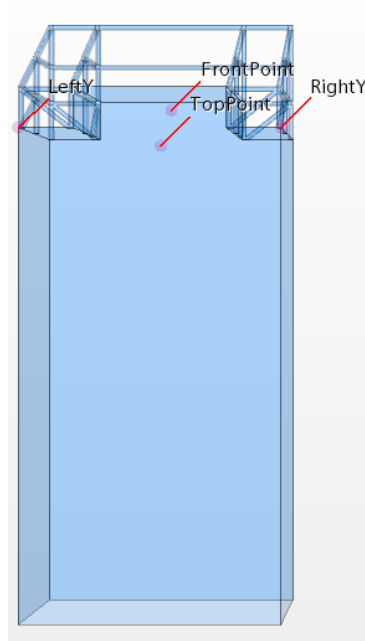


Figure 8.1: Surface probes

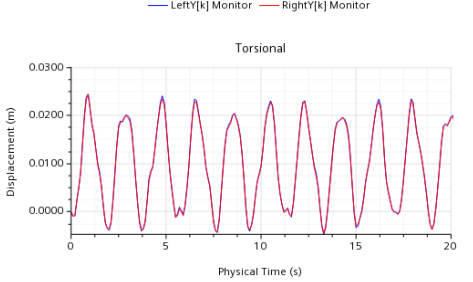
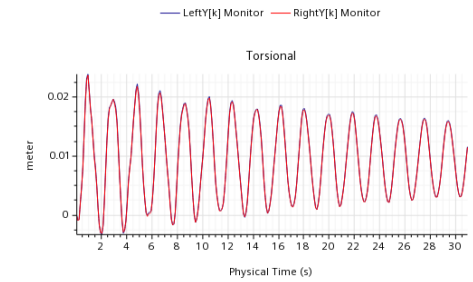
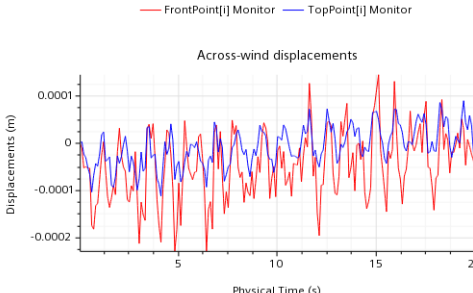
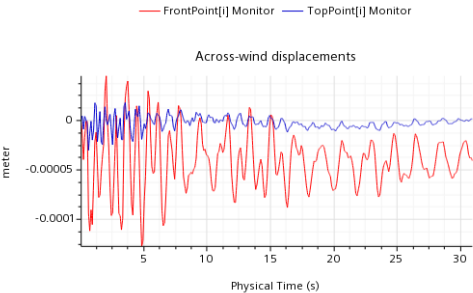
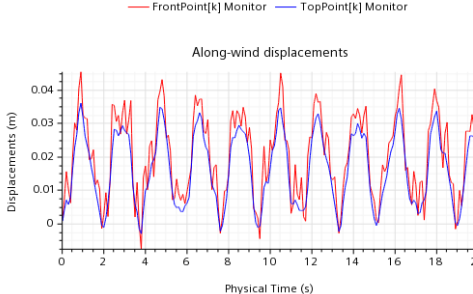
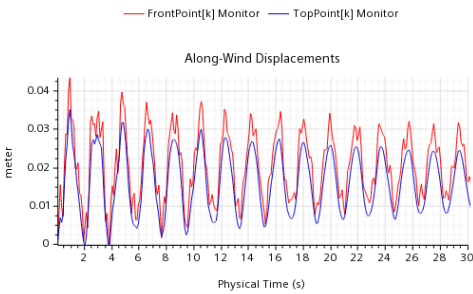
Below the respective displacements for each testing case will be visualised.

Note that *STAR – CCM+* uses the vector coordinate system $[x, y, z] = [i, j, k]$. The co-sim results were discontinued when adequate convergence had emerged.

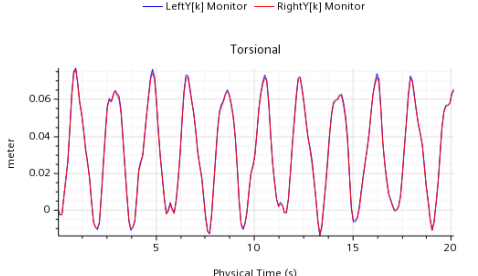
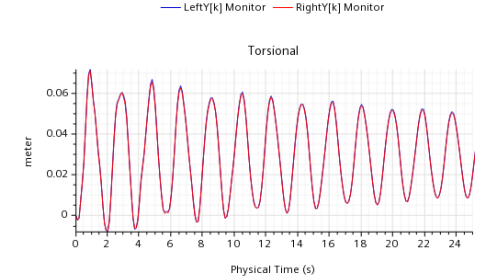
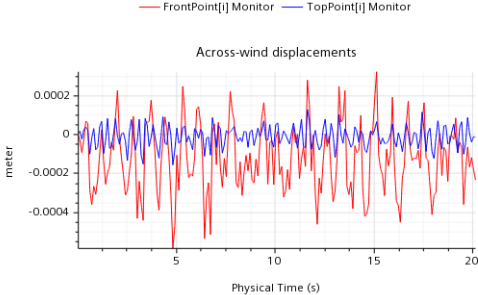
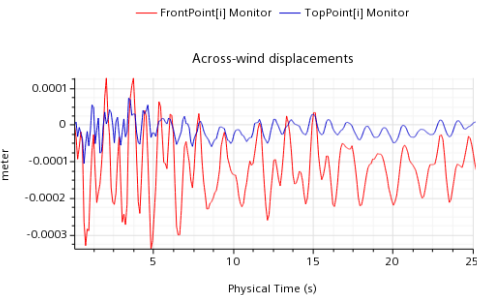
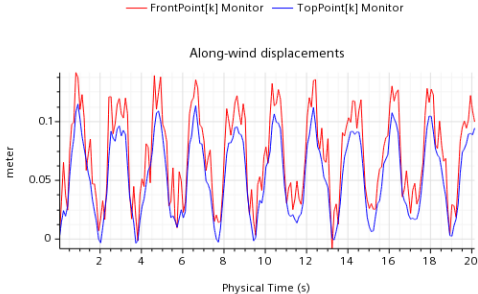
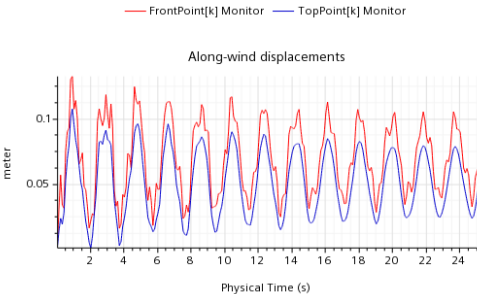
In following sections 8.1 and 8.2, the results from the coupling procedure can be viewed for each test scenario. It is noted that in the lower wind speed spectra, the structural response relies heavily on structural damping (Model 1), while as the wind speed increases the roles shift so that the aeroelastic damping becomes more prevalent. As expected, the frontal wall of the building is always submitted to positive pressures owing to the direct exposure of this wall to the wind stream, whilst the other surfaces walls are submitted to negative pressures due to the separation of the flow at the top and lateral walls, which leads to the formation of suction regions. One could also observe that oscillations occupied mainly in the along-wind direction for low wind speeds. As the wind speed is increased, displacements are mainly directed in the across-wind direction owing to the influence of an asymmetrical wake flow developed from separation occurring on the lateral walls of the building.

8.1 Displacement Time History, Model 1 & Model 4

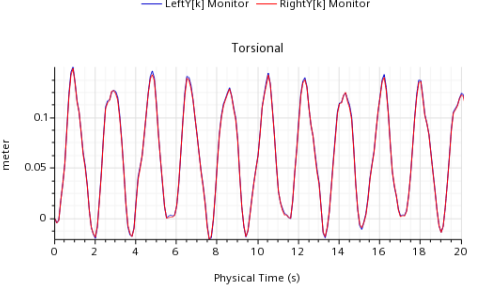
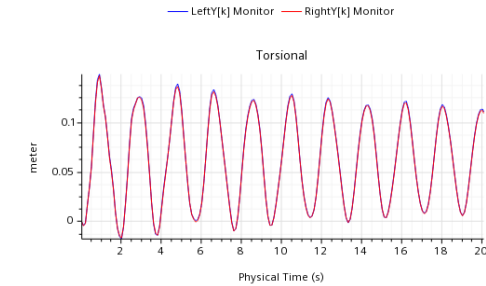
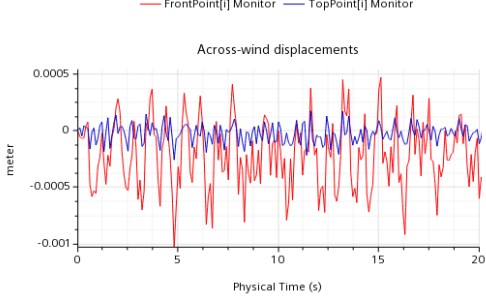
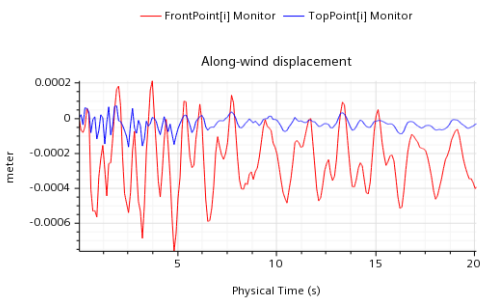
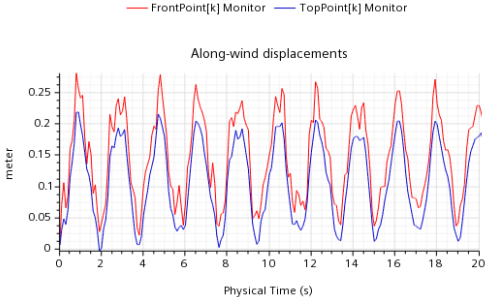
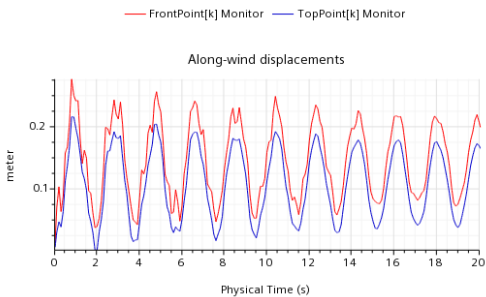
8.1.1 $V_h=17.95$ m/s



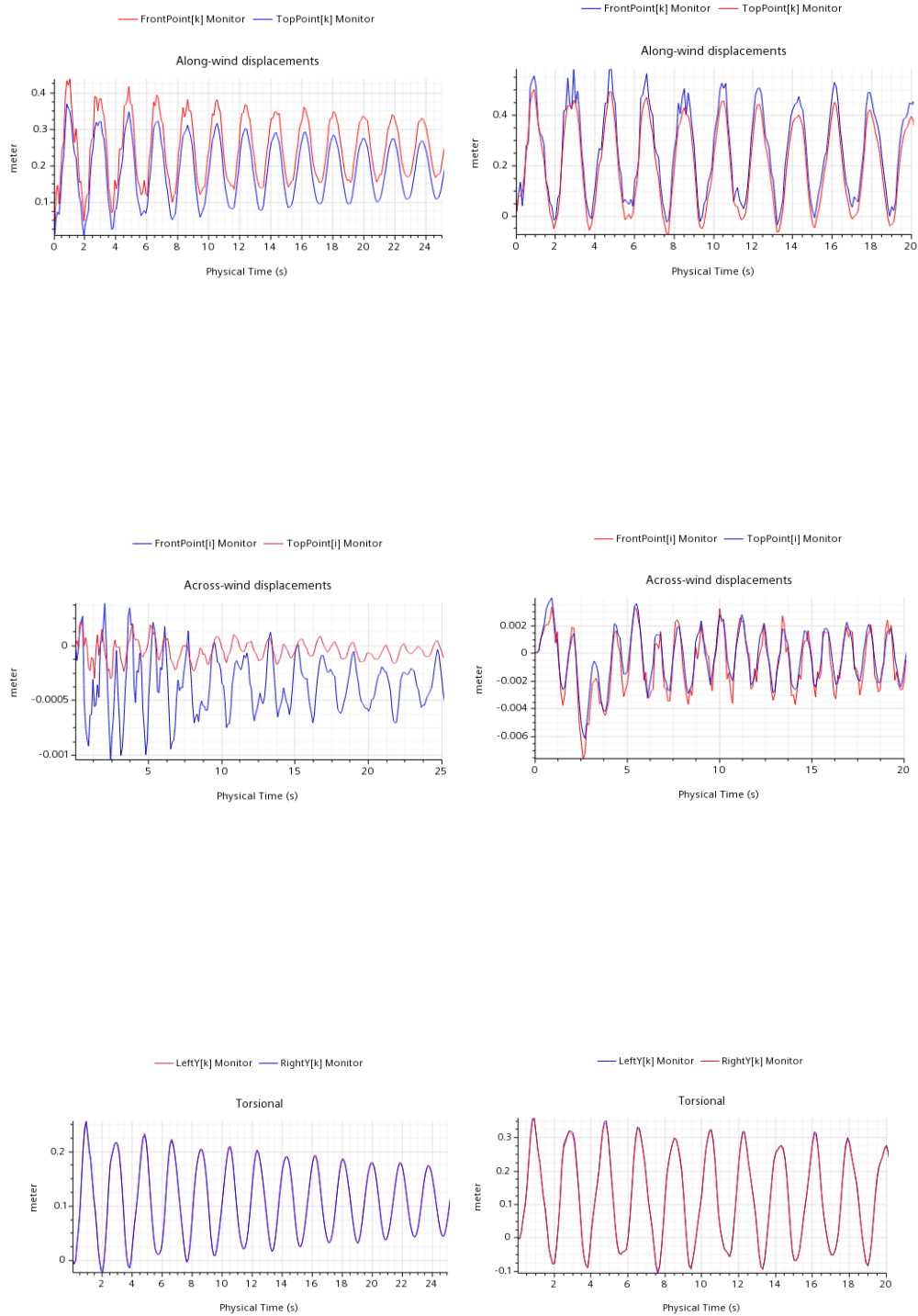
8.1.2 $V_h=35.9$ m/s



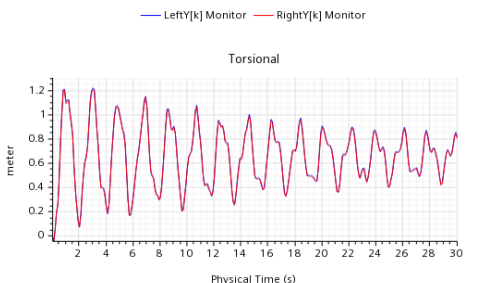
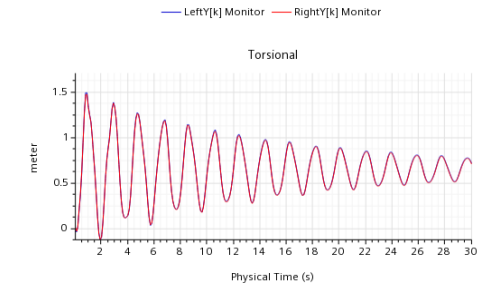
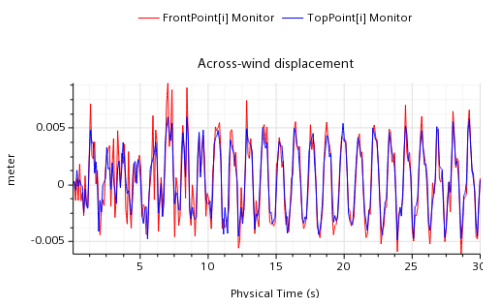
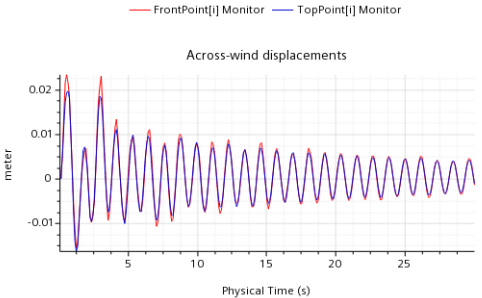
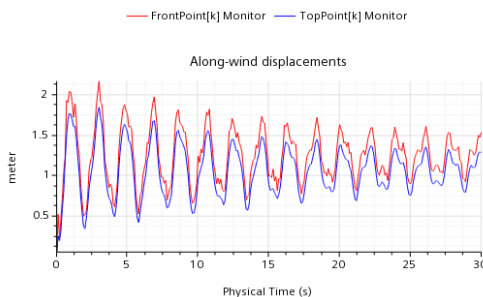
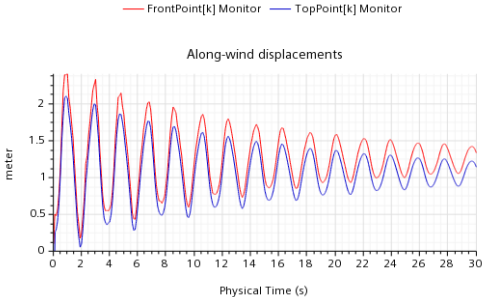
8.1.3 $V_h=53.85$ m/s



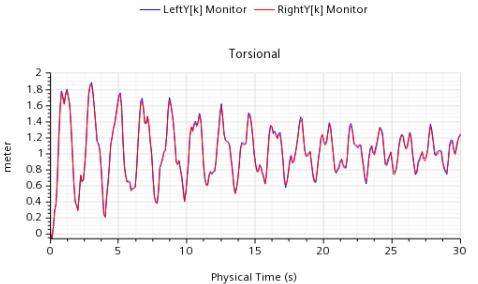
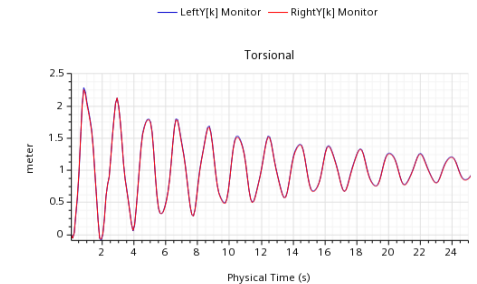
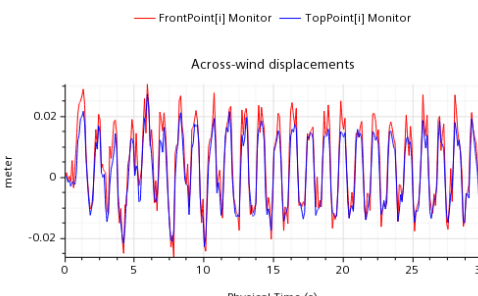
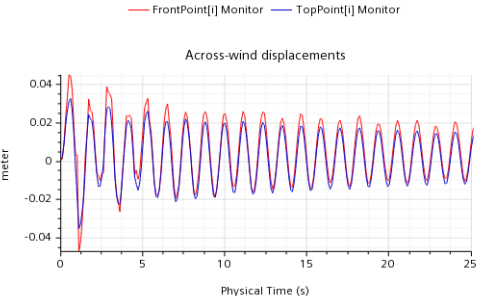
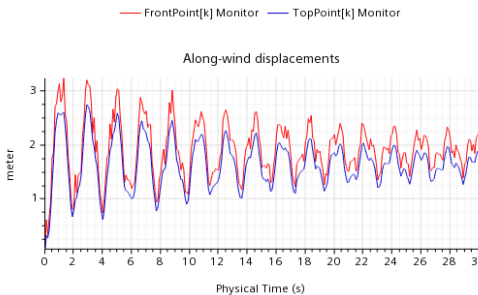
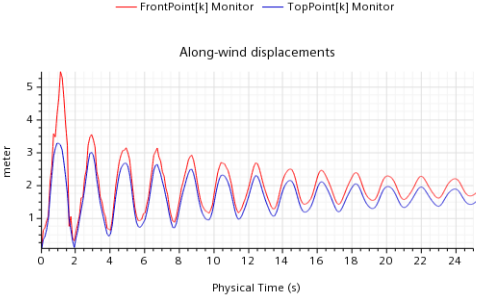
8.1.4 $V_h=71.8$ m/s



8.1.5 $V_h=179.5$ m/s

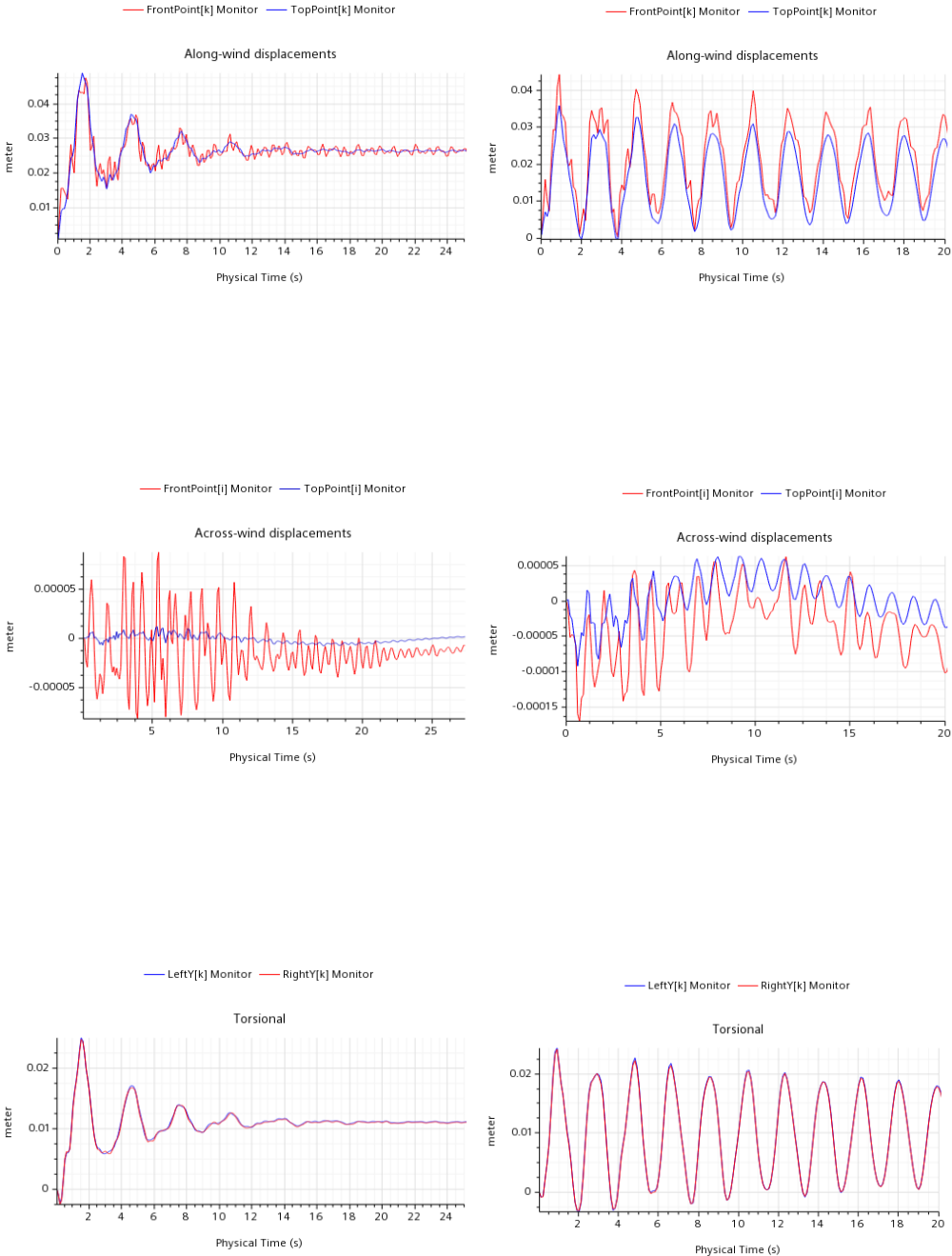


8.1.6 $V_h=224.375$ m/s

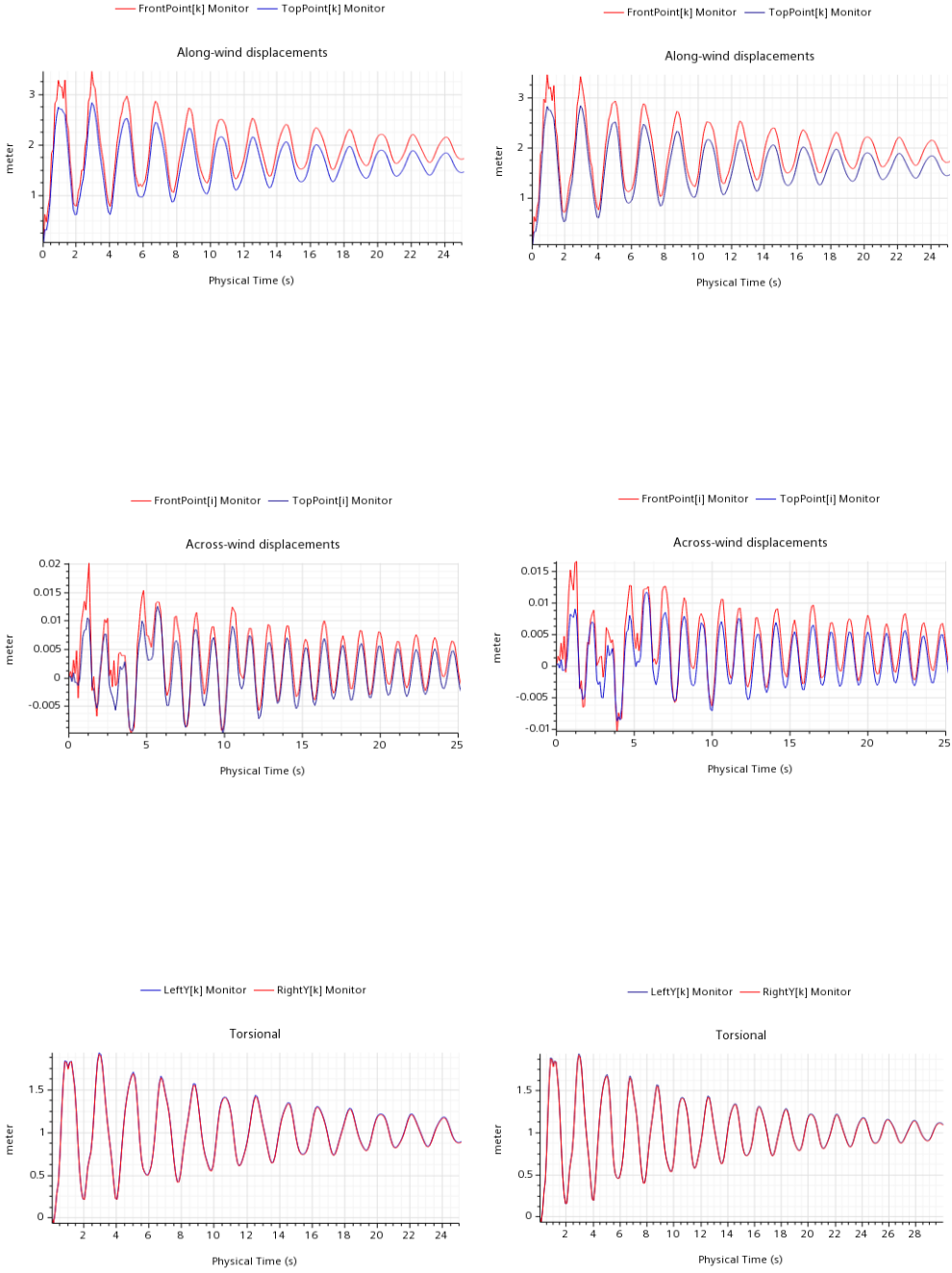


8.2 Displacement Time History, Model 2 & Model 3

8.2.1 $V_h=17.95$ m/s

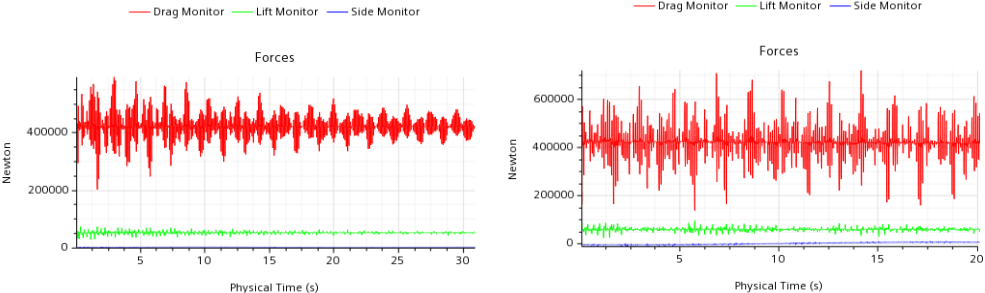


8.2.2 $V_h=224.375$ m/s

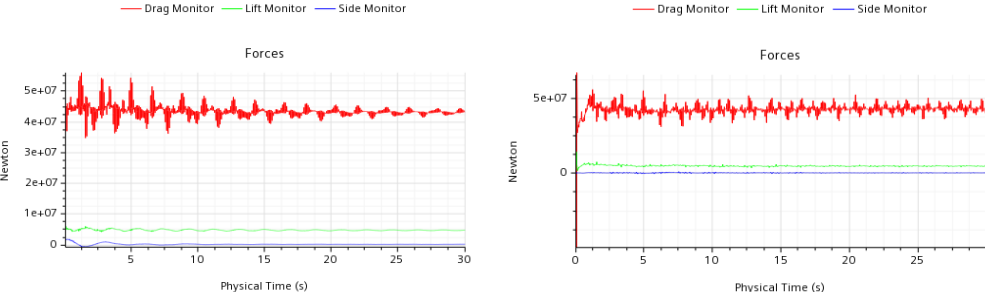


8.2.3 Acting forces, Model 1-Model 4

8.2.4 $V_h=17.95 \text{ m/s}$



8.2.5 $V_h=224.375 \text{ m/s}$



The strong oscillations of the **Drag forces** on the building showcase the fluid structure interaction. The determining force is that of Drag as it was expected, since it acts in the resistance of the along-wind displacements where the bigger deformations exists. It should be noted that as the damping and wind speed increases, so does the decay of each force’s amplitude.

An interesting topic of research would be to calculate the fatigue rate of timber connections under cyclic loading by implementing an *FSI* strategy.

8.3 Damping results.

Damping will be calculated by the along-wind displacements. As one can notice the **Displacement Time History** is not a smooth curve. That can be attributed to several reasons:

- The *ABAQUS* solver time is not the same as the fluid solver's. This can clearly be visualised in the lower wind speed cases. This was made out of necessity due to computational costs. (*Author's note: A 30s total run on a 4core processor at 3.2 Ghz needed approximately 1.5 days to complete*).
- The transfer interval time of the morpher in the coupling process is not the same as *ABAQUS* and *STAR – CCM+* solver.

However, some general remarks can be made about the quality of the damping,

1. In the lower wind speeds, namely $Vh_1 = 17.95m/s$ until $Vh_3 = 53.85m/s$, the aeroelastic damping has almost no effect in the reduction of displacements in the building. This is to be expected since the geometry of the building is not slender and vortex shedding does not happen fast enough in the separation field.
2. The maximum wind speed by *EC1* for the *SLS* criteria on the specific building is around $20m/s$. Thus, aeroelastic damping is not a parameter worth considering on this specific type of geometry and building.
3. The torsional plot shows good results since both probes are completely in sync, thus vortex shedding provides only translational oscillations.
4. Aeroelastic damping is not a stable parameter, and relies heavily on the wind conditions at the site as well as the geometry of the obstacle.

Damping was calculated using the method of logarithmic decrement, which becomes less and less precise as the damping ratio increases past about 5 %, but is reasonably stable in the lower regions.

$$\delta = \frac{1}{n} * \ln\left(\frac{x_t}{x_{t+nT}}\right) \tag{8.1}$$

Then, the ratio of critical damping was calculated using the following formula:

$$\xi = \frac{1}{\sqrt{1 + \left(\frac{2\pi}{\delta}\right)^2}} \tag{8.2}$$

In the following table, the damping ratios can be seen for each case, by selecting 2 appropriate peaks $n = 5$ periods away. A better way to calculate the damping ratio is by running a much longer analysis for every scenario until the amplitude of the oscillation has converged.

Critical damping ratio of Model 1

V_{cr} fraction	$V_{cr}/nW = 1$	$V_{cr}/nW = 2$	$V_{cr}/nW = 3$	$V_{cr}/nW = 4$	$V_{cr}/nW = 10$	$V_{cr}/nW = 12.5$
$\xi\%$	0,44	0,45	0,56	0,58	1,10	1,25

Critical damping ratio of Model 4

V_{cr} fraction	$V_{cr}/nW = 1$	$V_{cr}/nW = 2$	$V_{cr}/nW = 3$	$V_{cr}/nW = 4$	$V_{cr}/nW = 10$	$V_{cr}/nW = 12.5$
$\xi\%$	0,05	0,09	0,16	0,34	0,55	0,95

V_{cr} fraction	$V_{cr}/nW = 1$	$V_{cr}/nW = 2$	$V_{cr}/nW = 3$	$V_{cr}/nW = 4$	$V_{cr}/nW = 10$	$V_{cr}/nW = 12.5$
$\xi\%$	0,05	0,09	0,16	0,34	0,55	0,95

Critical damping ratio of Model 2

V_{cr} fraction	$V_{cr}/nW = 1$	$V_{cr}/nW = 12.5$
$\xi\%$	2,27	1,24

Critical damping ratio of Model 3

V_{cr} fraction	$V_{cr}/nW = 1$	$V_{cr}/nW = 12.5$
$\xi\%$	0,70	1,60

8.4 Discussions

In the previous section, the damping values were derived by using the method of logarithmic decrement. While this method is tried and true for calculating the damping in sinusoidal force based simulations, it falls short when used under continuous random loading, such as in a wind tunnel.

By comparing the damping ratios of each Model, the following proposals can be made:

1. The case of wind speed $V_h = 1$ is thought to provide very little aeroelastic damping and can be ignored. This way, the damping of **Model 1** is assumed to come only from structural damping.
2. By abstracting the damping ratios of Vh_1 from those of Vh_6 , the value of aeroelastic damping can be validated, on the basis that structural damping ratio does not increase with the increase of loading.
 - (a) Subtracting $\xi_{h_1} = 0.44$ from $\xi_{h_6} = 1.25$, the aeroelastic damping that occurs in **Model 1** is $\xi_{max} = 0.81$.
 - (b) By comparing the above value with the $\xi_{h_6} = 0.95$ of **Model 4**, an assumption can be made that the maximum aeroelastic damping is ~ 0.81 .
 - (c) Following the same train of thought for the $\xi_{h_1} = 0.44$ from $\xi_{h_3} = 0.56$ of **Model 1**, the aeroelastic damping in the case of $Vh_3 = 53.85m/s$ is ~ 0.12

By following the same methodology the damping ratio of the *SSI* under wind loading can be found:

- (a) Subtracting $\xi h_1 = 0.44$ of **Model 1** from $\xi h_1 = 0.70$ of **Model 3**, the aeroelastic damping that occurs in the case of $V_h = 1$ is ~ 0.26 .
- (b) Doing the same for $V_h = 6$, the value of ~ 0.35 can be calculated. Thus, as a structural component, *SSI* values remain relatively the same, and it is safe to assume that the proposed foundation can be replaced by an additive value of ~ 0.26 in structural damping.

Regarding **Model 2**, with semi rigid connections, the following conclusions can be made:

- (a) Under low wind loading, the semi-rigid model showed greater deformations in contrast to its rigid counterpart. That is to be expected.
- (b) However, under heavy wind loading, the displacements were **lower**, because of the lesser global stiffness that exists in the model, allowing for the vortex shedding to have greater impact on the stabilisation of the along-wind displacements.
- (c) Under low wind loading, the increased designation of damping allowed the building to balance its oscillations after 4 time periods. Also, the eigenperiod of the model in the along-wind direction was bigger, due to the difference of the natural frequencies of Model 2 to Model 1.
- (d) Assuming the damping assigned is true, the above phenomenon and the fact that the low wind speed scenario coincides with the design wind speed of Mjøstårnet, makes a good case for the ability of timber buildings having higher damping ratios than their conservative concrete counterparts.

8.5 Lock-in Phenomenon

To demonstrate the lock-in phenomenon, a new revised CFD model was configured. The changes that were made were:

1. The vortex shedding frequency, f_n as mentioned in the Glossary, was now set equal to the natural frequency of the building in the *across-wind direction*.
2. Strouhal number St was chosen to be equal to 0.15 which is a more appropriate value according to the bibliography [84].

Thus, the critical velocity V_{cr} on this scenario equals to:

$$V_{cr}^{lock-in} = \frac{35.9 * 0.78}{0.15} = 186.68m/s$$

By following the methodology that can be found in Appendix D, the inlet turbulence conditions were selected as:

$$k = 91.8$$

$$\omega = 0.267$$

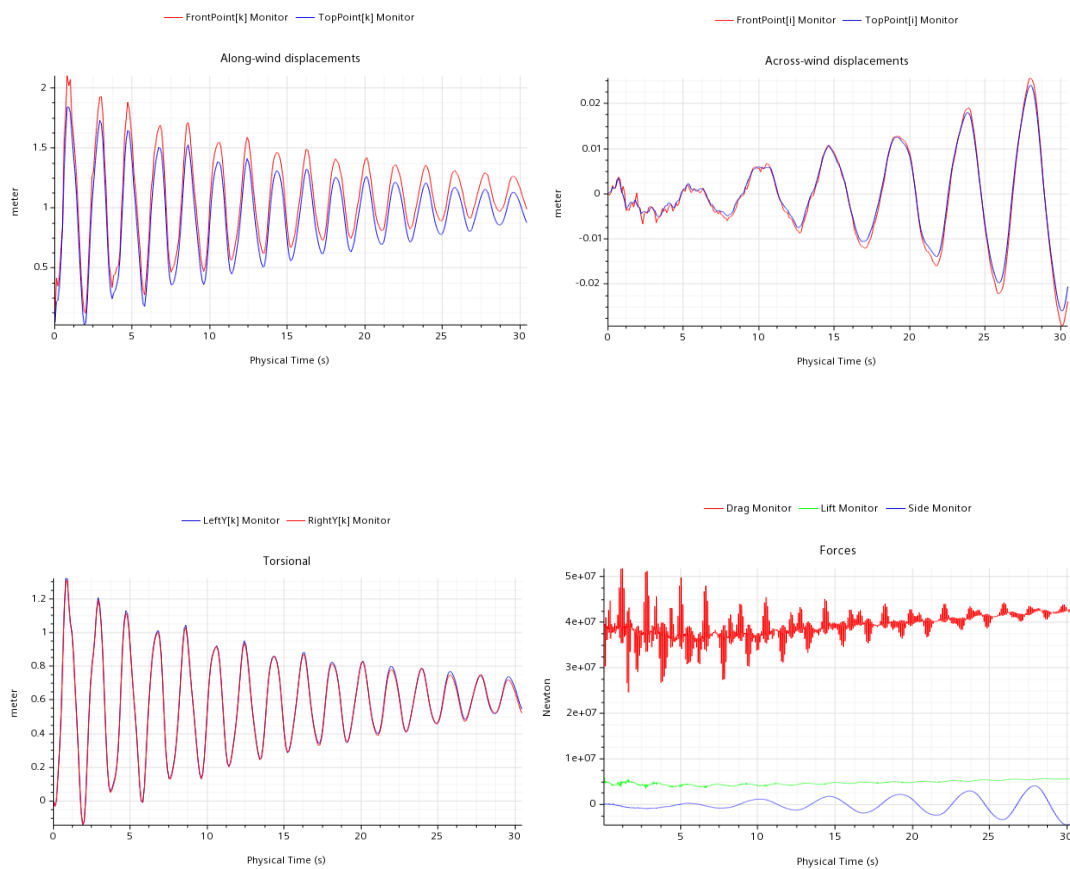
Also, the *Power – Law Velocity Inlet* equation was slightly modified. The modifications were:

- The power n was reduced to 0.2 which is nearer to the conventional value of $\alpha = 1/7$ that is most commonly used.
- The inlet BC of the *power – law* was set to rise until $Y = 200m$ above ground.

There can be no distinctive "best" parameter value selection, and a sensitivity analysis should be done in the exact same model and turbulent conditions to get a conclusive answer.

8.5.1 Lock-In Displacements

The structural response of the building in the along wind direction is firstly characterised by large displacements in the along-wind direction which after the first oscillation and the establishment of FSI , they are gradually damped due to aeroelastic damping and structural damping. In contrast, in the across-wind direction, displacements with small amplitudes are found in the first oscillation of the aeroelastic analysis. After that moment and the establishment of FSI , when synchronisation between the structural and vortex shedding frequencies occurs, the amplitudes of transversal oscillations are increasing leading to a structural response characterised by sway motion. That can also be validated by the *Forces* plot where in contrast to the previous case scenarios, the drag forces in the across-wind direction are increasing whilst the drag forces in the along-wind direction decrease rapidly.



8.5.2 Q-criterion

Evaluating vortex shedding and vorticity can be quite difficult by using standard scalar scenes. The coherent vortical structures in the flow can provide valuable understanding of the flow field in a variety of cases and give a clear way to identify the horseshoe structures that should exist in the separation field. The visualisation can be done by implementing the *Q – criteria* function. The *Q* criterion is written as:

$$Q = \frac{1}{2} * (\text{Vorticity}^2 - \text{Strain Rate}^2) \tag{8.3}$$

When $Q > 0$ there exists dominance of the rotational component over the stretching component in deformation of a fluid element. In those fields, vortices can be identified.

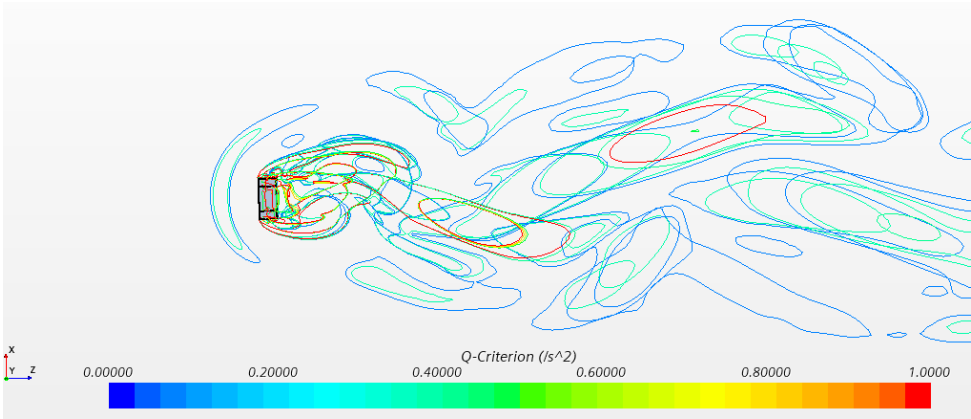


Figure 8.2: Q criteria-Vortex Shedding

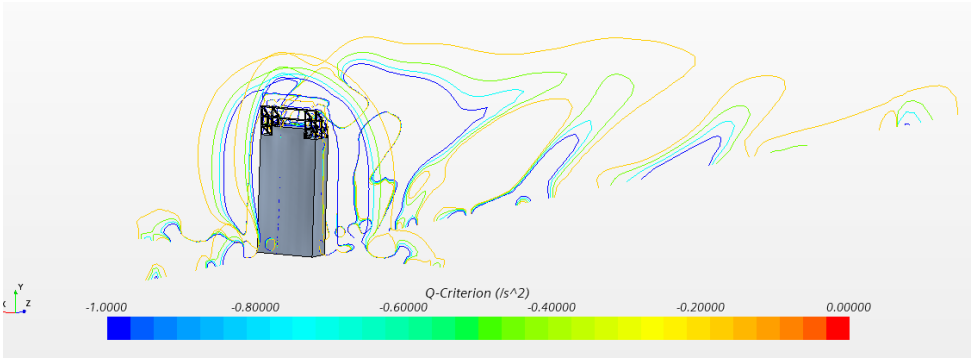


Figure 8.3: Q criteria-Horseshoe vortices

Conclusion

During this thesis, all simulations performed without structural damping led to a considerable increase of r.m.s. responses in the along-wind direction. This phenomenon became less apparent in the along-wind direction as the wind speeds came near the critical velocity, while simultaneously the across-wind response stabilised and in the case of the undamped model is even began to increase.

It also became clear that *aeroelastic damping* is an elusive parameter that cannot be calculated with certainty. In this work aeroelastic damping can reach values up to $\xi = 0.95\%$ of the critical damping ratio, alas that is done in unrealistic high speeds. Regarding the satisfaction of *SLS* criteria, where wind speeds are expected to be relatively under 20m/s , aeroelastic damping is minuscule and the value provided is not considered completely valid due to a considerable increase of r.m.s. responses. Aeroelastic damping is worthy of being considered in cases of tall slender buildings, if the ratio of the height to its narrowest side exceeds 7 [85]. In Mjøstårnet, that ratio is $73.6/15.3 = 4.8$ which falls short of this description of slender building.

For tall timber buildings, it is proposed to research the cyclic loading and fatigue rate of connections under wind loads by utilizing the *FSI* procedure, since the simulations in this work show that this is highly attainable by using a standard *PC* and considering that less accuracy is needed.

Appendix A

Element sections

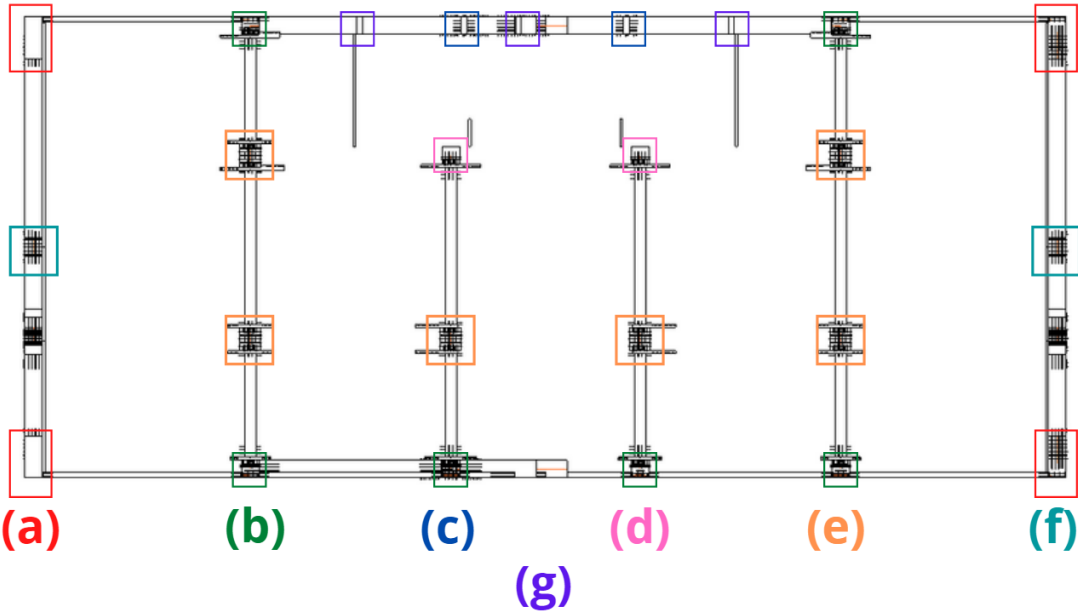


Figure A.1: Column elements numbering

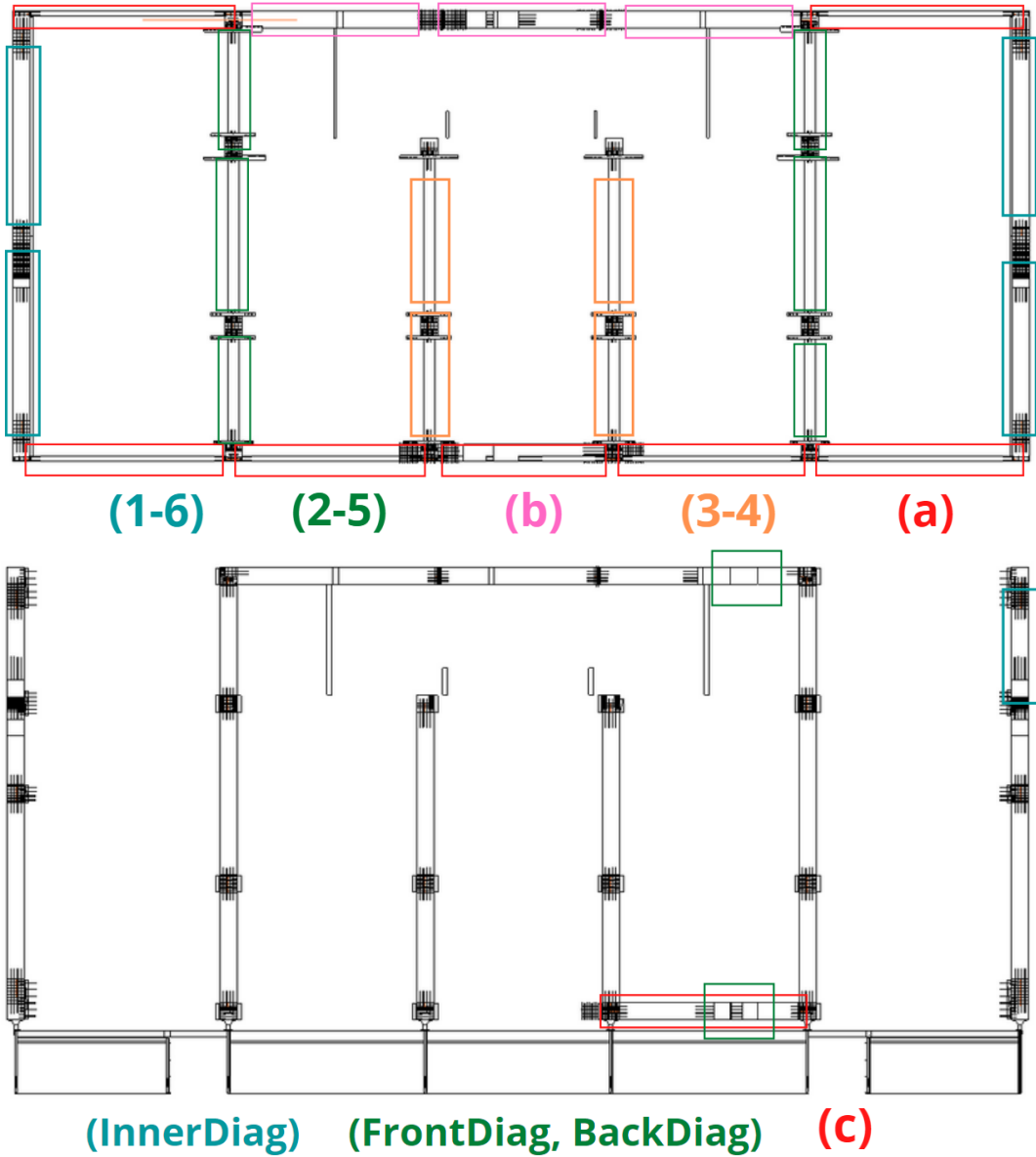


Figure A.2: Beam elements numbering

Part	Name/ Sets	Floor 1-5	Floor 5-12	Floor 12-18
		Dimensions(m)	Dimensions(m)	Dimensions(m)
Back_Columns	OuterColumns_a	a=1.485 b= 0.625	a=1.485 b= 0.625	a=1.485 b= 0.625
Back_Columns	InnerColumns_b	a=0.625 b= 0.625	a=0.625 b= 0.625	a=0.625 b= 0.625
Back_Columns	BackBracing_e	a=0.625 b= 0.215	a=0.625 b= 0.215	a=0.625 b= 0.215
Back_Columns	BackBracing_f	a=0.625 b= 0.190	a=0.625 b= 0.190	a=0.625 b= 0.190
Back_Beams	FacadeBeams_a	a=0.190 b= 0.405	a=0.190 b= 0.405	-
Back_Beams	ElevBeams_b	a=0.625 b= 0.225	a=0.625 b= 0.225	a=0.625 b= 0.225
Back_Diag	BackDiag	a=0.495 b= 0.625	a=0.495 b= 0.625	a=0.495 b= 0.625
Front_Columns	OuterColumns_a	a=1.485 b= 0.625	a=1.485 b= 0.625	a=1.485 b= 0.625
Front_Columns	InnerColumns_b	a=0.625 b= 0.625	a=0.625 b= 0.625	a=0.625 b= 0.625
Front_Beams	FacadeBeams_a	a=0.190 b= 0.405	a=0.190 b= 0.405	-
Front_Beams	DiagBeams_c	-	-	a=0.625 b= 0.300
Front_Diag	FrontDiag	a=0.495 b= 0.625	a=0.495 b= 0.625	a=0.495 b= 0.625
Inner_Beams	BeamsRow1_6	a=0.439 b= 0.625	a=0.439 b= 0.625	a=0.585 b= 0.625
Inner_Beams	BeamsRow2_5	a=0.675 b= 0.395	a=0.675 b= 0.395	a=0.720 b= 0.625
Inner_Beams	BeamsRow3_4	a=0.395 b= 0.675	a=0.395 b= 0.675	a=0.720 b= 0.625
Inner_Columns	InnerColumns_c	a=0.625 b= 0.630	a=0.625 b= 0.630	a=0.625 b= 0.630
Inner_Columns	InnerColumns_d	a=0.810 b= 0.725	a=0.720 b= 0.675	a=0.625 b= 0.630
Inner_Columns	InnerColumns_g	a=0.625 b= 0.630	a=0.625 b= 0.630	a=0.625 b= 0.630
Inner_Diag	InnerDiag	a=0.625 b= 0.990	a=0.625 b= 0.990	a=0.625 b= 0.990

Appendix B

Timber Connections

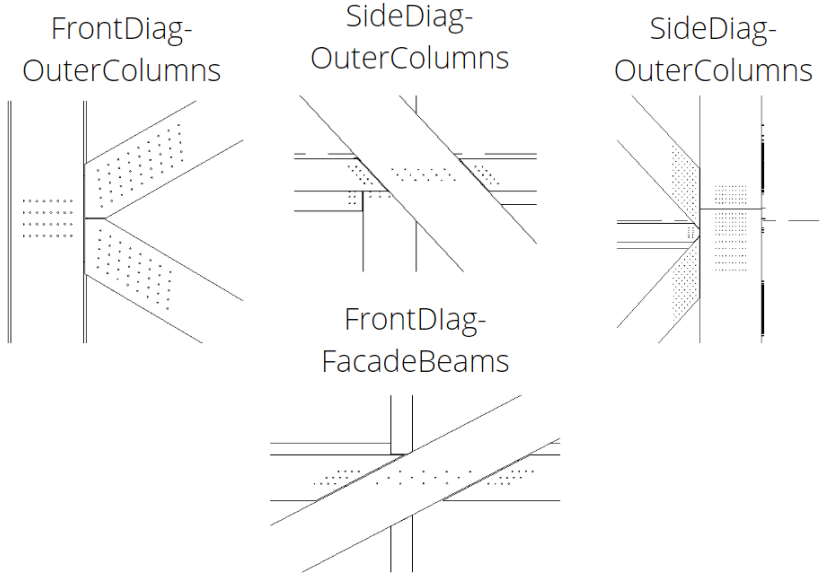
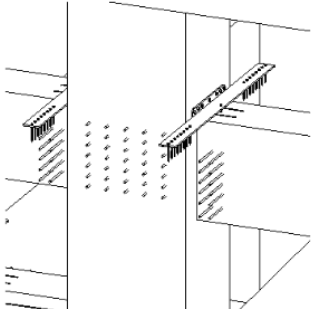
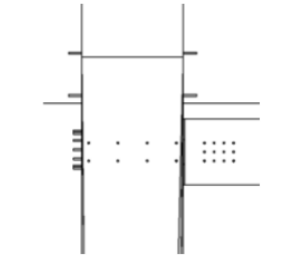


Figure B.1: Timber connections.

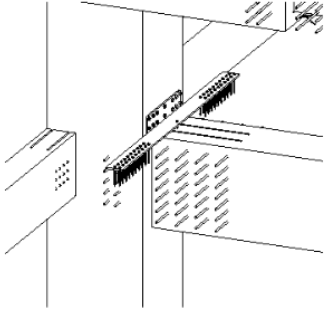
InnerBeams-
InnerColumns



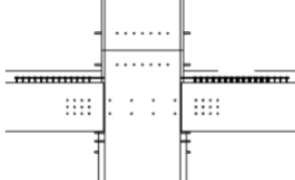
FacadeBeams-
OuterColumns



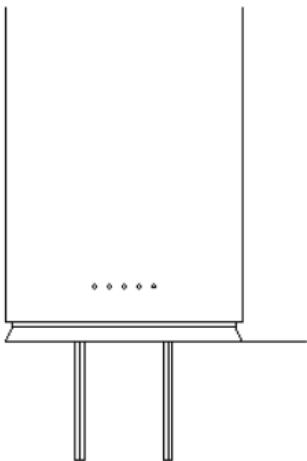
InnerBeams-
OuterColumns



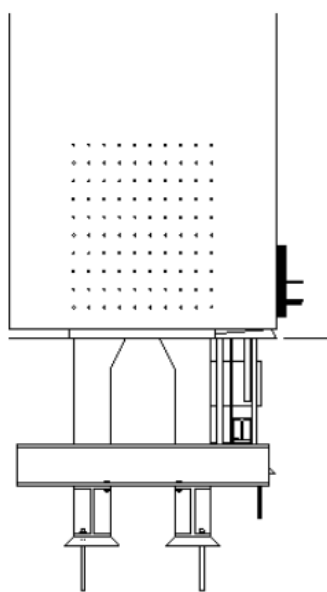
FacadeBeams-
FrontColumns



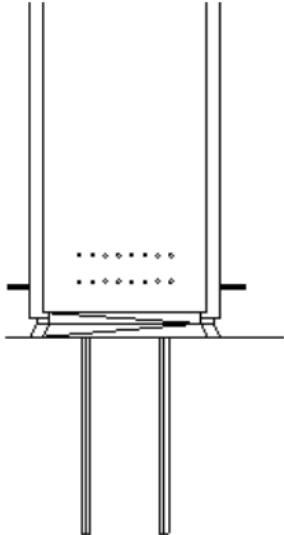
Foundation-
InnerColumns



Foundation-
OuterColumns



Foundation-
FrontColumns



As stated in the appropriate segment, 2, more than one stiffness matrix can be applied per *zero – length* element. In the case of timber connections, when calculating two-way connections connecting (i.e. BackBeams and BackColumns), the double amount of stiffness should be applied in their connection, in contrast to one way connections (i.e. OuterColumns and BackBeams). The connections are all done using a 4-slot-in steel plate or 4-slot-in steel plate.

FrontDiag-OuterColumns

The stiffness module for a connection is found in chapter 7 in *EC5 – 1*.

For a connection with steel or concrete, only the timber will deform, thus the stiffness can be doubled according to *EC1 – 4*, 7.1(3).

This connection has

$$K_{ser,dowel} = 2 * n_{sp} * \rho^{1.5} * \frac{d_c}{23} \quad (B.1)$$

For this connection:

n_{sp}	dowel rows R_i	dowel columns C_i	total n. of dowels	dowel diameter d_c	timber density ρ
8	8	4	40	12 mm	430kg/m ³

$$K_{ser,dowel} = 7.44 * 10^4 N/mm$$

$$K_{ser,connection} = 7.44 * 10^4 * 40 = 2.98 * 10^4 N/mm$$

the rotational stiffness of a joint can be calculated by the following formula:

$$K_{ser,\theta} = K_{ser,dowel} * \sum r_i^2 \quad (B.2)$$

Where,

1. K_{ser} is the slip modulus referred in the previous segment

2. r_i is the polar distance, namely the radius vector between an individual dowel and the geometric center of the dowel group.

The polar distance is calculated from the centre of the connection;

	C1	C2	C3	C4	C5	C6	C7	C8
R1	145726	85726	45726	25726	25726	45726	85726	145726
R2	128306	68306	28306	8306	8306	28306	68306	128306
R3	122500	62500	22500	2500	2500	22500	62500	122500
R4	128306	68306	28306	8306	8306	28306	68306	128306
R5	145726	85726	45726	25726	25726	45726	85726	145726

$$K_{ser,\theta} = K_{ser,dowel} * \sum r_i^2 = 1.91 * 10^{11} N * mm/rad$$

SideDiag-OuterColumns

The stiffness module for a connection is found in chapter 7 in *EC5 – 1*.

For a connection with steel or concrete, only the timber will deform, thus the stiffness can be doubled according to *EC1 – 4*, 7.1(3).

This connection has

$$K_{ser,dowel} = 2 * n_{sp} * \rho^{1.5} * \frac{d_c}{23} \tag{B.3}$$

For this connection:

n_{sp}	dowel rows R_i	dowel columns C_i	total n. of dowels	dowel diameter d_c	timber density ρ
8	9	9	81	12 mm	430kg/m ³

$$K_{ser,dowel} = 7.44 * 10^4 N/mm$$

$$K_{ser,connection} = 7.44 * 10^4 * 81 = 6,03 * 10^6 N/mm$$

the rotational stiffness of a joint can be calculated by the following formula:

$$K_{ser,\theta} = K_{ser,dowel} * \sum r_i^2 \tag{B.4}$$

Where,

1. K_{ser} is the slip modulus referred in the previous segment
2. r_i is the polar distance, namely the radius vector between an individual dowel and the geometric center of the dowel group.

The polar distance is calculated from the centre of the connection;

	C1	C2	C3	C4	C5	C6	C7	C8	C9
R1	478096	408096	358096	328096	318096	328096	358096	408096	478096
R2	338929	268929	218929	188929	178929	188929	218929	268929	338929
R3	239524	169524	119524	89524	79524	89524	119524	169524	239524
R4	179881	109881	59881	29881	19881	29881	59881	109881	179881
R5	160000	90000	40000	10000	0	10000	40000	90000	160000
R6	179881	109881	59881	29881	19881	29881	59881	109881	179881
R7	239524	169524	119524	89524	79524	89524	119524	169524	239524
R8	338929	268929	218929	188929	178929	188929	218929	268929	338929
R9	478096	408096	358096	328096	318096	328096	358096	408096	478096

$$K_{ser,\theta} = K_{ser,dowel} * \sum r_i^2 = 1.20 * 10^{12} N * mm/rad$$

SideDiag-InnerBeams

The stiffness module for a connection is found in chapter 7 in *EC5 – 1*.

For a connection with steel or concrete, only the timber will deform, thus the stiffness can be doubled according to *EC1 – 4*, 7.1(3).

This connection has

$$K_{ser,dowel} = 2 * n_{sp} * \rho^{1.5} * \frac{d_c}{23} \tag{B.5}$$

For this connection:

n_{sp}	dowel rows R_i	dowel columns C_i	total n. of dowels	dowel diameter d_c	timber density ρ
8	2	5	10	12 mm	430kg/m ³

$$K_{ser,dowel} = 7.44 * 10^4 N/mm$$

$$K_{ser,connection} = 7.44 * 10^4 * 10 = 7.44 * 10^5 N/mm$$

the rotational stiffness of a joint can be calculated by the following formula:

$$K_{ser,\theta} = K_{ser,dowel} * \sum r_i^2 \tag{B.6}$$

Where,

1. K_{ser} is the slip modulus referred in the previous segment
2. r_i is the polar distance, namely the radius vector between an individual dowel and the geometric center of the dowel group.

The polar distance is calculated from the centre of the connection;

	C1	C2
R1	26711	26711
R2	8553	8553
R3	2500	2500
R4	8553	8553
R5	26711	26711

$$K_{ser,\theta} = K_{ser,dowel} * \sum r_i^2 = 1.09 * 10^{12} N * mm/rad$$

FrontDiag-FrontBeams

BackDiag-BackBeams

The stiffness module for a connection is found in chapter 7 in *EC5 – 1*.

For a connection with steel or concrete, only the timber will deform, thus the stiffness can be doubled according to *EC1 – 4*, 7.1(3).

This connection has

$$K_{ser,dowel} = 2 * n_{sp} * \rho^{1.5} * \frac{d_c}{23} \tag{B.7}$$

For this connection:

n_{sp}	dowel rows R_i	dowel columns C_i	total n. of dowels	dowel diameter d_c	timber density ρ
4	4	3	12	12 mm	430kg/m ³

$$K_{ser,dowel} = 3.72 * 10^4 N/mm$$

$$K_{ser,connection} = 7.44 * 10^4 * 10 = 4.47 * 10^5 N/mm$$

the rotational stiffness of a joint can be calculated by the following formula:

$$K_{ser,\theta} = K_{ser,dowel} * \sum r_i^2 \quad (B.8)$$

Where,

1. K_{ser} is the slip modulus referred in the previous segment
2. r_i is the polar distance, namely the radius vector between an individual dowel and the geometric center of the dowel group.

The polar distance is calculated from the centre of the connection;

	C1	C2	C3	C4
R1	19786	12586	12586	19786
R2	8100	900	900	8100
R3	19786	12586	12586	19786

$$K_{ser,\theta} = K_{ser,dowel} * \sum r_i^2 = 5.49 * 10^9 N * mm/rad$$

FacadeBeams-OuterColumns

The stiffness module for a connection is found in chapter 7 in *EC5 – 1*.

For a connection with steel or concrete, only the timber will deform, thus the stiffness can be doubled according to *EC1 – 4*, 7.1(3).

This connection has

$$K_{ser,dowel} = 2 * n_{sp} * \rho^{1.5} * \frac{d_c}{23} \quad (B.9)$$

For this connection:

n_{sp}	dowel rows R_i	dowel columns C_i	total n. of dowels	dowel diameter d_c	timber density ρ
4	4	3	12	12 mm	430kg/m ³

$$K_{ser,dowel} = 3.72 * 10^4 N/mm$$

$$K_{ser,connection} = 4.47 * 10^5 N/mm$$

the rotational stiffness of a joint can be calculated by the following formula:

$$K_{ser,\theta} = K_{ser,dowel} * \sum r_i^2 \quad (B.10)$$

Where,

1. K_{ser} is the slip modulus referred in the previous segment
2. r_i is the polar distance, namely the radius vector between an individual dowel and the geometric center of the dowel group.

The polar distance is calculated from the centre of the connection;

	C1	C2	C3	C4
R1	11125	3925	3925	11125
R2	8100	900	900	8100
R3	11125	3925	3925	11125

$$K_{ser,\theta} = K_{ser,dowel} * \sum r_i^2 = 2.91 * 10^9 N * mm/rad$$

InnerBeams-InnerColumns

The stiffness module for a connection is found in chapter 7 in *EC5* – 1.

For a connection with steel or concrete, only the timber will deform, thus the stiffness can be doubled according to *EC1* – 4, 7.1(3).

This connection has

$$K_{ser,dowel} = 2 * n_{sp} * \rho^{1.5} * \frac{d_c}{23} \quad (B.11)$$

For this connection:

n_{sp}	dowel rows R_i	dowel columns C_i	total n. of dowels	dowel diameter d_c	timber density ρ
2+2	2+2	6+6	12+12	12 mm	430kg/m ³

$$K_{ser,dowel} = 3.72 * 10^4 N/mm$$

$$K_{ser,connection} = 8.93 * 10^5 N/mm$$

the rotational stiffness of a joint can be calculated by the following formula:

$$K_{ser,\theta} = K_{ser,dowel} * \sum r_i^2 \tag{B.12}$$

Where,

1. K_{ser} is the slip modulus referred in the previous segment
2. r_i is the polar distance, namely the radius vector between an individual dowel and the geometric center of the dowel group.

The polar distance is calculated from the centre of the connection;

	C1	C2
R1	31850	31850
R2	12250	12250
R3	2450	2450
R4	2450	2450
R5	12250	12250
R6	31850	31850

$$K_{ser,\theta} = K_{ser,dowel} * \sum r_i^2 = 1.39 * 10^{10} N * mm/rad$$

InnerBeams-OuterColumns

The stiffness module for a connection is found in chapter 7 in EC5 – 1.

For a connection with steel or concrete, only the timber will deform, thus the stiffness can

be doubled according to *EC1 – 4, 7.1(3)*.

This connection has

$$K_{ser,dowel} = 2 * n_{sp} * \rho^{1.5} * \frac{d_c}{23} \tag{B.13}$$

For this connection:

n_{sp}	dowel rows R_i	dowel columns C_i	total n. of dowels	dowel diameter d_c	timber density ρ
4	4	7	28	12 mm	430kg/m ³

$$K_{ser,dowel} = 3.72 * 10^4 N/mm$$

$$K_{ser,connection} = 1.04 * 10^6 N/mm$$

the rotational stiffness of a joint can be calculated by the following formula:

$$K_{ser,\theta} = K_{ser,dowel} * \sum r_i^2 \tag{B.14}$$

Where,

1. K_{ser} is the slip modulus referred in the previous segment
2. r_i is the polar distance, namely the radius vector between an individual dowel and the geometric center of the dowel group.

The polar distance is calculated from the centre of the connection;

	C1	C2	C3	C4
R1	82125	48325	48325	82125
R2	57625	23825	23825	57625
R3	42925	9125	9125	42925
R4	38025	4225	4225	38025
R5	42925	9125	9125	42925
R6	57625	23825	23825	57625
R7	82125	48325	48325	82125

$$K_{ser,\theta} = K_{ser,dowel} * \sum r_i^2 = 4.24 * 10^{10} N * mm/rad$$

FacadeBeams-FrontColumns**BackBeams-BackColumns**

The stiffness module for a connection is found in chapter 7 in *EC5 – 1*.

For a connection with steel or concrete, only the timber will deform, thus the stiffness can be doubled according to *EC1 – 4*, 7.1(3).

This connection has

$$K_{ser,dowel} = 2 * n_{sp} * \rho^{1.5} * \frac{d_c}{23} \quad (\text{B.15})$$

For this connection:

n_{sp}	dowel rows R_i	dowel columns C_i	total n. of dowels	dowel diameter d_c	timber density ρ
4+4	4+4	3+3	12+12	12 mm	430kg/m ³

$$K_{ser,dowel} = 3.72 * 10^4 N/mm$$

$$K_{ser,connection} = 8.93 * 10^5 N/mm$$

the rotational stiffness of a joint can be calculated by the following formula:

$$K_{ser,\theta} = K_{ser,dowel} * \sum r_i^2 \quad (\text{B.16})$$

Where,

1. K_{ser} is the slip modulus referred in the previous segment
2. r_i is the polar distance, namely the radius vector between an individual dowel and the geometric center of the dowel group.

The polar distance is calculated from the centre of the connection;

	C1	C2	C3	C4
R1	11125	3925	3925	11125
R2	8100	900	900	8100
R3	11125	3925	3925	11125

$$K_{ser,\theta} = K_{ser,dowel} * \sum r_i^2 = 5.82 * 10^9 N * mm/rad$$

Foundation-OuterColumns

The stiffness module for a connection is found in chapter 7 in *EC5 – 1*.

For a connection with steel or concrete, only the timber will deform, thus the stiffness can be doubled according to *EC1 – 4*, 7.1(3).

This connection has

$$K_{ser,dowel} = 2 * n_{sp} * \rho^{1.5} * \frac{d_c}{23} \quad (B.17)$$

For this connection:

n_{sp}	dowel rows R_i	dowel columns C_i	total n. of dowels	dowel diameter d_c	timber density ρ
8	10	10	100	12 mm	430kg/m ³

$$K_{ser,dowel} = 7.44^4 N/mm$$

$$K_{ser,connection} = 7.44 * 10^6 N/mm$$

the rotational stiffness of a joint can be calculated by the following formula:

$$K_{ser,\theta} = K_{ser,dowel} * \sum r_i^2 \quad (B.18)$$

Where,

1. K_{ser} is the slip modulus referred in the previous segment
2. r_i is the polar distance, namely the radius vector between an individual dowel and the geometric center of the dowel group.

The polar distance is calculated from the centre of the connection;

$$K_{ser,\theta} = K_{ser,dowel} * \sum r_i^2 = 1.06 * 10^{12} N * mm/rad$$

	C1	C2	C3	C4	C5	C6	C7	C8	C9
R1	348806	291006	247656	218756	204306	204306	218756	247656	291006
R2	268806	211006	167656	138756	124306	124306	138756	167656	211006
R3	208806	151006	107656	78756	64306	64306	78756	107656	151006
R4	168806	111006	67656	38756	24306	24306	38756	67656	111006
R5	148806	91006	47656	18756	4306	4306	18756	47656	91006
R6	148806	91006	47656	18756	4306	4306	18756	47656	91006
R7	168806	111006	67656	38756	24306	24306	38756	67656	111006
R8	208806	151006	107656	78756	64306	64306	78756	107656	151006
R9	268806	211006	167656	138756	124306	124306	138756	167656	211006
R10	348806	291006	247656	218756	204306	204306	218756	247656	291006

Foundation-InnerColumns

The stiffness module for a connection is found in chapter 7 in *EC5 – 1*.

For a connection with steel or concrete, only the timber will deform, thus the stiffness can be doubled according to *EC1 – 4*, 7.1(3).

This connection has

$$K_{ser,dowel} = 2 * n_{sp} * \rho^{1.5} * \frac{d_c}{23} \tag{B.19}$$

For this connection:

n_{sp}	dowel rows R_i	dowel columns C_i	total n. of dowels	dowel diameter d_c	timber density ρ
8	5	1	5	12 mm	430kg/m ³

$$K_{ser,dowel} = 7.44^4 N/mm$$

$$K_{ser,connection} = 3.72 * 10^5 N/mm$$

the rotational stiffness of a joint can be calculated by the following formula:

$$K_{ser,\theta} = K_{ser,dowel} * \sum r_i^2 \tag{B.20}$$

Where,

1. K_{ser} is the slip modulus referred in the previous segment
2. r_i is the polar distance, namely the radius vector between an individual dowel and the geometric center of the dowel group.

The polar distance is calculated from the centre of the connection;

	C1	C2	C3	C4	C5
R1	10000	2500	0	2500	10000

$$K_{ser,\theta} = K_{ser,dowel} * \sum r_i^2 = 1.86 * 10^9 N * mm/rad$$

Foundation-FrontColumns

Foundation-BackColumns

The stiffness module for a connection is found in chapter 7 in *EC5 – 1*.

For a connection with steel or concrete, only the timber will deform, thus the stiffness can be doubled according to *EC1 – 4*, 7.1(3).

This connection has

$$K_{ser,dowel} = 2 * n_{sp} * \rho^{1.5} * \frac{d_c}{23} \quad (B.21)$$

For this connection:

n_{sp}	dowel rows R_i	dowel columns C_i	total n. of dowels	dowel diameter d_c	timber density ρ
8	8	2	16	12 mm	430kg/m ³

$$K_{ser,dowel} = 7.44^4 N/mm$$

$$K_{ser,connection} = 3.72 * 10^5 N/mm$$

the rotational stiffness of a joint can be calculated by the following formula:

$$K_{ser,\theta} = K_{ser,dowel} * \sum r_i^2 \quad (B.22)$$

Where,

1. K_{ser} is the slip modulus referred in the previous segment
2. r_i is the polar distance, namely the radius vector between an individual dowel and the geometric center of the dowel group.

The polar distance is calculated from the centre of the connection;

	C1	C2	C3	C4	C5	C6	C7	C8
R1	33125	18125	8125	3125	3125	8125	18125	33125
R2	33125	18125	8125	3125	3125	8125	18125	33125

$$K_{ser,\theta} = K_{ser,dowel} * \sum r_i^2 = 1.86 * 10^9 N * mm/rad$$

Appendix C

SSI

C.1 Kinematic Interaction

$$k_x \simeq \delta * E_s \quad (C.1)$$

Reference	δ coefficient
Vesic 1961	$\frac{0.65}{1-\nu_s} * \left(\frac{E_s * D^4}{E_p * I_p}\right)^{1/12}$
Dobry et al. 1982	$1.67 * \left(\frac{E_p}{E_s}\right)^{-0.053}$
Gazetas and Dobry 1984	FIG. 7.—Coefficient of δ <i>diagram</i> [86]
Gazetas and Makris 1992	1.2
Kavvadas and Gazetas 1993 (homogeneous soil)	$\frac{3}{1-\nu_s^2} * \left(\frac{E_s}{E_p}\right)^{1/8} * \left(\frac{L}{D}\right)^{1/8}$
Kavvadas and Gazetas 1993 (2 layers soil)	$\frac{2}{1-\nu_s^2} * \left(\frac{E_{s0} * D^4}{E_p * I_p}\right)^{1/8} * \left(\frac{L}{D}\right)^{1/8} * \left(\frac{H_a}{H_b}\right)^{1/12} * \left(\frac{V_{sa}}{V_{sb}}\right)^{1/15}$
Syngros 2004 (homogeneous soil, fixed pile)	$2 * \left(\frac{E_p}{E_s}\right)^{-0.075}$

C.2 Group pile dynamic Impedance matrices

C.2.1 Monopile simplified dynamic impedance matrix

General Single Pile Stiffness [K11] MN/m						
	Kv[1]	0	0	=	0,00	0,00
K[11]dyn	0	Khh[1]	Khm[1]	=	0,00	808,78781118286-3,43349345162784i
	0	Kmh[1]	Kmm[1]	=	0,00	1345,96158857224-3,80926848252556i
	Kv[1]	-			0	-
	Khh[1]	$4EI\lambda^3$			Khm[1]	$2EI\lambda^2$
	Kmm[1]	$2EI\lambda$			0	-
$S_{ij}=K_{ij}+i*\omega*C_{ij}$						
Step2a- K[11] Method, May be used only if $L_a < L_p$						
Active Lgth	$L_a = 1.5*(E_p/E_s)^{0.25}*D_p =$		12,6527	TRUE		
	$L_a = 15*D_p =$		22,5	TRUE		
Wpile	$m = A_p*\rho_p =$		4,41786	tn/m		
Inertia_pile	$I_p = \pi/4*R^4 =$		0,2485	m4/m		
Pile_elastic	$E_p = C30 =$		30000	Mpa		
RadiationVel	$V_{la} = 3.4*V_s/\pi*(1-\nu) =$		360,751	m/s		
Spring stiffness	$k_x = 1.2*E_s$		268800	KN/m^2		268,8 MN/m^2
Dashpot damping	$C_x = 2*ac^{(-0.25)}*\rho_s*V_s*D[1+(V_{la}/V_s)^{1.25}] + 2*\beta_s*k_x/\epsilon =$					10,10708537 MN*s/m^2
Prmt λ	$\lambda = [(k_x + i*\omega*C_x - m*\omega^2)/(4*E_p*I_p)]^{1/4} =$			Re		Im
					0,008148722	-4,61245E-05
				=Re(λ)=	0,300451015	
				=Im(λ)=	-0,000425159	
				=Re(λ^3)=	0,027121794	
				=Im(λ^3)=	-0,000115138	
				=Re(λ^2)=	0,090270632	
				=Im(λ^2)=	-0,000255479	

C.2.2 Pile distance matrix and ψ motion matrix

S	1	2	3	4	5	6	7	8	9	10	11	12	13	14
0	5	10	15	20	5	5	5	5	5	10	10	10	10	
5	0	5	10	15	5	5	5	5	5	10	10	10	10	
10	5	0	5	10	5	5	5	5	5	10	10	10	10	
15	10	5	0	5	5	5	5	5	5	10	10	10	10	
20	15	10	5	0	5	5	5	5	5	10	10	10	10	
5	5	5	5	5	0	5	10	15	20	5	5	5	5	
5	5	5	5	5	5	0	5	10	15	5	5	5	5	
5	5	5	5	5	10	5	0	5	10	5	5	5	5	
5	5	5	5	5	15	10	5	0	5	5	5	5	5	
5	5	5	5	5	20	15	10	5	0	5	5	5	5	
10	10	10	10	10	5	5	5	5	5	0	5	10	15	
10	10	10	10	10	5	5	5	5	5	5	0	5	10	
10	10	10	10	10	5	5	5	5	5	10	5	0	5	
10	10	10	10	10	5	5	5	5	5	15	10	5	0	
10	10	10	10	10	5	5	5	5	5	20	15	15	5	

$\psi(r,\theta)=(s,\pi/2)$	1	2	3	4	5	6	7	8	9	10	11	12	13
1	0	397-0,019	996-0,030	088-0,037	806-0,044	397-0,019	397-0,019	397-0,019	397-0,019	397-0,019	996-0,030	996-0,030	996-0,030
2	397-0,019	0	397-0,019	996-0,030	088-0,037	397-0,019	397-0,019	397-0,019	397-0,019	397-0,019	996-0,030	996-0,030	996-0,030
3	996-0,030	397-0,019	0	397-0,019	996-0,030	397-0,019	397-0,019	397-0,019	397-0,019	397-0,019	996-0,030	996-0,030	996-0,030
4	088-0,037	996-0,030	397-0,019	0	397-0,019	397-0,019	397-0,019	397-0,019	397-0,019	397-0,019	996-0,030	996-0,030	996-0,030
5	806-0,044	088-0,037	996-0,030	397-0,019	0	397-0,019	397-0,019	397-0,019	397-0,019	397-0,019	996-0,030	996-0,030	996-0,030
6	397-0,019	397-0,019	397-0,019	397-0,019	397-0,019	0	397-0,019	996-0,030	088-0,037	806-0,044	397-0,019	397-0,019	397-0,019
7	397-0,019	397-0,019	397-0,019	397-0,019	397-0,019	397-0,019	0	397-0,019	996-0,030	088-0,037	397-0,019	397-0,019	397-0,019
8	397-0,019	397-0,019	397-0,019	397-0,019	397-0,019	996-0,030	397-0,019	0	397-0,019	996-0,030	397-0,019	397-0,019	397-0,019
9	397-0,019	397-0,019	397-0,019	397-0,019	397-0,019	088-0,037	996-0,030	397-0,019	0	397-0,019	397-0,019	397-0,019	397-0,019
10	397-0,019	397-0,019	397-0,019	397-0,019	397-0,019	806-0,044	088-0,037	996-0,030	397-0,019	0	397-0,019	397-0,019	397-0,019
11	996-0,030	996-0,030	996-0,030	996-0,030	996-0,030	397-0,019	397-0,019	397-0,019	397-0,019	397-0,019	0	397-0,019	996-0,030
12	996-0,030	996-0,030	996-0,030	996-0,030	996-0,030	397-0,019	397-0,019	397-0,019	397-0,019	397-0,019	397-0,019	0	397-0,019
13	996-0,030	996-0,030	996-0,030	996-0,030	996-0,030	397-0,019	397-0,019	397-0,019	397-0,019	397-0,019	996-0,030	397-0,019	0
14	996-0,030	996-0,030	996-0,030	996-0,030	996-0,030	397-0,019	397-0,019	397-0,019	397-0,019	397-0,019	088-0,037	996-0,030	397-0,019
15	996-0,030	996-0,030	996-0,030	996-0,030	996-0,030	397-0,019	397-0,019	397-0,019	397-0,019	397-0,019	806-0,044	088-0,037	088-0,037

C.2.3 ϵ_{xx} coefficient matrix

Khh		$\Sigma\Sigma=$ 72,8739118219649 4,91341664266619i												
aup= 0,75														
	1	2	3	4	5	6	7	8	9	10	11	12	13	
1	1	994-0,019	892-0,027	135-0,033	146-0,038	994-0,019	994-0,019	994-0,019	994-0,019	994-0,019	892-0,027	892-0,027	892-0,027	
2	994-0,019	1	994-0,019	892-0,027	135-0,033	994-0,019	994-0,019	994-0,019	994-0,019	994-0,019	892-0,027	892-0,027	892-0,027	
3	892-0,027	994-0,019	1	994-0,019	892-0,027	994-0,019	994-0,019	994-0,019	994-0,019	994-0,019	892-0,027	892-0,027	892-0,027	
4	135-0,033	892-0,027	994-0,019	1	994-0,019	994-0,019	994-0,019	994-0,019	994-0,019	994-0,019	892-0,027	892-0,027	892-0,027	
5	146-0,038	135-0,033	892-0,027	994-0,019	1	994-0,019	994-0,019	994-0,019	994-0,019	994-0,019	892-0,027	892-0,027	892-0,027	
6	994-0,019	994-0,019	994-0,019	994-0,019	994-0,019	1	994-0,019	892-0,027	135-0,033	146-0,038	994-0,019	994-0,019	994-0,019	
7	994-0,019	994-0,019	994-0,019	994-0,019	994-0,019	994-0,019	1	994-0,019	892-0,027	135-0,033	994-0,019	994-0,019	994-0,019	
8	994-0,019	994-0,019	994-0,019	994-0,019	994-0,019	892-0,027	994-0,019	1	994-0,019	892-0,027	994-0,019	994-0,019	994-0,019	
9	994-0,019	994-0,019	994-0,019	994-0,019	994-0,019	135-0,033	892-0,027	994-0,019	1	994-0,019	994-0,019	994-0,019	994-0,019	
10	994-0,019	994-0,019	994-0,019	994-0,019	994-0,019	146-0,038	135-0,033	892-0,027	994-0,019	1	994-0,019	994-0,019	994-0,019	
11	892-0,027	892-0,027	892-0,027	892-0,027	892-0,027	994-0,019	994-0,019	994-0,019	994-0,019	994-0,019	1	994-0,019	892-0,027	
12	892-0,027	892-0,027	892-0,027	892-0,027	892-0,027	994-0,019	994-0,019	994-0,019	994-0,019	994-0,019	994-0,019	1	994-0,019	
13	892-0,027	892-0,027	892-0,027	892-0,027	892-0,027	994-0,019	994-0,019	994-0,019	994-0,019	994-0,019	892-0,027	994-0,019	1	
14	892-0,027	892-0,027	892-0,027	892-0,027	892-0,027	994-0,019	994-0,019	994-0,019	994-0,019	994-0,019	135-0,033	892-0,027	994-0,019	
15	892-0,027	892-0,027	892-0,027	892-0,027	892-0,027	994-0,019	994-0,019	994-0,019	994-0,019	994-0,019	146-0,038	135-0,033	135-0,033	

Real														
	1	2	3	4	5	6	7	8	9	10	11	12	13	14
1	1	0,3196	0,22407	0,18073	0,15403	0,3196	0,3196	0,3196	0,3196	0,3196	0,22407	0,22407	0,22407	0,22407
2	0,32	1	0,3196	0,22407	0,18073	0,3196	0,3196	0,3196	0,3196	0,3196	0,22407	0,22407	0,22407	0,22407
3	0,22	0,3196	1	0,3196	0,22407	0,3196	0,3196	0,3196	0,3196	0,3196	0,22407	0,22407	0,22407	0,22407
4	0,18	0,22407	0,3196	1	0,3196	0,3196	0,3196	0,3196	0,3196	0,3196	0,22407	0,22407	0,22407	0,22407
5	0,15	0,18073	0,22407	0,3196	1	0,3196	0,3196	0,3196	0,3196	0,3196	0,22407	0,22407	0,22407	0,22407
6	0,32	0,3196	0,3196	0,3196	0,3196	1	0,3196	0,22407	0,18073	0,15403	0,3196	0,3196	0,3196	0,3196
7	0,32	0,3196	0,3196	0,3196	0,3196	0,3196	1	0,3196	0,22407	0,18073	0,3196	0,3196	0,3196	0,3196
8	0,32	0,3196	0,3196	0,3196	0,3196	0,22407	0,3196	1	0,3196	0,22407	0,3196	0,3196	0,3196	0,3196
9	0,32	0,3196	0,3196	0,3196	0,3196	0,18073	0,22407	0,3196	1	0,3196	0,3196	0,3196	0,3196	0,3196
10	0,32	0,3196	0,3196	0,3196	0,3196	0,15403	0,18073	0,22407	0,3196	1	0,3196	0,3196	0,3196	0,3196
11	0,22	0,22407	0,22407	0,22407	0,22407	0,3196	0,3196	0,3196	0,3196	0,3196	1	0,3196	0,22407	0,18073
12	0,22	0,22407	0,22407	0,22407	0,22407	0,3196	0,3196	0,3196	0,3196	0,3196	0,3196	1	0,3196	0,22407
13	0,22	0,22407	0,22407	0,22407	0,22407	0,3196	0,3196	0,3196	0,3196	0,3196	0,22407	0,3196	1	0,3196
14	0,22	0,22407	0,22407	0,22407	0,22407	0,3196	0,3196	0,3196	0,3196	0,3196	0,18073	0,22407	0,3196	1
15	0,22	0,22407	0,22407	0,22407	0,22407	0,3196	0,3196	0,3196	0,3196	0,3196	0,15403	0,18073	0,18073	0,3196

Im														
	1	2	3	4	5	6	7	8	9	10	11	12	13	14
1	0	-0,0195	-0,0273	-0,0332	-0,038	-0,0195	-0,0195	-0,0195	-0,0195	-0,0195	-0,0273	-0,0273	-0,0273	-0,0273
2	-0,02	0	-0,0195	-0,0273	-0,0332	-0,0195	-0,0195	-0,0195	-0,0195	-0,0195	-0,0273	-0,0273	-0,0273	-0,0273
3	-0,03	-0,0195	0	-0,0195	-0,0273	-0,0195	-0,0195	-0,0195	-0,0195	-0,0195	-0,0273	-0,0273	-0,0273	-0,0273
4	-0,03	-0,0273	-0,0195	0	-0,0195	-0,0195	-0,0195	-0,0195	-0,0195	-0,0195	-0,0273	-0,0273	-0,0273	-0,0273
5	-0,04	-0,0332	-0,0273	-0,0195	0	-0,0195	-0,0195	-0,0195	-0,0195	-0,0195	-0,0273	-0,0273	-0,0273	-0,0273
6	-0,02	-0,0195	-0,0195	-0,0195	-0,0195	0	-0,0195	-0,0273	-0,0332	-0,038	-0,0195	-0,0195	-0,0195	-0,0195
7	-0,02	-0,0195	-0,0195	-0,0195	-0,0195	-0,0195	0	-0,0195	-0,0273	-0,0332	-0,0195	-0,0195	-0,0195	-0,0195
8	-0,02	-0,0195	-0,0195	-0,0195	-0,0195	-0,0273	-0,0195	0	-0,0195	-0,0273	-0,0195	-0,0195	-0,0195	-0,0195
9	-0,02	-0,0195	-0,0195	-0,0195	-0,0195	-0,0332	-0,0273	-0,0195	0	-0,0195	-0,0195	-0,0195	-0,0195	-0,0195
10	-0,02	-0,0195	-0,0195	-0,0195	-0,0195	-0,038	-0,0332	-0,0273	-0,0195	0	-0,0195	-0,0195	-0,0195	-0,0195
11	-0,03	-0,0273	-0,0273	-0,0273	-0,0273	-0,0195	-0,0195	-0,0195	-0,0195	-0,0195	0	-0,0195	-0,0273	-0,0332
12	-0,03	-0,0273	-0,0273	-0,0273	-0,0273	-0,0195	-0,0195	-0,0195	-0,0195	-0,0195	-0,0195	0	-0,0195	-0,0273
13	-0,03	-0,0273	-0,0273	-0,0273	-0,0273	-0,0195	-0,0195	-0,0195	-0,0195	-0,0195	-0,0273	-0,0195	0	-0,0195
14	-0,03	-0,0273	-0,0273	-0,0273	-0,0273	-0,0195	-0,0195	-0,0195	-0,0195	-0,0195	-0,0332	-0,0273	-0,0195	0
15	-0,03	-0,0273	-0,0273	-0,0273	-0,0273	-0,0195	-0,0195	-0,0195	-0,0195	-0,0195	-0,038	-0,0332	-0,0332	-0,0195

C.2.4 ϵ_{xy} coefficient matrix

Khm		$\Sigma\Sigma=$ 66,4434771750801-4,36748146014771i												
aum=afp 0,66667		1	2	3	4	5	6	7	8	9	10	11	12	13
1	1	217-0,017	793-0,024	231-0,029	907-0,033	217-0,017	217-0,017	217-0,017	217-0,017	217-0,017	793-0,024	793-0,024	793-0,024	793-0,024
2	217-0,017	1	217-0,017	793-0,024	231-0,029	217-0,017	217-0,017	217-0,017	217-0,017	217-0,017	793-0,024	793-0,024	793-0,024	793-0,024
3	793-0,024	217-0,017	1	217-0,017	793-0,024	217-0,017	217-0,017	217-0,017	217-0,017	217-0,017	793-0,024	793-0,024	793-0,024	793-0,024
4	231-0,029	793-0,024	217-0,017	1	217-0,017	217-0,017	217-0,017	217-0,017	217-0,017	217-0,017	793-0,024	793-0,024	793-0,024	793-0,024
5	907-0,033	231-0,029	793-0,024	217-0,017	1	217-0,017	217-0,017	217-0,017	217-0,017	217-0,017	793-0,024	793-0,024	793-0,024	793-0,024
6	217-0,017	217-0,017	217-0,017	217-0,017	217-0,017	1	217-0,017	793-0,024	231-0,029	907-0,033	217-0,017	217-0,017	217-0,017	217-0,017
7	217-0,017	217-0,017	217-0,017	217-0,017	217-0,017	217-0,017	1	217-0,017	793-0,024	231-0,029	217-0,017	217-0,017	217-0,017	217-0,017
8	217-0,017	217-0,017	217-0,017	217-0,017	217-0,017	793-0,024	217-0,017	1	217-0,017	793-0,024	217-0,017	217-0,017	217-0,017	217-0,017
9	217-0,017	217-0,017	217-0,017	217-0,017	217-0,017	231-0,029	793-0,024	217-0,017	1	217-0,017	217-0,017	217-0,017	217-0,017	217-0,017
10	217-0,017	217-0,017	217-0,017	217-0,017	217-0,017	907-0,033	231-0,029	793-0,024	217-0,017	1	217-0,017	217-0,017	217-0,017	217-0,017
11	793-0,024	793-0,024	793-0,024	793-0,024	793-0,024	217-0,017	217-0,017	217-0,017	217-0,017	217-0,017	1	217-0,017	793-0,024	793-0,024
12	793-0,024	793-0,024	793-0,024	793-0,024	793-0,024	217-0,017	217-0,017	217-0,017	217-0,017	217-0,017	217-0,017	1	217-0,017	793-0,024
13	793-0,024	793-0,024	793-0,024	793-0,024	793-0,024	217-0,017	217-0,017	217-0,017	217-0,017	217-0,017	793-0,024	217-0,017	1	793-0,024
14	793-0,024	793-0,024	793-0,024	793-0,024	793-0,024	217-0,017	217-0,017	217-0,017	217-0,017	217-0,017	231-0,029	793-0,024	217-0,017	793-0,024
15	793-0,024	793-0,024	793-0,024	793-0,024	793-0,024	217-0,017	217-0,017	217-0,017	217-0,017	217-0,017	907-0,033	231-0,029	217-0,017	793-0,024

Real		1	2	3	4	5	6	7	8	9	10	11	12	13	14
1	1	0,28409	0,19917	0,16065	0,13691	0,28409	0,28409	0,28409	0,28409	0,28409	0,19917	0,19917	0,19917	0,19917	0,19917
2	0,28	1	0,28409	0,19917	0,16065	0,28409	0,28409	0,28409	0,28409	0,28409	0,19917	0,19917	0,19917	0,19917	0,19917
3	0,2	0,28409	1	0,28409	0,19917	0,28409	0,28409	0,28409	0,28409	0,28409	0,19917	0,19917	0,19917	0,19917	0,19917
4	0,16	0,19917	0,28409	1	0,28409	0,28409	0,28409	0,28409	0,28409	0,28409	0,19917	0,19917	0,19917	0,19917	0,19917
5	0,14	0,16065	0,19917	0,28409	1	0,28409	0,28409	0,28409	0,28409	0,28409	0,19917	0,19917	0,19917	0,19917	0,19917
6	0,28	0,28409	0,28409	0,28409	0,28409	1	0,28409	0,19917	0,16065	0,13691	0,28409	0,28409	0,28409	0,28409	0,28409
7	0,28	0,28409	0,28409	0,28409	0,28409	0,28409	1	0,28409	0,19917	0,16065	0,28409	0,28409	0,28409	0,28409	0,28409
8	0,28	0,28409	0,28409	0,28409	0,28409	0,19917	0,28409	1	0,28409	0,19917	0,28409	0,28409	0,28409	0,28409	0,28409
9	0,28	0,28409	0,28409	0,28409	0,28409	0,16065	0,19917	0,28409	1	0,28409	0,28409	0,28409	0,28409	0,28409	0,28409
10	0,28	0,28409	0,28409	0,28409	0,28409	0,13691	0,16065	0,19917	0,28409	1	0,28409	0,28409	0,28409	0,28409	0,28409
11	0,2	0,19917	0,19917	0,19917	0,19917	0,28409	0,28409	0,28409	0,28409	0,28409	1	0,28409	0,19917	0,16065	0,19917
12	0,2	0,19917	0,19917	0,19917	0,19917	0,28409	0,28409	0,28409	0,28409	0,28409	0,28409	1	0,28409	0,19917	0,19917
13	0,2	0,19917	0,19917	0,19917	0,19917	0,28409	0,28409	0,28409	0,28409	0,28409	0,19917	0,28409	1	0,28409	0,28409
14	0,2	0,19917	0,19917	0,19917	0,19917	0,28409	0,28409	0,28409	0,28409	0,28409	0,16065	0,19917	0,28409	1	0,28409
15	0,2	0,19917	0,19917	0,19917	0,19917	0,28409	0,28409	0,28409	0,28409	0,28409	0,13691	0,16065	0,16065	0,28409	0,28409
Im		1	2	3	4	5	6	7	8	9	10	11	12	13	14
1	0	-0,0173	-0,0243	-0,0295	-0,0338	-0,0173	-0,0173	-0,0173	-0,0173	-0,0173	-0,0243	-0,0243	-0,0243	-0,0243	-0,0243
2	-0,02	0	-0,0173	-0,0243	-0,0295	-0,0173	-0,0173	-0,0173	-0,0173	-0,0173	-0,0243	-0,0243	-0,0243	-0,0243	-0,0243
3	-0,02	-0,0173	0	-0,0173	-0,0243	-0,0173	-0,0173	-0,0173	-0,0173	-0,0173	-0,0243	-0,0243	-0,0243	-0,0243	-0,0243
4	-0,03	-0,0243	-0,0173	0	-0,0173	-0,0173	-0,0173	-0,0173	-0,0173	-0,0173	-0,0243	-0,0243	-0,0243	-0,0243	-0,0243
5	-0,03	-0,0295	-0,0243	-0,0173	0	-0,0173	-0,0173	-0,0173	-0,0173	-0,0173	-0,0243	-0,0243	-0,0243	-0,0243	-0,0243
6	-0,02	-0,0173	-0,0173	-0,0173	-0,0173	0	-0,0173	-0,0243	-0,0295	-0,0338	-0,0173	-0,0173	-0,0173	-0,0173	-0,0173
7	-0,02	-0,0173	-0,0173	-0,0173	-0,0173	-0,0173	0	-0,0173	-0,0243	-0,0295	-0,0173	-0,0173	-0,0173	-0,0173	-0,0173
8	-0,02	-0,0173	-0,0173	-0,0173	-0,0173	-0,0243	-0,0173	0	-0,0173	-0,0243	-0,0173	-0,0173	-0,0173	-0,0173	-0,0173
9	-0,02	-0,0173	-0,0173	-0,0173	-0,0173	-0,0295	-0,0243	-0,0173	0	-0,0173	-0,0173	-0,0173	-0,0173	-0,0173	-0,0173
10	-0,02	-0,0173	-0,0173	-0,0173	-0,0173	-0,0338	-0,0295	-0,0243	-0,0173	0	-0,0173	-0,0173	-0,0173	-0,0173	-0,0173
11	-0,02	-0,0243	-0,0243	-0,0243	-0,0243	-0,0173	-0,0173	-0,0173	-0,0173	-0,0173	0	-0,0173	-0,0243	-0,0295	-0,0295
12	-0,02	-0,0243	-0,0243	-0,0243	-0,0243	-0,0173	-0,0173	-0,0173	-0,0173	-0,0173	-0,0173	0	-0,0173	-0,0243	-0,0243
13	-0,02	-0,0243	-0,0243	-0,0243	-0,0243	-0,0173	-0,0173	-0,0173	-0,0173	-0,0173	-0,0243	-0,0173	0	-0,0173	-0,0173
14	-0,02	-0,0243	-0,0243	-0,0243	-0,0243	-0,0173	-0,0173	-0,0173	-0,0173	-0,0173	-0,0295	-0,0243	-0,0173	0	-0,0173
15	-0,02	-0,0243	-0,0243	-0,0243	-0,0243	-0,0173	-0,0173	-0,0173	-0,0173	-0,0173	-0,0338	-0,0295	-0,0295	-0,0173	-0,0173

C.2.6 Group pile dynamic impedance matrix

Group Pile stiffness Matrix MN/m							
	K^G_{xx}	K^G_{xy}	K^G_{xr}		0	0	0
K^G_{dyn}	K^G_{yx}	K^G_{yy}	K^G_{yr}	=	0	58922,661450952-4224,12359088665i	89413,73117936-6131,56332763266i
	K^G_{rx}	K^G_{ry}	K^G_{rr}		0	89413,73117936-6131,56332763266i	182411,920042567-10040,8948446904i
	K^G_{xx}	$K_{xx}[11]*\sum\sum\epsilon_{xx}$			K^G_{xy}	$K_{xy}[11]*\sum\sum\epsilon_{xy}$	
	K^G_{yy}	$K_{yy}[11]*\sum\sum\epsilon_{yy}$			K^G_{yr}	$K_{yr}[11]*\sum\sum\epsilon_{yr}$	
	K^G_{rr}	$K_z[11]*\sum\sum\epsilon_{xz}$			K^G_{xr}	$K_{xr}[11]*\sum\sum\epsilon_{xr}$	

Appendix D

Turbulence calculations

D.1 First cell height inflation

Starting by calculating wind flow's Reynolds number (Re). Reynolds number will be kept stable through the all wind cases.

$$Re = \frac{\rho * U * L}{\mu} = 41134193 \quad (D.1)$$

Where the constant temperature defined in *Segregated Fluid Isothermal* under the *Physics Model* tree at 25° and,

- ρ is the density of the air at 25°, as 1.18415 kg/m³
- U is the reference velocity, V_h
- L is the characteristic length, here chosen as the width of the building $D = 35.9m$
- μ is the dynamic viscosity in regards to the reference velocity V_h , μ_h

An empirical correlation for fully developed turbulent flow over a flat plate is then used to estimate the skin friction coefficient (cf):

$$cf = [2\log_{10}(Re) - 0.65]^{-2.3} = 2,1060E - 03 \tag{D.2}$$

This particular correlation has been taken from *Schlichting*(1979) for fully turbulent flow with $Re10^9$.

Afterwards the wall shear stress (τ_w)is calculated.

$$\tau_w = \frac{1}{2} * \rho * U^2 * cf \tag{D.3}$$

The wall shear stress (τ_w) for every wind speed scenario can be seen below:

Vh_1	Vh_2	Vh_3	Vh_4	Vh_5	Vh_6
4,0177E - 01	1,6071E + 00	3,6159E + 00	6,4282E + 00	4,0177E + 01	6,2776E + 01

The friction velocity (u_τ) can then be computed from the wall shear stress (τ_w):

$$u_\tau = \sqrt{\frac{\tau_w}{\rho}} \tag{D.4}$$

The friction velocity (u_τ) for every wind speed scenario can be seen below:

Vh_1	Vh_2	Vh_3	Vh_4	Vh_5	Vh_6
0,582482537	1,164965073	1,74744761	2,329930146	5,824825366	7,281031707

The formula of $y+$ can be rearranged to give the height of the wall adjacent cell centroid from the wall (y_p), which is the half of the total height of the cell (y_h). The target value of $y+$ is set as 50.

$$y_h = 2 * \frac{y^+ \mu}{u_\tau * \rho} = 2,6895E - 03 \tag{D.5}$$

D.2 Inlet turbulent conditions

The turbulent kinetic energy (k) is correlated with the turbulence intensity (I) and the inlet velocity (U):

$$k = \frac{3}{2} * U^2 * I^2 \quad (\text{D.6})$$

The turbulence intensity (I) value equals to 4.1900902 % .

Using the turbulent length-scale or the reference length ($L = D = 35.9m$), the turbulent dissipation rate (ϵ) is being calculated next.

$$\epsilon = C\mu * \frac{k^{3/2}}{D} \quad (\text{D.7})$$

Afterwards, the specific dissipation rate (ω) will be calculated. $C\mu = 0.09$ is the model coefficient of the *SSTKO* model.

$$\omega = \frac{\epsilon}{C\mu * k} \quad (\text{D.8})$$

Reference Velocity, V_h (m/s)	TKE k	ϵ	ω
Vh_1	0.849	0.00196	0.0257
Vh_2	3.4	0.0157	0.0513
Vh_3	7.64	0.0529	0.077
Vh_4	13.6	0.125	0.103
Vh_5	84.9	1.96	0.257
Vh_6	133	3.83	0.321

Bibliography

- [1] C. Bob, T. Dencsak, and L. Bob, *Sustainability of buildings*, (2021).
- [2] N. Hume, *Lumber party: economic bounce fuels US wood price rally*, Financial Times (2021).
- [3] N. L. Cruz H., Jones D., *Materials for Construction and Civil Engineering*, (2011).
- [4] S. Wood, <https://www.swedishwood.com/building-with-wood/construction/wood-and-wood-based-products/structural-elements/>, .
- [5] C. Assistant, *Units in ABAQUS*, (<https://caeassistant.com/blog/units-in-abaqus-1/>).
- [6] Matthew, *Tall Timber Buildings: Applications of Solid Timber Construction in Multistory Buildings*, CTBUH (2011).
- [7] L. A. B. J. K. O. J. . R. T. Johansson, M., *Building higher with light-weight timber structures - The effect of wind induced vibrations*, Paper presented at 44th International Congress and Exposition on Noise Control Engineering (2015).
- [8] R. Abrahamsen, *Mjøstårnet - 18 storey timber building completed*, Internationales Holzbau-Forum (2018).
- [9] C. Meinhardt, *Increase of a High Rise Buildings Damping Behaviour by Applying Large Scale Tuned Mass Dampers*, IABSE Congress Report **17** (2008).

-
- [10] B. H. B.-W. M. F. G. R. T. S. D. U. W. G. e. a. Ramage, M. H., *The wood from the trees: The use of timber in construction*, (2016).
- [11] T. structures Glued laminated timber Strength classes and determination of characteristic values, *BS EN 1194:1999*, .
- [12] S. S. K. F. . R. B. Michael Ramage, Robert Foster, *Super Tall Timber: design research for the next generation of natural structure*, *The Journal of Architecture* (2017).
- [13] J. Siem. *FOUR DOWELS IN A COLUMN COMPARED TO AN ONE DOWEL CONNECTION*. (2014).
- [14] F. Solarino, L. Giresini, W.-S. Chang, and H. Huang, *Experimental Tests on a Dowel-Type Timber Connection and Validation of Numerical Models*, *Buildings* **7**, 116 (2017).
- [15] M. Dorn, K. De Borst, and J. Eberhardsteiner, *Experiments on dowel-type timber connections*, *Engineering Structures* **47**, 67–80 (2013).
- [16] H. Stamatopoulos and K. Malo, *Withdrawal stiffness of threaded rods embedded in timber elements*, *Construction and Building Materials* **116**, 263–272 (2016).
- [17] M. F. G. S. Matteo Izzi, Georg Flatscher, *Experimental investigations and design provisions of steel-to-timber joints with annular-ringed shank nails for Cross-Laminated Timber structures*, (2016).
- [18] K. D. Radek Koubek, *Friction of wood on steel*, Linnaeus University, Faculty of Technology (2014).
- [19] W.-S. C. Thomas Reynolds, Richard Harris, *Stiffness of dowel-type timber connections under pre-yield oscillating loads*, *Engineering Structures* (2014).
- [20] K. Malo, R. Abrahamsen, and M. Bjertnæs, *Some structural design issues of the 14-storey timber framed building “Treet” in Norway*, *European Journal of Wood and Wood Products* **74** (2016).

-
- [21] G. Cazzulani, T. Balduzzi, F. Ripamonti, and D. Rocchi. *Active damping for wind-tunnel aeroelastic models of large civil structures*. volume 8690, page 869003, (2013).
- [22] P. Martinez-Vazquez. *Wind-induced vibrations of structures using design spectra*. (2016).
- [23] T. Kijewski-Correa and J. Pirnia, *Dynamic behavior of tall buildings under wind: Insights from full-scale monitoring*, *The Structural Design of Tall and Special Buildings* **16**, 471 – 486 (2007).
- [24] T. Kijewski-Correa and J. Pirnia, *Chapter 3-Eigenvalue Analysis*, University of Rochester .
- [25] M.-N. Abrahamsen, Moelven Limtre AS, *MJØSTÅRNET - CONSTRUCTION OF AN 81 M TALL TIMBER BUILDING*, .
- [26] A. K. Chopra, *Dynamics of Structures*, Pearson Education (2007).
- [27] T. E. o. E. Britannica, *Damping*, Encyclopedia Britannica (2020).
- [28] R. Ambrosini, *Material Damping vs. Radiation Damping in Soil-structure Interaction Analysis,* *Computers and Geotechnics*, 33(2): 86-92, *Computers and Geotechnics - COMPUT GEOTECH* **33**, 86–92 (2006).
- [29] A. G. DAVENPORT, *THE RESPONSE OF SLENDER, LINE-LIKE STRUCTURES TO A GUSTY WIND*, *Proceedings of the Institution of Civil Engineers* (2015).
- [30] A. Feldmann, H. Huang, W.-S. Chang, R. Harris, P. Dietsch, M. Gräfe, and C. Hein. *Dynamic properties of tall Timber Structures under wind-induced Vibration*. (2016).
- [31] A. R. Nathalie Labonnote. *Experimental evaluations of material damping in timber beams of structural dimensions*. (2013).
- [32] J. WECKENDORF, B. Zhang, A. KERMANI, D. REID, and P. ANDERSEN, *Damp-*

- ing Characteristics of Timber Flooring Systems with Respect to Low-Frequency Vibration Modes*, 10th World Conference on Timber Engineering 2008 **4** (2008).
- [33] Fragiacomio and Lukaszewska, *Development of prefabricated timber–concrete composite floor systems*, Structures and Buildings **164** (2011).
- [34] J. Wacker and J. Groenier, *Comparative Analysis of Design Codes for Timber Bridges in Canada, the United States, and Europe*, Transportation Research Record: Journal of the Transportation Research Board **2200**, 163–168 (2010).
- [35] A. Ghorbani and A. Noveiri. *DYNAMIC ANALYSIS OF PILED RAFT SYSTEM ON SAND USING THREE DIMENTIONAL FINITE ELEMENT METHOD*. (2015).
- [36] I. Løken and A. Kaynia, *Effect of foundation type and modelling on dynamic response and fatigue of offshore wind turbines*, Wind Energy **22** (2019).
- [37] R. P. S. Ashok Gupta, *Fatigue Behaviour of Offshore Structures*, **22** (1986).
- [38] D. Ptilakis and D. Clouteau. *The Role of the Soil Stiffness on the Dynamic Impedance Functions*. (2007).
- [39] E. Kausel. *Early history of soil–structure interaction*. page Soil Dynamics and Earthquake Engineering, (2010).
- [40] S. Grange, P. Kotronis, and J. Mazars, *A macro-element to simulate dynamic Soil-Structure Interaction*, Engineering Structures , 3034–3046 (2009).
- [41] E. C. Á. Cunha, *Dynamic soil-pile-interaction effects on eigenfrequency and damping of slender structures*, (2014).
- [42] M. N. T. Nogami, *Resistance of soil to a horizontally vibrating pile*, (1977).
- [43] <http://www.tesolution.com/windtunnelbuildings.html>, *WIND TUNNEL TEST FOR BUILDINGS BY TESOLUTION*, .

- [44] <https://www.standard.no/no/Nettbutikk/produktkatalogen/Produktpresentasjon/?ProductID=398860>, *NS-EN 1991-1-4:2005+NA:2009*, .
- [45] P. Kraemer and H. Friedmann. *Experimental validation of stochastic subspace algorithms for structural health monitoring of offshore wind turbine towers and foundations*. (2016).
- [46] T. M. KE. Simiu. *Design of Buildings and Bridges for Wind: A Practical Guide for ASCE-7 Standard Users and Designers of Special Structures*. (2006).
- [47] E. S. DongHun Yeo. *Database-Assisted Design for Wind Effects on High-Rise Structures and Its Potential for Assessment of CFD Simulation*. (2010).
- [48] J. A. Main and W. P. Fritz. *Database-Assisted Design for Wind: Concepts, Software, and Examples for Rigid and Flexible Buildings*. (2006).
- [49] C. A. Kazemi Amiri. *A procedure for in situ wind load reconstruction from structural response only based on field testing data*. (2017).
- [50] R. Kiviluoma, *Aeroelastic wind-tunnel testing technique revisited*, CTBUH 2005 - 7th World Congress Renewing the Urban Landscape, Proceedings (2005).
- [51] Y. Kim and S. Yoon, *Aeroelastic Vibration of Super-Tall Buildings*, Advanced Materials Research **1025-1026**, 914–917 (2014).
- [52] D. Wilcox, *Turbulence Modeling for CFD (Third Edition) (Hardcover)* (2006).
- [53] P. Sullivan, J. McWilliams, and C.-H. Moeng, *A subgrid-scale model for Large-Eddy simulation of planetary boundary-layer flows*, Boundary-Layer Meteorology **71**, 247–276 (1994).
- [54] A. Class, *What is the difference between k - ω , k - ϵ and Spalart-allmaras turbulent models?*, (2014).

- [55] N. Labonnote. *Damping in Timber Structures*. PhD thesis, (2012).
- [56] K. Malo, R. Abrahamsen, and M. Bjertnæs, *Some structural design issues of the 14-storey timber framed building “Treet” in Norway*, *European Journal of Wood and Wood Products* **74** (2016).
- [57] J. Sliseris, L. Gaile, and L. Pakrastins, *Numerical analysis of behaviour of cross laminated timber (CLT) in blast loading*, *IOP Conference Series: Materials Science and Engineering* **251**, 012105 (2017).
- [58] C. Fredö, *Material and Structural Damping in Abaqus?*, (2017).
- [59] G. W. Emma, *Improving Acoustic Insulation Using Vibration-Damping Infills in Floors*, (2012).
- [60] R. A. Serway, *Physics for Scientists and Engineers 2nd*, (1986).
- [61] N. Thng, *Physics for Scientists and Engineers 2nd*, .
- [62] J. L. . N. Landbrukshogskole, *Soil Map Norway - Jordbunnskart*, (1983).
- [63] B. Fellenius and A. Eslami, *Soil profile interpreted from CPTu data*, *Geotechnical Engineering Conference* **1** (2000).
- [64] A. Kaynia and E. Kausel, *Dynamic Stiffness and Seismic Response of Pile Groups*, *NASA STI/Recon Technical Report N* , 16586– (1982).
- [65] Q. Shen, G. Wang, and M. Gu, *Numerical simulation of wind loads on high-rise buildings and disaster analysis*, **36**, 592–597 (2008).
- [66] <http://www.cd-adapco.com/products/star-ccm/documentation>, *STAR CCM+ Users Manual*, , 592–597 (2021).
- [67] <https://www.computationalfluidynamics.com.au/tips-tricks-turbulence-part-4-reviewing-how-well-you-have-resolved-the-boundary->

- TURBULENCE PART 4 - REVIEWING HOW WELL YOU HAVE RESOLVED THE BOUNDARY LAYER*, LEAP CFD Team (2013).
- [68] https://web.cecs.pdx.edu/~gerry/class/ME448/StarCCM/pdf/volumetric_mesh_control.pdf, *Volumetric Controls (pdx.edu)*, LEAP CFD Team (2012).
- [69] D. C. Wilcox, *Reassessment of the scale-determining equation for advanced turbulence models*, (1988).
- [70] D. Wilcox, *Formulation of the k - Turbulence Model Revisited*, Aiaa Journal - AIAA J **46**, 2823–2838 (2008).
- [71] P. Richards and S. Norris, *Appropriate boundary conditions for computational wind engineering models revisited*, Journal of Wind Engineering and Industrial Aerodynamics - J WIND ENG IND AERODYN **99**, 257–266 (2011).
- [72] M. Cindori, F. Juretic, H. Kozmar, and I. Džijan, *Steady RANS model of the homogeneous atmospheric boundary layer*, Journal of Wind Engineering and Industrial Aerodynamics **173**, 289–301 (2018).
- [73] M. Shirzadi, Y. Tominaga, and P. Mirzaei, *Experimental and Steady-RANS CFD Modelling of Cross-ventilation in Moderately-dense Urban Areas*, Sustainable Cities and Society **52**, 101849 (2019).
- [74] S. M. Salim, K. Ong, and S. Cheah. *Comparison of RANS, URANS and LES in the Prediction of Airflow and Pollutant Dispersion*. (2011).
- [75] J. F. M. G. M. L. Rogers. *Wind Energy Explained: Theory, Design and Application, Second Edition*. (2010).
- [76] C. F. C. F. Michael V. Cook BSc, MSc, *Chapter 14 - Flight in a Non-steady Atmosphere*, A Linear Systems Approach to Aircraft Stability and Control (2013).
- [77] T. Pritz. *Frequency power law of material damping*. (2004).

- [78] A. Luis and A. Awruch, *Aerodynamic and aeroelastic analyses on the CAARC standard tall building model using numerical simulation*, *Computers and Structures* **87**, 564–581 (2009).
- [79] FengFu, *Chapter Two - Fundamentals of Tall Building Design*, *Design and Analysis of Tall and Complex Structures* (2018).
- [80] A. Hemidi, F. Henry, S. Leclaire, J.-M. Seynhaeve, and Y. Bartosiewicz, *CFD Analysis of a Supersonic Air Ejector. Part I: Experimental Validation of Single-Phase and Two-Phase Operation*, *Applied Thermal Engineering* **29**, 1523–1531 (2009).
- [81] NASA, *Mach Number, Role in Compressible Flows*, <https://www.grc.nasa.gov/WWW/k-12/airplane/machrole.html> .
- [82] N. Basse, *Python code to calculate turbulence intensity based on Reynolds number and surface roughness.*, (2019).
- [83] J. Wieringa, *Updating the Davenport roughness classification*, *Journal of Wind Engineering and Industrial Aerodynamics* (2019).
- [84] S. Kaneko, T. Nakamura, F. Inada, M. Kato, K. Ishihara, T. Nishihara, N. Mureithi, and M. Langthje, *Flow-Induced Vibrations: Classifications and Lessons from Practical Experiences: Second Edition*, *Flow-Induced Vibrations: Classifications and Lessons from Practical Experiences: Second Edition* , 1–410 (2013).
- [85] Y. Kim, Y.-L. Lo, and C. Chang, *Characteristics of unsteady pressures on slender tall building*, *Journal of Wind Engineering and Industrial Aerodynamics* **174**, 344–357 (2018).
- [86] X. Karatzia and G. Mylonakis. *HORIZONTAL RESPONSE OF PILES IN INHOMOGENEOUS SOIL: SIMPLE ANALYSIS*. (2012).